University of Liverpool

Bayesian Modal Identification using Asynchronous Ambient Data

Thesis submitted in accordance with the requirements of the University of Liverpool for the degree of Doctor in Philosophy

By

Yi-Chen Zhu

June 2018

Abstract

Operational modal analysis (OMA) has been used nowadays for identifying the modal properties of structures (e.g., natural frequencies, damping ratios and mode shapes) based on the measured ambient vibration data for its high economy and efficiency. In vibration tests, multiple sensors are often used to obtain the mode shape information of the instrumented structure. Time synchronisation among the sensors/data channels is normally required by conventional modal identification techniques. In full-scale tests, this often requires additional equipment and logistics in order to obtain synchronous data. Ambient vibration tests can be conducted more flexibly and efficiently if time synchronisation is not required in OMA. Motivated by the above concerns, this thesis aims at developing Bayesian OMA approaches based on asynchronous ambient data.

This thesis first investigates the characteristics of asynchronous data in OMA. Inspired by the experimental findings, a stationary stochastic model is proposed to model asynchronous data in OMA with imperfect coherence to capture the key asynchronous characteristics within suitable time scales. The theoretical properties of the power spectral density (PSD) matrix for asynchronous ambient data are also derived. Based on this model, two Bayesian OMA methods using fast Fourier transform (FFT) of asynchronous ambient data are proposed. Balancing simplicity and utility, the first method assumes zero coherence among the synchronous data groups, which leads to an efficient algorithm for determining the most probable values as well as the posterior uncertainties of modal properties. The second method assumes general coherence values among the synchronous data groups, which strictly obeys the proposed asynchronous data model. It provides a more robust means to

identify the modal parameters based on asynchronous data without zero coherence approximation, although more computational efforts are needed. Synthetic, laboratory and field test data are used to verify and illustrate the asynchronous data model and these two Bayesian OMA methods. A full-scale ambient test with multiple setups is also presented, where the challenges and complications related to ambient vibration test with asynchronous data in real applications are investigated.

This work is expected to gain more insights on time synchronisation problems in OMA and provide a pathway for more flexible and economical implementation of ambient vibration tests.

Acknowledgements

I would like to express my best appreciation to my supervisor Prof. Siu-Kui Au for his enthusiastic guidance, tremendous mentoring and constant encouragement. It is he who guides me to the scientific world and helps me appreciate the beauty of science. His profound knowledge and open-minded perspectives continuously inspire me throughout my doctoral study. Besides his rigorous attitude to science, I have also benefited a great deal from his positive life philosophy. It is a great honour and pleasure for me to be one of his students and conduct research under his supervision.

I would also like to thank Dr. Steve Jones, who gave valuable suggestions not only on my study but also on my life during my undergraduate and Ph.D. study in the University of Liverpool. Special thanks are due to Prof. James Brownjohn at the University of Exeter where I learned a lot from him about field vibration testing through a one-week field test for the Jiangyin Yangtze River Bridge in China. My sincere thanks also go to Prof. Mitsuyoshi Akiyama in Waseda University.

I am grateful to the University of Liverpool and Tung Foundation Scholarship Fund for the generous financial support during my Ph.D. study. The UK Engineering & Physical Sciences Research Council Grant (EP/N017897/1) is also gratefully acknowledged. My deep appreciation goes to all the faculties and staffs of School of Engineering and Institute for Risk and Uncertainty in the University of Liverpool. Special thanks also go to my buddies in the research group: Dr. Binbin Li, Mr. Yanlong Xie, Miss Xinrui Wang and Mr. Zuo Zhu for the enjoyable discussion about the research and the enthusiastic help in performing the laboratory and field tests. The wonderful times we shared and the warm friendship also brought me a lot of happiness during my life in Liverpool.

Finally, I would like to express my deepest gratitude to my family. My greatest appreciation goes to my wife, Minghuan Qu, for her unwavering support and all the sacrifices she made on my behalf. Thank her for every dish she cooked for me and every journey she accompanied. Her unconditional love is what kept me going during my Ph.D. study and sustains me so far. I would also like to thank my parents and parents in law for their love and support of my education and life.

Table of Content

List of Figures

List of Tables

List of Abbreviations

ARMA	auto-regression moving model
c.o.v.	coefficient of variation
DAQ	data acquisition
DOF	degree of freedom
FFT	fast Fourier transformation
GPS	global position system
i.i.d.	independent and identically distributed
LSCF	least square complex frequency method
MAC	modal assurance criterion
MPV	most probable value
NExT	natural excitation techniques
NLLF	negative log-likelihood function
NTP	network time protocol
OMA	operational modal analysis
PDF	probability density function
ppm	parts per million
PSD	power spectral density
RBS	reference broadcast synchronisation
SHM	structural health monitoring
SNR	signal-to-noise ratio
SSI	stochastic subspace identification
SV	singular value
TPSN	time-syn protocol for sensor network

Chapter 1: Introduction

1.1 Motivation

Civil infrastructures are facilities and systems that support human activities including housing, transportation and communication. They are the lifeline of economic and social development. Throughout their service life, civil infrastructures constantly suffer from natural and man-made hazards as well as their own natural aging, which may lead to structural damage and collapse with casualties and financial losses. Maintenance management is hence essential to civil infrastructures in order to ensure their safety and service quality. As indicated in UK infrastructure cost review [1], the infrastructure renewal and maintenance cost is in the order of 15 billion pounds per annum. In addition to cost-effective maintenance technologies, developing prognostic and diagnostic methodologies is of great importance in optimising the balance of structure performance and maintenance cost. Structural health monitoring (SHM) [2,3] aims at assessing the performance and health condition of structures based on measured structural response data with applications in structural damage detection, localisation and quantification. The development of structural health monitoring techniques can also facilitate better decision making for designers and owners of civil infrastructures on planning the maintenance and replacement actions of existing structures.

Modal identification aims at identifying the modal properties of structures involving natural frequencies, damping ratios and mode shapes based on the measured structural response data [4,5]. It is often the first step in SHM that provides the 'in-situ' information about the current status of the structure. Ambient modal identification, also known as operational modal analysis (OMA) [6,7], identifies the

modal properties of structures under ambient excitation condition. It does not require artificial loading conditions but assumes the excitation to be statistically random. Due to its high economy and efficiency, OMA has attracted great attention in both theory development and field test applications over the past decades.

When conducting modal identification tests, time synchronisation is usually required by conventional methods. That is, digital data in different channels should be recorded simultaneously at the same time scale. Synchronisation is not only to do with the start time for different data channels, but also with the sampling pace at which they are recorded. When multiple data acquisition (DAQ) units [8] are used in the test, time asynchronisation cannot be taken for granted. Each DAQ unit has its own clock for data sampling and the actual sampling rates among the DAQ units are not identical if they are running independently. Time synchronisation schemes need to be well considered in modal identification tests in order to get synchronous data, which inevitably leads to extra cost in field deployment or additional equipments. There can be significant advantages in the flexibility and efficiency of field data collection if OMA can be performed based on asynchronous data. Motivated by the above concerns, the primary objective of the research in this thesis is to develop OMA approaches that can identify modal properties of structures based on asynchronous ambient data.

1.2 Literature review

This section introduces modal identification tests of civil structures and the time synchronisation issues associated with the tests. Literature review mainly focuses on OMA (ambient vibration tests), which has been used in the recent decades because of its high economy and flexibility. Due to the unknown nature of excitation

information, the identification uncertainty in ambient vibration tests is significant compared to other modal identification tests. Bayesian approach is introduced, which provides a fundamental way to quantify uncertainty based on measured data and investigate its asymptotic behaviour with respect to test configurations. The details of the Bayesian OMA theory are reviewed, which helps develop the modal identification methods for asynchronous ambient data in this work. When conducting modal identification tests with multiple data channels, time synchronisation must be considered among the data channels. An overview of synchronisation techniques used in OMA is given in this section. The drawbacks of conventional time synchronisation methods are discussed, which yield the major motivation of developing modal identification methods based on asynchronous ambient data in this work.

1.2.1 Modal identification

Thanks to the sophisticated construction techniques and advanced materials, modern structures such as skyscrapers and long-span bridges can be built lighter and more slender. However, these structures are more sensitive to dynamic loads. The 'modal properties' of a structure mainly include natural frequencies, damping ratios and mode shapes. These are critical properties characterising the response of structures against dynamic loads (e.g., wind, earthquake, traffic) [9]. Natural frequencies govern the resonance bands of the structure. The dynamic response will be significantly amplified if the frequency of excitation lies in these bands. A well-known example is the Millennium bridge in London [10], whose first lateral natural frequency lies in the frequency range of human walking, leading to excessive lateral vibration. Damping ratio influences the vibration level and energy dissipation of the structure. For super tall buildings and long-span bridges, damping plays a significant

role in their serviceability performance [11–13]. The design and maintenance of vibration control devices (e.g., damper) also depend on the precise estimation of damping ratios [14,15]. Mode shapes reflect the response patterns of the instrumented structure associated with the stiffness and mass distribution. The variation in mode shape can also be used for tracking structure condition with applications in detecting structural damage [16,17].

The process of identifying the modal properties of a structure based on measured structure response data is known as modal identification. It provides the baseline information about the 'in-situ' status of a structure [4,5], which can be quite different from the predictions in the design stage. The natural frequencies of the structure can vary with the amplitude of excitation, the temperature and aging, etc. [18–20]. Current design models for damping are all empirical based on historic databases [21,22] with significant scatter. Investigating the in-situ damping properties can also lead to better prediction of dynamic behaviour in structural design. Modal identification has become an indispensable task in SHM [2,3,23], which provides crucial information for downstream applications, e.g., model updating [24,25], vibration control [13] and damage detection [26,27].

Vibration tests

The vibration tests for modal identification can be mainly categorised into three types, i.e., free, forced and ambient vibration tests. In a free vibration test [28–30], the structure is left to vibrate after some initial excitations and the measured response data under the free vibration phase are selected for analysis. Various forms of modal identification techniques have been developed based on measured free vibration data. The least square methods have been proposed where the modal parameters are

identified as the one that minimises the difference between the theoretical and measured vibration response in a least square sense [28]. The Ibrahim time domain method makes use of the generalized eigenvalue decomposition [31] and the complex exponential method is developed based on the singular value decomposition [32]. Methods based on wavelet transformation also exist, including discrete wavelet transform [33] and continuous wavelet transform [30]. In a Bayesian context, a modal identification method based on free vibration data has been proposed recently [34,35], which is capable of determining the most probable value of modal parameters as well as quantifying the associated uncertainties.

In a forced vibration test [36–38], the structure is subjected to some artificial excitations. In this context, both the input loading and the structure response time histories are used for modal identification. The half-power bandwidth method [39,40] is the simplest modal identification method based on forced vibration data but lacking identification accuracy. Methods based on curve fitting of frequency response functions provide a sophisticated means for modal parameters estimation [41]. Other methods also exist, including the circle fitting method [42], the Edwin-Gleeson method [43], the orthogonal polynomial method [44], etc. A Bayesian modal identification method for forced vibration data has also been developed [45], with the enhanced one considering the ambient vibration effect [46].

For free and forced vibration tests, the artificial excitation should be large enough such that the measured data are dominated by the required dynamic response. For civil infrastructures which are typically large-scale, this often leads to overheads in excitation equipment (e.g., shaker) and site control (e.g., the structure under shutdown condition). These two types of test may also cause damage to the structure

if the excitation is not properly controlled. On the other hand, ambient vibration tests can be conducted under environmental excitations such as wind, cultural activities and microtremor without artificial loading conditions. The excitation information is unknown but assumed to be statistically random. Due to its high economy and feasibility, ambient vibration tests have been widely applied for modal identification in recent years [47–49]. One major drawback of this test is that the input loading is unknown and cannot be directly controlled. The modal structural response may not be significant compared to free and forced vibration test and the associated identification uncertainties need to be well considered.

Operational modal analysis

Ambient modal identification, also known as operational modal analysis (OMA), is the modal identification strategy based on ambient vibration data. Methods have been developed in both non-Bayesian and Bayesian manner. In OMA, non-Bayesian methods are conventional. Peak picking [50] method may be the simplest non-Bayesian method. The natural frequency of the mode is simply picked based on the spectral peak of the sample PSD matrix [51] and the mode shape is determined as the corresponding eigenvector at natural frequency. The damping ratio can be estimated based on the half bandwidth method. Despite its simplicity and intuitiveness, the peak picking method can only provide a rough estimation of modal parameters for well-separated modes with small damping. The estimated mode shape is actually the operational deflection shapes at the resonance frequency instead of the true mode shape of the mode of interest. Frequency domain decomposition [52] can be considered as an extension of peak picking method which resolves the multiple modes problem by extracting modal properties based on the singular value

decomposition of the sample PSD matrix. However, it should be noted that the mode shape estimation based on this method could be biased for the closely spaced modes. This is because the mode shapes are determined based on the singular vectors which are orthogonal but this may not be the case for the identified mode shapes (which are confined only to the measured degrees of freedom) of two closely-spaced modes. Some variants of this method can also be found, see [53,54]. The peak picking and frequency domain decomposition are nonparametric methods. The Least Square Complex Frequency (LSCF) method [55] is a parametric method in the frequency domain. The modal parameters are identified by fitting the fraction polynomial model in a least square sense. The original LSCF method mainly focuses on well separated mode cases, where the poly-reference version of this method (also known as PolyMAX) has been proposed for closely spaced modes [56].

The foregoing are the frequency domain methods. Non-Bayesian OMA methods have also been proposed in the time domain. The auto-regression moving model (ARMA) has been attempted for modal identification in the past [57]. However, this type of method has not been widely used in practical applications of OMA for civil structures as they are time consuming with convergence problems. The natural excitation techniques (NExT) for modal identification [58] is a popular time domain method in the early stage of OMA. It is based on the correlation functions by expressing the random response as a sum of decaying sinusoids. Stochastic subspace identification (SSI) technique estimates modal parameters by adopting a linear state-space model. The modal parameters are determined by linear regression of the system matrices. Two main strategies have been developed: the Covariance-driven (SSI-COV) method [59,60] and the Data-driven (SSI-DATA) method [61]. The SSI-COV method deals with the stochastic realisation problem based on the covariance

of system outputs while the SSI-DATA method operates directly on the time series data by applying numerical techniques like QR factorisation and least square method. Several variants of SSI method also exists, see details in [62]. The SSI methods provide a quick and efficient estimation of modal parameters, which leads to wide applications in OMA [49,63,64]. Other non-Bayesian OMA techniques also exist, including blind source identification [65–67] and maximum likelihood identification [68,69], etc. Recently, transmissibility based OMA techniques have been proposed [70,71] with the premise of being robust to the characteristics of the excitation spectra in identifying mode shapes.

OMA approaches have also been developed from a Bayesian perspective. In this context, modal identification is treated as a probability inference problem. The information about modal parameters is encapsulated in the 'posterior' distribution, which is a joint probability density function (PDF) given modelling assumptions and available information of data. The most probable value (MPV) of modal parameters then can be determined by optimising the posterior PDF. Bayesian approaches provide a fundamental way to identify the modal parameter as the physical assumptions are obeyed and information in the measured data is fully used for inference. The drawback is that the optimisation procedure is nonlinear and the dimension of matrix computation involved grows with the measured degrees of freedom (DOF) and the data length, which requires more computational effort. Reducing the dimension of the optimisation problem becomes a natural target for Bayesian approaches. Bayesian OMA methods have been proposed in different contexts, e.g., in the time domain [72], frequency domain based on sample power spectral density (PSD) matrix [73–75] and fast Fourier transform (FFT) of data [76,77]. Time domain formulation is too restricted in the modelling assumptions and

sample PSD matrix formulation requires averaging techniques which is less fundamental. Compared with these two formulations, the Bayesian FFT method is more robust in model assumptions while still mathematically tractable. Efficient algorithms have been developed based on different settings, e.g., well-separated modes [78], closely-spaced modes [79,80] and multiple setups [81]. The modal identification methods for asynchronous ambient data proposed in this work are developed based on the Bayesian FFT method. Detailed theory of this method is reviewed in Section 1.2.2.

Identification uncertainty

The loading information in OMA is unknown and its intensity and frequency characteristics cannot be directly controlled. The structural response may not be significant and hence the effect of measurement noise cannot be neglected. The identification uncertainty is normally much larger than those in known input vibration tests (e.g., forced vibration or free vibration tests). Quantifying and managing the uncertainty of identified modal parameters then becomes essential for OMA. It often involves two aspects. Given the measured ambient vibration data, it is of interest to know the associated uncertainty of the identified modal parameters, which is referred as 'uncertainty quantification'. On the other hand, it is desirable to know the achievable identification quality/uncertainty for a given test configuration when planning the vibration tests.

For non-Bayesian or 'frequentist' methods, identification uncertainty is often quantified in terms of the ensemble variance of estimates over repeated experiments. Some challenges are discussed in [82]. For SSI, computational methods have been developed based on first-order perturbation for single setup data [83,84] and multi-

setup data [85]. See also [86] for the variance of maximum likelihood modal parameter estimator in the state-space time domain. Probabilistic models for raw scalar transmissibility functions have also been proposed recently [87,88], which helps quantify the identification uncertainty for transmissibility based OMA methods.

Bayesian approaches [89] provide a fundamental basis for investigating the identification uncertainty in a probabilistic manner. Identification uncertainty of modal parameters can be quantified in terms of the covariance matrix associated with the 'posterior' (i.e. given data) distribution of modal parameters. With sufficient data (which is typically the case in OMA), the posterior distribution of modal parameters has a single peak and can be approximated by a Gaussian distribution. The 'posterior covariance matrix' then can be obtained as the inverse of Hessian of the negative log-likelihood function (NLLF) [25]. For OMA with synchronous data, efficient methods have been developed in different settings, e.g., well-separated modes [78], close modes [80] and multiple setups [90]. Mathematical connection between Bayesian and frequentist quantification of identification uncertainty has also been discussed [91].

Uncertainty quantification only gives a 'point-wise' view of the uncertainty behaviour in OMA for a given set of data. For test planning, it is of interest to know the relationship between test configuration and identification uncertainties. For example, how long should the measured data be; how many sensors should be used and how good these sensors are in order to achieve a certainty level of identification accuracy. This is referred as 'uncertainty law'. Focusing on well-separated mode, the closed form analytical expressions giving the leading (zeroth) order term of the posterior variance of modal properties have been derived under asymptotic

conditions of long data and small damping [92,93]. It gives the achievable identification precision of OMA. Recently, the first order uncertainty law has also been derived [94], revealing the effect of modal signal-to-noise ratio (SNR, the ratio of the spectral density of modal excitation to the spectral density of prediction error at the resonance peak of the mode) on the identification uncertainty of modal parameters. The first order uncertainty law provides a scientific guidance on planning ambient vibration tests as the signal-to-noise ratio depends on the test configurations such as sensor noise, sensor number and measurement locations.

1.2.2 Bayesian OMA framework

The OMA methods for asynchronous data proposed in this work are developed based on Bayesian approach using the FFT of ambient data. The overall Bayesian framework is reviewed in this section. Bayesian approach views modal identification as a probability inference problem based on available information. The information about modal parameters is encapsulated in the posterior PDF given measured data and modelling assumptions. For modal identification problem that is 'globally identifiable' [24], maximising the posterior PDF gives the MPV of modal parameters and the identification uncertainties are characterised through the posterior covariance matrix.

Most of the non-Bayesian modal identification methods can provide a quick estimation of modal parameters. This may not be the case for Bayesian methods, however. Bayesian approaches require numerical optimisation and iteration to determine the MPV of modal parameters. There is a nonlinear relationship between the likelihood function and modal parameters. The dimension of matrix computation involved in optimising the likelihood function grows with the measured DOFs.

Efficient iterative algorithms that can suppress the computational effort shall be proposed when developing Bayesian modal identification methods. The original Bayesian framework for OMA was proposed in [72], which is a time domain method applicable for synchronous data in a single setup. A frequency domain method based on sample PSD has also been developed [73]. The time domain method is restricted to the modelling assumptions on excitation and measurement noise and the sample PSD method relies on averaging techniques. To address these problems, Bayesian approach based on FFT of ambient data has been developed. It provides a rigorous means that makes full use of measured data without artificial averaging and the modelling assumptions are strictly obeyed. The original formulation was proposed in [76]. Fast algorithms have also been proposed that allows practical implementation in different contexts, e.g., well-separated modes, multiple modes and multiple setups. See reviews in [77]. The details of this method are as follows.

Let $\left\{\hat{\ddot{\mathbf{x}}}_j \in R^n\right\}_{j=1}^N$ denote the measured ambient acceleration data with n DOFs of the subject structure and N sampling points per channel. The (scaled) FFT of $\left\{\hat{\ddot{\mathbf{x}}}_j\right\}$ is defined as:

$$\mathcal{F}_k = \sqrt{\frac{2\Delta t}{N}} \sum_{j=1}^{N} \hat{\ddot{\mathbf{x}}}_j \exp\left[-2\pi \mathbf{i} \frac{(k-1)(j-1)}{N}\right] \tag{1}$$

where $\mathbf{i}^2 = -1$ and Δt is the sampling interval. The FFT corresponds to frequency $\mathrm{f}_k = (k-1)/N\Delta t\,(\mathrm{Hz})$ for $k = 1,\ldots N_q$, where $N_q = \mathrm{int}(N/2)+1$ (int(.) denotes integer part) is the index corresponding to the Nyquist frequency. The PSD matrix of the measured data at frequency f_k can be calculated as multiplying $\mathcal{F}_k$ by its conjugate transpose. The scaling factor $\sqrt{2\Delta t/N}$ is defined such that the PSD is one-sided with respect to frequency in Hz. For modal identification, only the FFT

data within a selected frequency band dominated by the modes of interested is used. Let $\{\mathcal{F}_k\}$ denote such collection with N_f points in the set.

In the context of Bayesian inference, the measured data depends on the set of modal parameters $\boldsymbol{\theta}$ to be identified, which normally includes natural frequencies, damping ratios, mode shapes, etc. According to the Bayes' theorem, the posterior PDF of $\boldsymbol{\theta}$ given the FFT data $\{\mathcal{F}_k\}$ can be expressed as

$$p\left(\boldsymbol{\theta}\middle|\{\mathcal{F}_k\}\right) = p\left(\{\mathcal{F}_k\}\middle|\boldsymbol{\theta}\right)\frac{p(\boldsymbol{\theta})}{p\left(\{\mathcal{F}_k\}\right)} \tag{2}$$

where $p\left(\{\mathcal{F}_k\}\middle|\boldsymbol{\theta}\right)$ is the likelihood function; $p(\boldsymbol{\theta})$ is the prior PDF that reflects one's knowledge about $\boldsymbol{\theta}$ in the absence of data and $p\left(\{\mathcal{F}_k\}\right)$ is the normalizing constant that does not depend on $\boldsymbol{\theta}$. The prior PDF is assumed to be uniformly distributed as the typical data size in modal identification is sufficiently large that the likelihood function is fast-varying compared to the prior PDF. The posterior PDF is then proportional to the likelihood function:

$$p\left(\boldsymbol{\theta}\middle|\{\mathcal{F}_k\}\right) \propto p\left(\{\mathcal{F}_k\}\middle|\boldsymbol{\theta}\right) \tag{3}$$

Assuming long data duration and high sampling rate, $\{\mathcal{F}_k\}$ are asymptotically independent at different frequencies and jointly (circularly symmetric) complex Gaussian [95]. The likelihood function is then given by:

$$p\left(\{\mathcal{F}_k\}\middle|\boldsymbol{\theta}\right) = (\pi)^{-nN_f} \times \prod_k \left(\det \mathbf{E}_k\right)^{-1} \exp\left[-\sum_k \mathcal{F}_k^* \mathbf{E}_k^{-1} \mathcal{F}_k\right] \tag{4}$$

where '*' denotes conjugate transpose and $\mathbf{E}_k = \mathrm{E}[\mathcal{F}_k \mathcal{F}_k^* | \boldsymbol{\theta}]$ is the theoretical PSD matrix of data with respect to $\boldsymbol{\theta}$. Here E[.] denotes expectation. For analysis or

computation, it is more convenient to work with the 'negative log-likelihood function' (NLLF) such that:

$$p\left(\boldsymbol{\theta}\middle|\{\mathcal{F}_k\}\right) \propto \exp\left[-L(\boldsymbol{\theta})\right] \tag{5}$$

where

$$L(\boldsymbol{\theta}) = \sum_k \ln \det \mathbf{E}_k + \sum_k \mathcal{F}_k^* \mathbf{E}_k^{-1} \mathcal{F}_k \tag{6}$$

For sufficient data, modal identification problem is 'globally identifiable' [24]. The MPV of $\boldsymbol{\theta}$ can be determined by maximising the posterior PDF, or equivalently minimising the NLLF with respect to $\boldsymbol{\theta}$. The posterior PDF can be approximated by a Gaussian PDF

$$p\left(\boldsymbol{\theta}\middle|\{\mathcal{F}_k\}\right) = (2\pi)^{-n_{\boldsymbol{\theta}}/2} \left(\det \hat{\mathbf{C}}\right)^{-1/2} \exp\left[-\frac{1}{2}\left(\boldsymbol{\theta}-\hat{\boldsymbol{\theta}}\right)^T \hat{\mathbf{C}}^{-1}\left(\boldsymbol{\theta}-\hat{\boldsymbol{\theta}}\right)\right] \tag{7}$$

where $n_{\boldsymbol{\theta}}$ is the number of parameters in $\boldsymbol{\theta}$; $\hat{\boldsymbol{\theta}}$ is the MPV and $\hat{\mathbf{C}}$ is the posterior covariance matrix, equal to the inverse of Hessian of NLLF at MPV. The identification uncertainties of modal parameters are fully characterised by the posterior covariance matrix.

The complex Gaussian PDF is the core of the Bayesian OMA framework. It holds for all stochastic stationary ambient data regardless of the spectral characteristics of the activities. The latter is reflected in the theoretical PSD matrix $\mathbf{E}_k$, which should be derived based on the modelling assumptions of measured data. The efficient computation of determinant and inverse of $\mathbf{E}_k$ (hence the NLLF) and the posterior covariance matrix is the natural target of developing Bayesian modal identification algorithms.

1.2.3 Time synchronisation

When multiple channels of data are measured, time synchronisation is often required among the channels by conventional modal identification methods. Compared to asynchronous data, synchronous data are much easier to be modelled mathematically. Synchronisation does not only mean that different channels start recording at the same time, but also sample the data simultaneously at the same time scale afterwards. When multiple DAQ units are used, time synchronisation should not be taken for granted even they are connected to the same computer for data recording. Crystal oscillators (e.g. Quartz) are commonly used in DAQ units to control the sampling process [96]. Although they can provide time basis with high precision and stability, the actual sampling interval of each oscillator may still vary due to temperature, aging and so forth [97]. As long as the sampling clocks in different DAQ units run independently without particular synchronisation schemes, the actual sampling interval among the units will not be identical and the measured data will have synchronisation problems.

In practical contexts, synchronisation means that the sampling time difference between data channels is within a certain tolerance. The basic setting is to connect different sensors to a central DAQ unit through cables where the analog data can be sampled synchronously. In full-scale tests, the required cables can be very long, which inevitably leads to additional noise in the measured data and extra cost of logistics. To avoid using long analogue cables, common configurations use multiple DAQ units to record the data locally and synchronise the DAQ units digitally using some synchronisation provisions. For outdoor applications, DAQ units can be synchronised with a common GPS (Global Positioning System) clock [98] through GPS receivers. For indoor applications where GPS signal is weak, one alternative

option is to use high-precision clocks as a substitution. These clocks can be first trained with a common time base (e.g. GPS). Once the clocks are synchronised, they can be disconnected with the reference clock and provide a high precision time stamp independently for the DAQ units within a reasonable time span. When Ethernet ports are provided, some DAQ units are also capable to be synchronised using the Network Time Protocol (NTP) [99]. In this context, the analogue cables are relatively short but the Ethernet cables can still be long.

Recently, wireless sensor networks have been applied in modal identification tests [100]. Time synchronisation schemes have been developed for wireless sensors. Reference Broadcast Synchronisation (RBS) [101] and Timing-Sync Protocol for Sensor Networks (TPSN) [102] are two basic synchronisation methods for wireless sensors networks, which can provide time precisions in the order of microseconds. Time synchronisation algorithms specifically for wireless SHM sensors have also been developed [103].

Asynchronisation issue caused by time shift among the sensors is a major concern in OMA tests when using wireless sensor networks. It often leads to errors in both the amplitude and phase of the identified mode shapes. This issue has been investigated in both laboratory and field test studies [104–107]. Some off-line synchronisation methods have been proposed trying to eliminate the effect of synchronisation-induced errors in OMA after the structural response data are measured. A synchronisation method has been proposed to estimate the time shift based on the cross correlation between different measured data channels for well-separated mode case [108]. Dragos and Smarsly proposed an off-line synchronisation technique

based on the differences among the phase angles of the frequency components corresponding to the first mode [109].

It is not easy to get synchronous data in real implementation. It often requires additional instruments and the setups need to be well planned to avoid extra logistics. Field test can be conducted in a more economical and efficient manner if OMA can be performed directly based on asynchronous data. This is the major motivation of this thesis.

1.3 Objectives and outline

The main objective of the research is to develop OMA methods that are capable of identifying the modal properties of structures based on asynchronous ambient data. An asynchronous data model with imperfect coherence is first proposed in order to quantitatively describe asynchronous data in OMA. Based on this model, a fast Bayesian modal identification method is developed. Zero coherence among the synchronous data groups is assumed in this method to facilitate analysis. It allows the most probable value of modal parameters as well as the associated identification uncertainties to be determined. A Bayesian modal identification method with general coherence has also been developed in this work, which strictly obeys the proposed asynchronous data model. Synthetic and laboratory data are used to verify the proposed asynchronous data model and the identification methods. Field ambient vibration tests are also conducted and the proposed methods are applied to perform OMA. Specifically, this thesis is organised as follows:

In Chapter 2, the characteristics of asynchronous data are investigated through several laboratory experiments, which illustrate the potential issues encountered in OMA and help propose the asynchronous data model in the next chapter.

In Chapter 3, a probabilistic model for asynchronous ambient data is proposed inspired by the experimental findings in the last chapter. The model is conducive to analysis and modal identification while capturing key asynchronous properties through imperfect coherence in the frequency domain. The properties of the theoretical PSD matrix based on the asynchronous data modal are also investigated in this chapter.

In Chapter 4, a fast Bayesian modal identification method for asynchronous data is developed based on the proposed asynchronous data model in Chapter 3. Balancing model simplicity and utility, zero coherence is assumed in this method, which allows a fast iterative procedure to be proposed. The method provides an efficient way to determine the most probable value of modal parameters based on asynchronous ambient data. The identification uncertainty of modal parameters is also investigated.

In Chapter 5, a Bayesian modal identification method for asynchronous data with general coherence is developed. Compared to the fast algorithm proposed in Chapter 4, this method strictly obeys the asynchronous data model without approximation. It also allows the synchronisation degree to be quantified. Computational difficulties are addressed and dimension of matrix computation involved is suppressed, which allows the most probable value of modal parameters to be determined in reasonable time.

In Chapter 6, synthetic, laboratory and field data examples are presented to verify the consistency of the asynchronous data model and two modal identification methods proposed in previous chapters.

In Chapter 7, the proposed modal identification methods are applied to modal identification of a full-scale ambient vibration test incorporating multiple setups,

illustrating their feasibility for field test applications. Challenges encountered in field instrumentation are also discussed.

The thesis is concluded in Chapter 8 with suggestions for future work.

Chapter 2: Experimental Investigation of Asynchronous Data

The characteristics of asynchronous data are investigated through several laboratory experiments. The results are presented in this chapter, which help propose the asynchronous data model in the next chapter. The first example investigates the actual sampling rate of a DAQ system, illustrating the synchronisation issue caused by the clock jitter. Asynchronous data will cause errors in the identified modal parameters when using conventional modal identification methods that assume synchronous data. This issue is investigated in the second example using a multi-storey laboratory shear frame structure. Structure response data are measured in an asynchronous manner where multiple DAQ units are used without synchronisation. Modal identification has been conducted using a Bayesian FFT method for synchronous data and the identification results are compared with those identified based on synchronous data. In the third example, the behaviour of asynchronisation with measurement time is investigated based on the coherence of FFT data between two asynchronous data channels.

2.1 Sampling interval of DAQ system

The oscillator in a DAQ system can normally provide a high-precision time basis to control the data sampling procedure. However, the actual sampling interval may still have small variations due to the noise in the oscillator, which is caused by temperature, aging and other environmental variation [97]. Such variation is often referred as ‘clock jitter’. This is the main reason why simply controlling multiple DAQ units to start and finish recording at the same time will still cause synchronisation problems. The actual sampling intervals among the DAQ units are

not identical if they are running independently without synchronisation strategies. The clock jitter of the sampling clock in a DAQ unit is investigated in this example.

The instrumented DAQ unit is cDAQ-9171 from National Instruments. The time accuracy of this DAQ unit is 50ppm (parts per million), which only gives the accumulated time error over a measurement duration (e.g., 50ms of time error over a measurement duration of 1000s). In this example, the actual time intervals of this DAQ unit during the sampling procedure are investigated. The DAQ unit is used to measure the triangle wave signals generated by a signal generator with an amplitude of $\pm 4\mathrm{V}$. Signals with different frequencies are recorded, including [10 20 30 40 50 60]Hz. For each type of signal, 900s of digital data are recorded with a sampling rate 2048Hz. Based on the difference of two adjacent sampling points, the actual sampling interval between these two points can be estimated.

Figure 2.1-1 shows the histograms of the actual sampling intervals estimated based on different frequencies of triangle wave signals. Small values are filtered out when plotting the graphs as these values are obtained when the two points are on opposite sides of the signal peak. It can be seen that the actual sampling intervals vary randomly and do not follow any specific distributions. Multiple trials have also been conducted and the distribution of the actual sample intervals also varies even for a certain triangle wave signal. The standard deviations of the sampling intervals are calculated. They are of the same order of magnitude (around $5\times10^{-6}\mathrm{s}$) for all the measured signals, illustrating the time accuracy of the tested DAQ unit.

The characteristics of clock jitter have also been investigated by other researchers and different clock jitter models have been proposed [97,110–112]. Although the investigation method in this example is different from other research, the results are

in agreement that the clock jitter cannot be simply modelled based on any specific probability distributions.

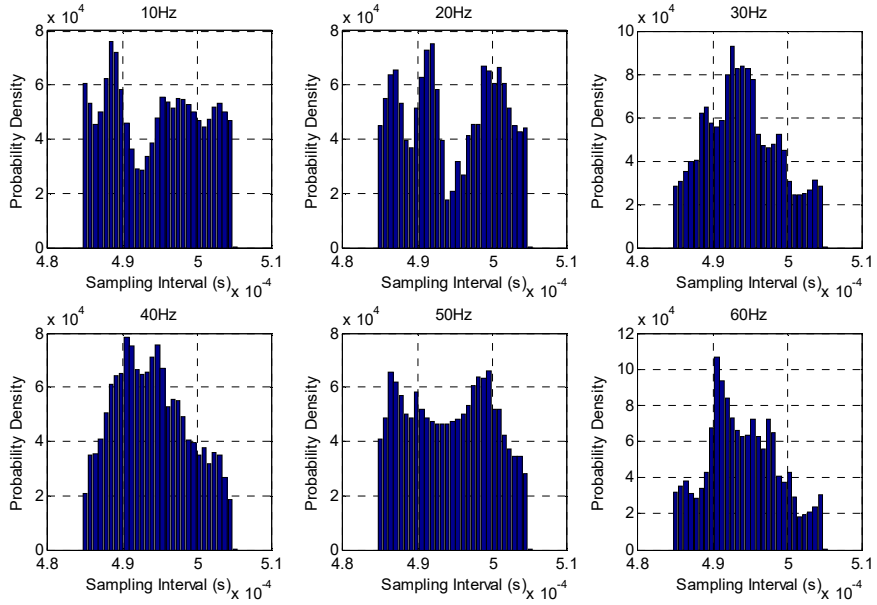

Figure 2.1-1. Histogram of sampling intervals with different signals

2.2 Effect of asynchronisation on OMA

In this example, the effect of time synchronisation problems on the modal identification results is investigated using real asynchronous data. Modal properties are identified using an existing algorithm that assumes synchronous data and the associated issues are discussed.

Consider a four-storey aluminium shear frame structure with a uniform storey height of 25cm and 30cm × 20cm in plan (as shown in *Figure 2.2-2*). Piezoelectric accelerometers are distributed at the centre of each floor, measuring the structure response under ambient condition in the weak direction. *Figure 2.2-3* shows the schematic diagram of the experimental setup. Sensor 1 to 4 are synchronised using one DAQ unit and Sensor 5 & 6 are synchronised using another. These two DAQ units are controlled to start and finish recording at the same time with a sampling

frequency of 2048Hz. The acceleration data measured from Sensor 1 to 4 is combined and referred as the synchronous data set. The data measured from Sensor {1,2,5,6} is combined and referred as the asynchronous data set, including two synchronous data groups. Thirty minutes of data are recorded and later decimated to 256Hz for analysis.

Figure 2.2-2. Four-storey laboratory shear frame model

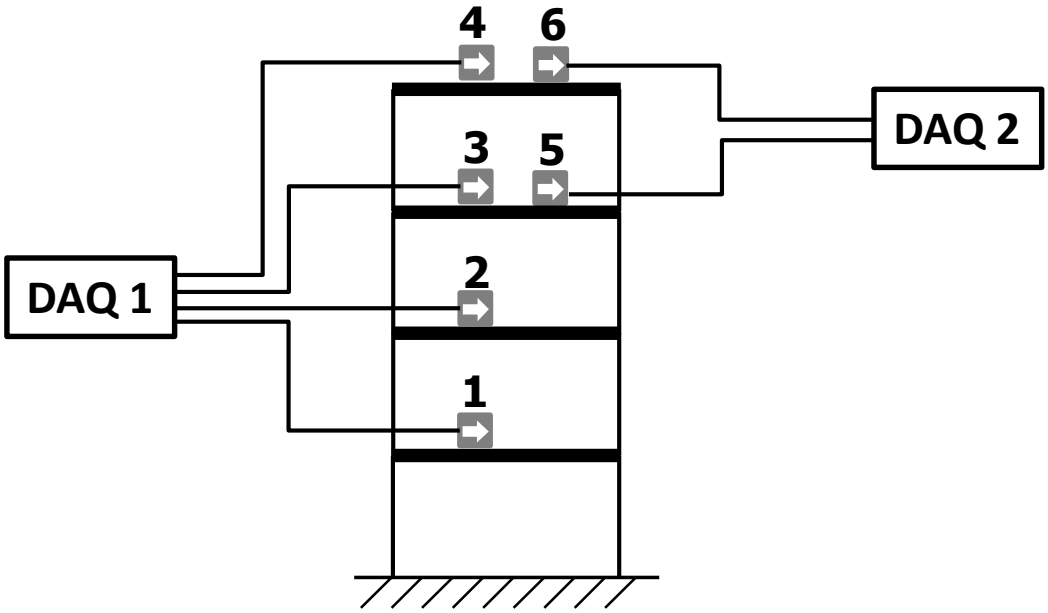

Figure 2.2-3. Experimental setup, laboratory shear frame model

Figure 2.2-4 and *Figure 2.2-5* show the root PSD spectrum for the synchronous and asynchronous data sets, respectively. Spectral peaks can be found in the spectrum for both cases, suggesting potential modes in the measured data. However, these two spectra look similar to each other. It is hard to detect the time synchronisation issue solely from the PSD spectrum. Significant differences can be found in the singular value (SV, the eigenvalues of PSD matrix) spectrum. *Figure 2.2-6* and *Figure 2.2-7* show the root SV spectrum for the synchronous and asynchronous data sets, respectively. For the synchronous case, the number of significant peaks in a resonance band reflects the number of modes in this band. In the root SV spectrum for the synchronous data set, there is only one significant peak within the resonance band of each mode, indicating five well-separated modes. This is not the case for the asynchronous data set, however. Two significant peaks can be found for each mode, which looks like there are two extremely close modes within the resonance band.

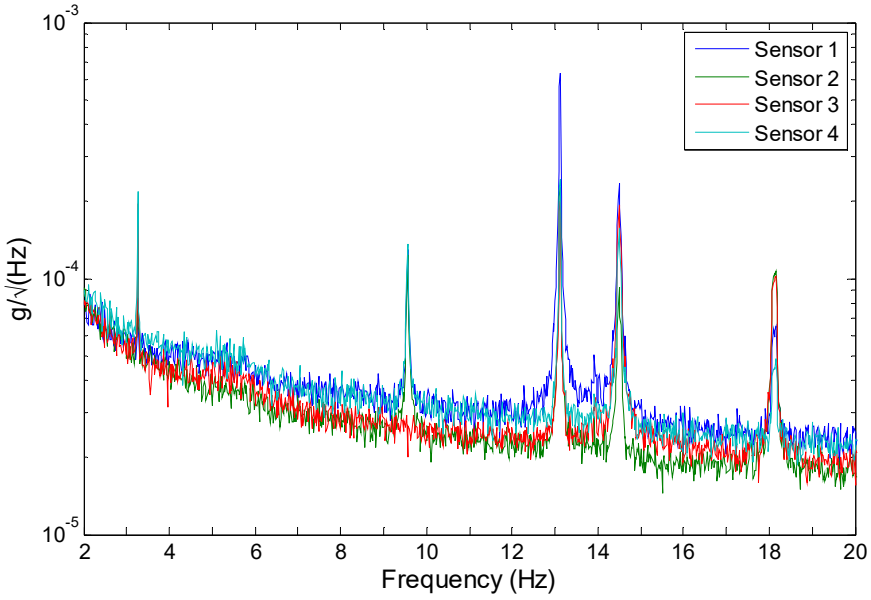

Figure 2.2-4. Root PSD spectrum of synchronous data set, laboratory shear frame model

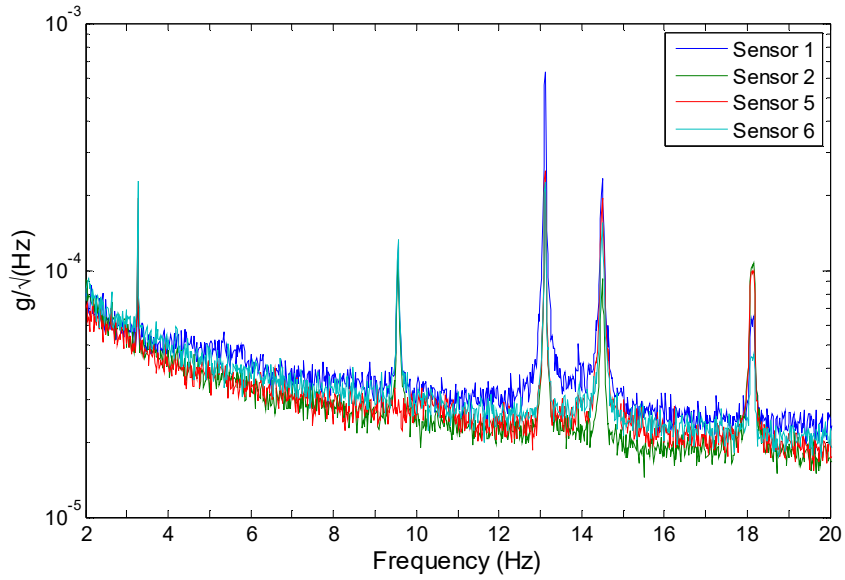

Figure 2.2-5. Root PSD spectrum of asynchronous data set, laboratory shear frame model

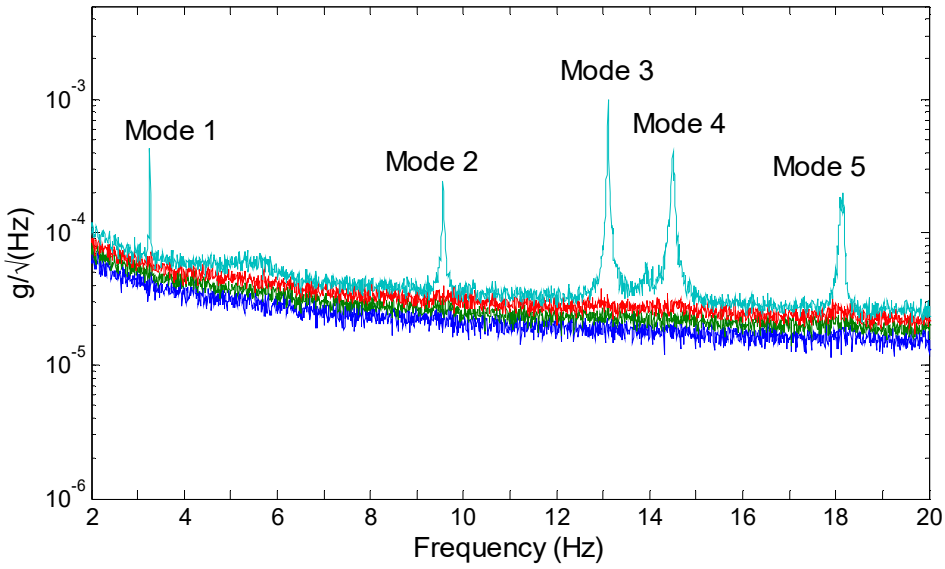

Figure 2.2-6. Root SV spectrum of synchronous data set, laboratory shear frame model

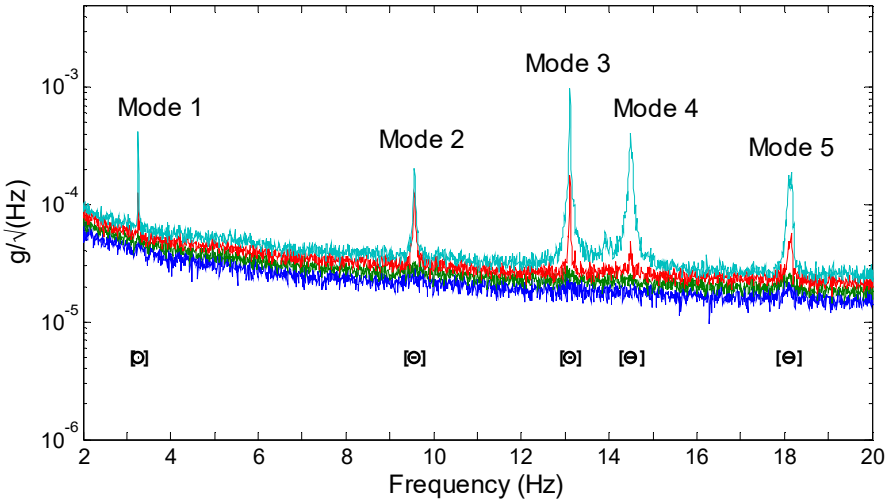

Figure 2.2-7. Root SV spectrum of asynchronous data set, laboratory shear frame model

Modal identification here focuses on these five modes shown in the spectrum. For both synchronous and asynchronous data sets, modal properties are identified using the Bayesian FFT method that assumes synchronous data [79,80]. The initial guess of natural frequencies and selected frequency bands for these modes are shown in *Figure 2.2-7* with a circle and the symbol '[-]', respectively. Same frequency bands and initial guesses are chosen for synchronous and asynchronous data sets. *Table 2.2-1* lists the identification results for these two data sets. The natural frequencies and damping ratios identified based on the asynchronous data set are close to those identified based on the synchronous data set. This is also the case for the modal force PSD. However, the prediction error PSDs identified based on the asynchronous data set are larger than their synchronous counterparts. This is a reflection of modelling error due to time synchronisation problems. Major discrepancies can be found in the identified mode shapes. *Figure 2.2-8* shows the identified mode shapes for both synchronous (solid lines) and asynchronous data sets (squares). It can be seen that except the first mode, the relative directions of the mode shape on the third and fourth floor for the asynchronous data set are not correctly identified. There are also

errors in the identified mode shape values, especially on the first and second floor for Mode 1 and 2.

Table 2.2-1 Identification results for synchronous and asynchronous data set

Parameter	Mode	Synchronous Data Set	Asynchronous Data Set
$f\ (\mathrm{Hz})$	1	3.260	3.260
	2	9.559	9.560
	3	13.10	13.10
	4	14.50	14.50
	5	18.13	18.13
$\zeta\ (\%)$	1	0.07	0.07
	2	0.15	0.11
	3	0.04	0.04
	4	0.15	0.15
	5	0.22	0.22
$\sqrt{S}\ (\mu g/\sqrt{\mathrm{Hz}})$	1	0.89	0.89
	2	0.76	0.50
	3	1.03	1.00
	4	1.21	1.19
	5	0.83	0.77
$\sqrt{S_e}\ (\mu g/\sqrt{\mathrm{Hz}})$	1	54.1	78.2
	2	28.1	54.4
	3	25.1	58.6
	4	23.5	24.9
	5	22.0	29.1

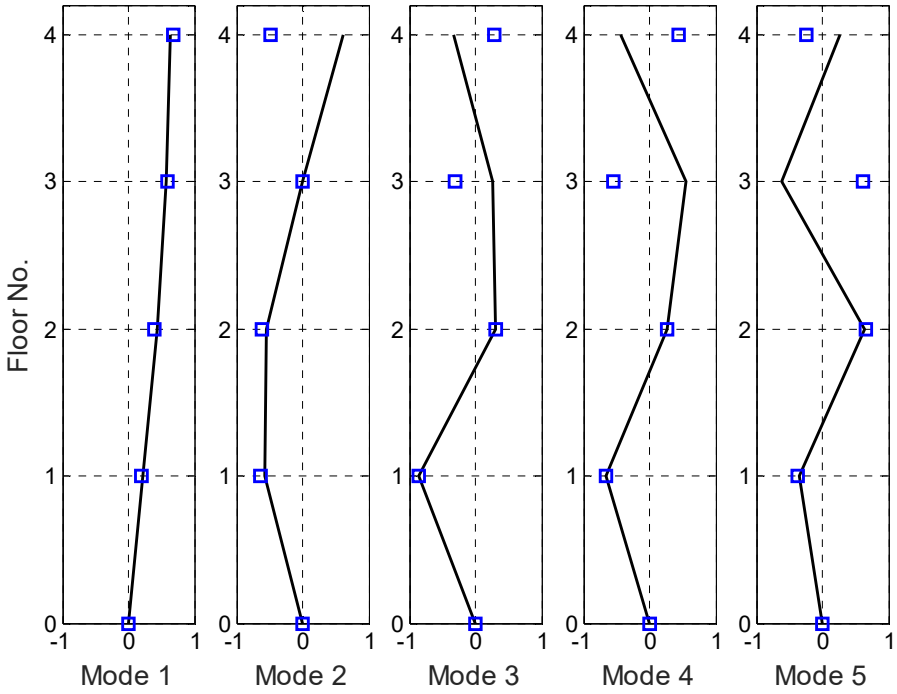

Figure 2.2-8. Identified mode shapes (solid line: synchronous data; square: asynchronous data based on conventional method)

It can be seen that the identified natural frequencies and damping ratios are not severely affected even when asynchronous data are (inappropriately) processed using a modal identification method that assumes synchronous data. The main error lies in the identified mode shapes, where both the relative scaling and directions among the synchronous data groups may be erroneously determined.

2.3 Asynchronisation against measurement duration

The asynchronisation characteristics in OMA against measurement duration are investigated in this example. Consider a one-storey shear frame. Three accelerometers are distributed at the centre of the first floor measuring the acceleration response of the structure in the weak direction (as shown in *Figure 2.3-9*). The first sensor is used as the reference sensor. The second sensor is synchronised with the first sensor by connecting them to the same DAQ unit. The

third sensor is connected to another DAQ unit. These two DAQ units are controlled to start and finish recording at the same time. One hour of ambient acceleration response of the structure is measured. The measured data from the first and second sensor are combined and referred as the synchronous data set while those from the first and third sensor are combined and referred as the asynchronous data set. The data are sampled at 2048Hz and decimated to 256Hz for analysis.

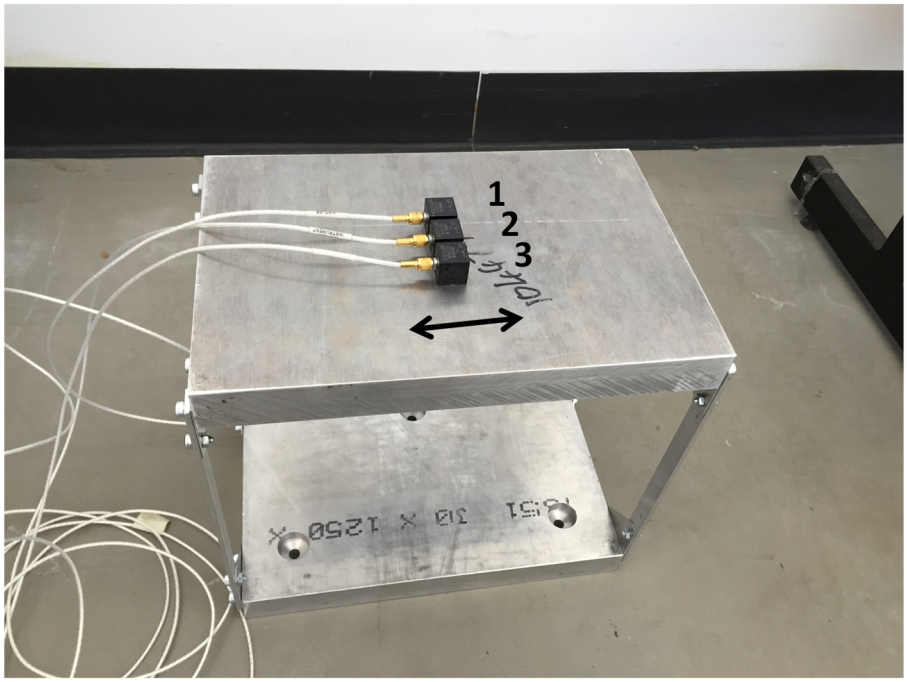

Figure 2.3-9. Single-storey laboratory shear frame model with sensors

Figure 2.3-10 shows the root SV spectrum for both synchronous and asynchronous data sets. Spectral peaks can be found around 10Hz in both cases, illustrating the presence of a mode. Similar to previous examples, there is only one spectral peak for the synchronous data set while multiple peaks can be found for the asynchronous data set. To investigate the characteristics of asynchronisation, the data are chopped into different measurement durations from the start for both cases. For each sequence of data, it is averaged over 10 non-overlapping segments to estimate the coherence of their FFT values around the resonance peak of the mode. Around the resonance peak

of the mode, the FFT of measured data is dominated by structural responses and the coherence between the data channels measuring the same DOFs can hence reflect the asynchronisation characteristics in the measured ambient data. In this experiment, the average coherence value is discussed based on the resonance frequency band selected as [10.1 10.3]Hz.

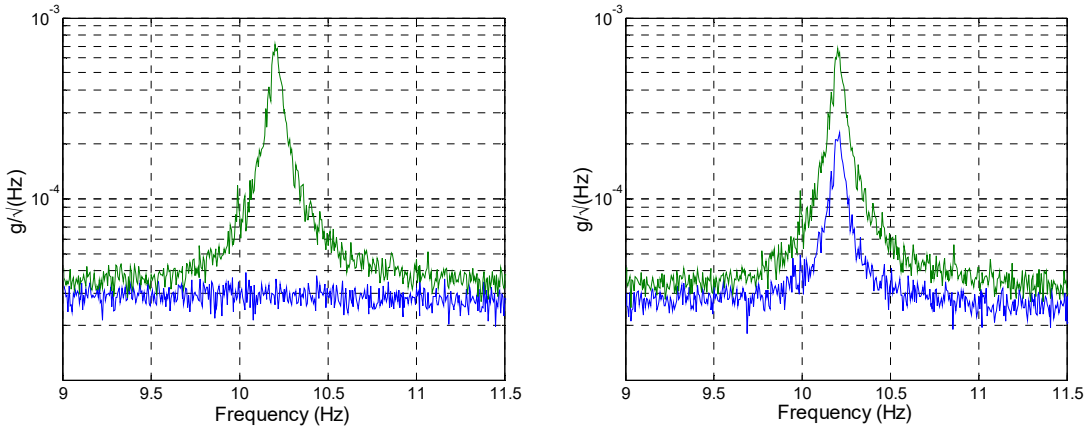

Figure 2.3-10. Root SV spectrum of (a) synchronous and (b) asynchronous data

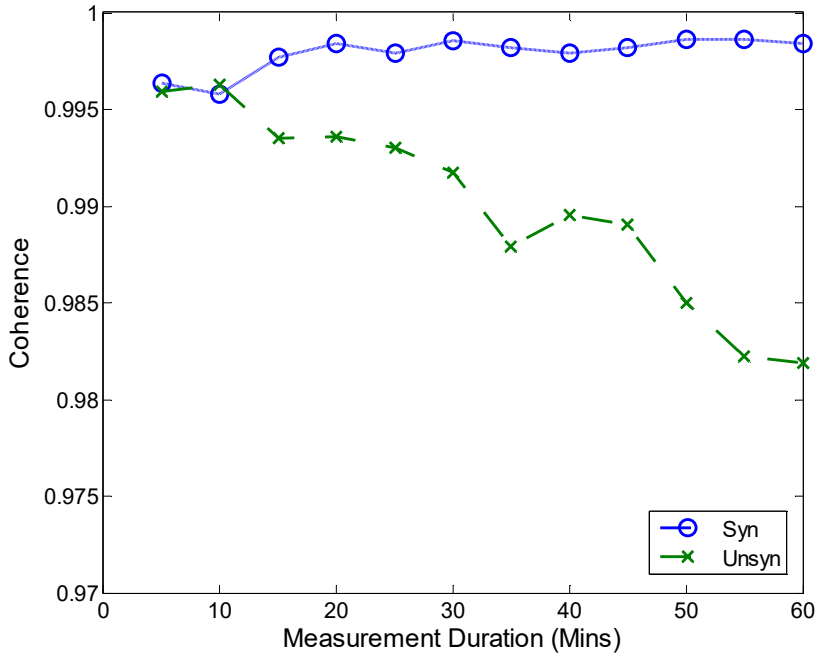

Figure 2.3-11. Norm of coherence against measurement duration

Figure 2.3-11 shows the norm of the coherence value against the measurement duration for both synchronous and asynchronous data set. It can be seen that the norm of the coherence is very close to 1 regardless the measurement duration of the data for the synchronous data set. However, there is a decrease for the asynchronous data set when the measurement duration increases, suggesting a decrease of the synchronisation degree between the two measured data channels.

2.4 Discussion

This chapter has illustrated the properties of asynchronous data based on several laboratory tests. It is shown that due to the clock jitter, the actual sampling interval of a DAQ unit varies randomly and does not follow any specific distributions. Using conventional OMA methods that assume synchronous data does not cause significant errors in identifying the natural frequencies and damping ratios when the measured data has time synchronisation problems. However, the mode shapes cannot be correctly identified by conventional methods with errors in the relative scaling and directions between different synchronous data groups. The coherence between two asynchronous data channels decreases with the increase of measurement duration, illustrating a decrease of the synchronisation degree between the channels. The experimental findings in this chapter provide some insights on the asynchronous data in OMA, which help propose the asynchronous data model in the next chapter.

Chapter 3: Modelling Asynchronous Data in OMA

Motivated by the experimental findings in the last chapter, a mathematical model is proposed in this chapter for asynchronous data in OMA. Time synchronisation problem in the measured data normally results from two aspects, the initial time shift (start time) between data channels and the random time drifts due to 'clock jitter' (from the noise of individual time-measuring oscillators). The initial time shift can be detected and compensated using existing time delay estimation techniques [113,114]. This work focuses on the latter. Compared to the nominal sampling interval, the random time drifts are relatively small. However, it cannot be aligned after the digital data are sampled. Furthermore, the time errors caused by the drifts are accumulated over time, which leads to the non-stationary behaviour of the sampled asynchronous data [115,116]. Generally, modelling a non-stationary process is much more difficult compared to a stationary one. To balance simplicity and utility, a stationary stochastic model with imperfect coherence in the frequency domain is proposed for asynchronous ambient data in this work. It is conducive to analysis and modal identification while capturing key asynchronous characteristics within suitable time scales.

Time histories of ambient vibration data look erratic as the structure is subjected to different excitation sources (e.g. wind, microtremor, cultural activities) with a variety of frequency characteristics. Working in the frequency domain provides an effective means where activities of different frequency characteristics can be analysed separately. Recall that minimising the NLLF involves calculating the inverse and determinant of the PSD matrix with different trials, it is necessary to investigate the eigenvalue and eigenvector properties of the PSD matrix so that its determinant and

inverse can be expressed in better forms to facilitate computations. The eigenvalues of the PSD matrix are also used to plot the 'singular value (SV) spectrum'. Investigating the eigenvalue properties of PSD matrix helps gain more insights on detecting the number of modes and synchronisation issues in the frequency band.

For instructional purposes, the ambient data model for synchronous data model is first reviewed in this section. The properties of the PSD matrix for synchronous data are also investigated, which will be later compared with their asynchronous counterparts in this chapter. The probabilistic model for asynchronous ambient data is then proposed and the characteristics of the corresponding PSD matrix are investigated. The proposed model provides a cornerstone for the Bayesian modal identification methods of asynchronous ambient data to be proposed in the following chapters.

3.1 Properties of PSD matrix for synchronous data

Without loss of generality, let the measured acceleration data be $\left\{\ddot{\mathbf{x}}_j \in R^n\right\}_{j=1}^N$ with n measured DOFs and N sampling points in each data channel. It is assumed to consist of theoretical structural response $\ddot{\mathbf{x}}_j$ under ambient excitation and prediction error $\boldsymbol{\varepsilon}_j$ due to measurement noise or modelling error:

$$\hat{\ddot{\mathbf{x}}}_j = \ddot{\mathbf{x}}_j + \boldsymbol{\varepsilon}_j \tag{8}$$

Consider a frequency band dominated by a single mode, the FFT of measured data within the band can be modelled as:

$$\mathcal{F}_k = \boldsymbol{\varphi}\ddot{\eta}_k + \boldsymbol{\varepsilon}_k \tag{9}$$

where $\boldsymbol{\varphi}$ is the mode shape and $\ddot{\eta}_k$ denotes the FFT of modal response $\ddot{\eta}(t)$; $\boldsymbol{\varepsilon}_k$ is the scaled FFT of measurement noise. Assuming classically damped system, the modal response $\ddot{\eta}(t)$ follows the modal equation of motion:

$$\ddot{\eta}(t) + 2\zeta\omega\dot{\eta}(t) + \omega^2\eta(t) = p(t) \tag{10}$$

where $\omega = 2\pi f$ (rad/s); f (Hz) and ζ are the natural frequency and damping ratio of the mode, respectively; $p(t)$ is the modal force. In the resonance band of the mode, the modal force is normally modelled as a stationary process with a constant PSD S and measurement error as independent and identically (i.i.d.) Gaussian white noise with a constant PSD S_e. Post-multiplying $\mathcal{F}_k$ in Eq.(9) by its conjugate transpose and taking expectation gives the theoretical PSD matrix:

$$\mathbf{E}_k = \mathrm{E}[\mathcal{F}_k\mathcal{F}_k^*] = SD_k\boldsymbol{\varphi}\boldsymbol{\varphi}^T + S_e\mathbf{I}_n \tag{11}$$

where

$$D_k = \left[\left(\beta_k^2 - 1\right)^2 + \left(2\zeta\beta_k\right)^2\right]^{-1} \qquad \beta_k = f/\mathrm{f}_k \tag{12}$$

is the dynamic amplification factor.

The PSD spectrum is a plot of the diagonal elements of $\mathbf{E}_k$ with frequency f_k. A peak in the spectrum indicates the presence of a mode. However, it does not necessarily indicate the number of modes. For example, the PSD spectrum of two data channels measuring the same DOF has two almost identical peaks around the natural frequency of a single mode. The number of modes is reflected in the plot of eigenvalues of $\mathbf{E}_k$, conventionally referred as the SV spectrum. The eigenvalues are

related to dynamic amplification and eigenvectors to mode shapes. To see this, consider an orthonormal basis $B = \{\mathbf{a}_j \in R^n\}_{j=1}^n$ with $\mathbf{a}_1 = \boldsymbol{\varphi} \in R^n$ (assuming $\|\boldsymbol{\varphi}\|^2 = 1$). Using this basis, the identity matrix can be written as $\mathbf{I}_n = \sum_{j=1}^n \mathbf{a}_j \mathbf{a}_j^T$. Substituting into Eq.(11) gives the eigenvector representation of $\mathbf{E}_k$:

$$\mathbf{E}_k = \underbrace{(SD_k + S_e)}_{Eigenvalue} \mathbf{a}_1 \mathbf{a}_1^T + \sum_{j=2}^{n} \underbrace{S_e}_{Eigenvalue} \mathbf{a}_j \mathbf{a}_j^T \tag{13}$$

This indicates that, for a well-separated mode, the largest eigenvalue of the PSD matrix near the natural frequency is equal to $SD_k + S_e$ with eigenvector $\boldsymbol{\varphi}$. The remaining $(n-1)$ eigenvalues are all equal to S_e, reflecting the noise level. In the general case where there can be more than one mode in the band, the number of eigenvalues significantly larger than the remaining ones indicates the dimension of the subspace spanned by the mode shapes, i.e., 'mode shape subspace' [79].

3.2 Probabilistic model for asynchronous data

To model asynchronous data in OMA, recall Eq.(9) that applies for synchronous data. The same spectral properties can be assumed for the measurement noise $\boldsymbol{\varepsilon}_k$ as they are independent regardless of synchronisation issue. The difference lies in the modal responses $\ddot{\eta}_k$. For asynchronous data, the measured modal responses at different channels need not follow the same time variation because of the synchronisation problems.

Assume that the test configuration on time synchronisation are given (i.e., the corresponding channels that uses the same sampling clocks are known), which is typically the case in real applications. Define a 'synchronous data groups' as a set of

data channels that record the structural responses based on the same sampling clock. Let n_g denote the total number of synchronous data groups in the whole measurement array. For the overall mode shape $\boldsymbol{\varphi}$, let $\mathbf{u}_i \in R^{n_i}$ $\left(i = 1,..., n_g\right)$ denote the part of $\boldsymbol{\varphi}$ measured by Group i and $\ddot{\eta}_{ki}$ be the FFT of the associated modal acceleration responses, where n_i is the number of measured DOFs in Group i. The FFT of measured asynchronous data now can be expressed as:

$$\mathcal{F}_k = \begin{bmatrix} \mathbf{u}_1 \ddot{\eta}_{k1} \\ \vdots \\ \mathbf{u}_{n_g} \ddot{\eta}_{kn_g} \end{bmatrix} + \boldsymbol{\varepsilon}_k \tag{14}$$

The modal responses $\ddot{\eta}_{ki}$ among different synchronous data groups should still satisfy the modal equation of motion, i.e.,

$$\ddot{\eta}_i(t) + 2\zeta\omega\dot{\eta}_i(t) + \omega^2\eta_i(t) = p_i(t) \qquad i = 1,..., n_g \tag{15}$$

where $p_i(t)$ is the measured modal force associated with the ith synchronous data group. For synchronous data, $p_i(t)$ among different synchronous data groups would have been identical and hence $\ddot{\eta}_{ki}$. This is not the case for asynchronous data, however. Assume the same measurement duration for all the groups while the sampling clocks among different synchronous data groups run independently without synchronisation protocol. The measured modal force among these groups can be assumed as identically distributed, i.e.,

$$\mathrm{E}\left(p_{ki} p_{ki}^*\right) = S \qquad i = 1,..., n_g \tag{16}$$

such that

$$\mathrm{E}\left(\ddot{\eta}_{ki}\ddot{\eta}_{ki}^{*}\right)=SD_k \qquad i=1,\ldots,n_g \tag{17}$$

The major difficulty lies in modelling the relationship among $\ddot{\eta}_{ki}$ as asynchronous data fundamentally is a non-stationary process. Balancing model simplicity and utility, a stationary stochastic model is proposed where the asynchronous nature of data among different groups is empirically modelled through imperfect coherence:

$$\chi_{kij}=\frac{\mathrm{E}\left(\ddot{\eta}_{ki}\ddot{\eta}_{kj}^{*}\right)}{\sqrt{\mathrm{E}\left(\ddot{\eta}_{ki}\ddot{\eta}_{ki}^{*}\right)\mathrm{E}\left(\ddot{\eta}_{kj}\ddot{\eta}_{kj}^{*}\right)}} \tag{18}$$

where $\chi_{kij}\in C$ ($\left|\chi_{kij}\right|\le 1$) is the coherence between ith and jth group at frequency f_k. This model is justified for frequencies that are small compared to the reciprocal of the random time difference (drift) between the sampling clocks of different groups.

The resulting PSD matrix for asynchronous data now can be written as:

$$\mathbf{E}_k=\mathrm{E}\left(\mathcal{F}_k\mathcal{F}_k^{*}\right)=SD_k\begin{bmatrix}\mathbf{u}_1\mathbf{u}_1^T & \chi_{k12}\mathbf{u}_1\mathbf{u}_2^T & \cdots & \chi_{k1n_g}\mathbf{u}_1\mathbf{u}_{n_g}^T\\ \chi_{k21}\mathbf{u}_2\mathbf{u}_1^T & \mathbf{u}_2\mathbf{u}_2^T & & \vdots\\ \vdots & & \ddots & \vdots\\ \chi_{kn_g1}\mathbf{u}_{n_g}\mathbf{u}_1^T & \cdots & \cdots & \mathbf{u}_{n_g}\mathbf{u}_{n_g}^T\end{bmatrix}+S_e\mathbf{I}_n \tag{19}$$

The diagonal partitions of the PSD matrix $\mathbf{E}_k$ for asynchronous data are the same as their synchronous counterparts (see Eq.(11)), which do not reveal the asynchronous nature of data. The latter is reflected in the off-diagonal partitions through the coherence parameters $\{\chi_{kij}\}$. The eigenvalue properties of $\mathbf{E}_k$ for asynchronous data will be investigated in the next section.

3.3 Properties of PSD matrix for asynchronous data

The eigenvalues and eigenvectors of the PSD matrix for asynchronous data are investigated in this section. It also helps express the determinant and inverse of the

PSD matrix in better forms that can facilitate computations when developing modal identification algorithms for asynchronous ambient data.

Define a matrix $\mathbf{C}_k \in C^{n_g \times n_g}$ that contains the norm of partial mode shapes and coherence values among the synchronous data groups:

$$\begin{aligned}\mathbf{C}_k &= diag\left\{\left\|\mathbf{u}_i\right\|\right\}_{i=1}^{n_g} \boldsymbol{\chi}_k diag\left\{\left\|\mathbf{u}_i\right\|\right\}_{i=1}^{n_g} \\ &= \begin{bmatrix} \left\|\mathbf{u}_1\right\|\left\|\mathbf{u}_1\right\| & \chi_{k12}\left\|\mathbf{u}_1\right\|\left\|\mathbf{u}_2\right\| & \cdots & \chi_{k1n_g}\left\|\mathbf{u}_1\right\|\left\|\mathbf{u}_{n_g}\right\| \\ \chi_{k21}\left\|\mathbf{u}_2\right\|\left\|\mathbf{u}_1\right\| & \left\|\mathbf{u}_2\right\|\left\|\mathbf{u}_2\right\| & & \vdots \\ \vdots & & \ddots & \vdots \\ \chi_{kn_g1}\left\|\mathbf{u}_{n_g}\right\|\left\|\mathbf{u}_1\right\| & \cdots & \cdots & \left\|\mathbf{u}_{n_g}\right\|\left\|\mathbf{u}_{n_g}\right\| \end{bmatrix}\end{aligned} \tag{20}$$

where $diag\left\{\left\|\mathbf{u}_i\right\|\right\}_{i=1}^{n_g}$ denotes a diagonal matrix with entries $\left\{\left\|\mathbf{u}_i\right\|\right\}_{i=1}^{n_g}$ and $\boldsymbol{\chi}_k$ denotes a $n_g \times n_g$ matrix with (i, j) entry χ_{kij}. The PSD matrix for asynchronous data then can be expressed in a structured form as:

$$\mathbf{E}_k = SD_k \mathbf{U}\mathbf{C}_k\mathbf{U}^T + S_e\mathbf{I}_n \tag{21}$$

where $\mathbf{U} \in R^{n \times n_g}$ is a block-diagonal matrix formed by the normalised partial mode shapes $\left\{\mathbf{u}_i / \left\|\mathbf{u}_i\right\|\right\}_{i=1}^{n_g}$:

$$\mathbf{U} = \begin{bmatrix} \mathbf{u}_1 / \left\|\mathbf{u}_1\right\| & & \\ & \ddots & \\ & & \mathbf{u}_{n_g} / \left\|\mathbf{u}_{n_g}\right\| \end{bmatrix} \tag{22}$$

Let $\left\{\lambda_{ki} \geq 0\right\}_{i=1}^{n_g}$ and $\left\{\mathbf{c}_{ki} = \left[c_{k1i}, \cdots, c_{kn_gi}\right]^T \in C^{n_g}\right\}_{i=1}^{n_g}$ be the eigenvalues and eigenvectors (with unit norm) of $\mathbf{C}_k$. Then

$$\mathbf{C}_k = \sum_{i=1}^{n_g} \lambda_{ki} \mathbf{c}_{ki} \mathbf{c}_{ki}^* \tag{23}$$

Substituting Eq.(23) into Eq.(21) gives:

$$\mathbf{E}_k = \sum_{i=1}^{n_g} SD_k \lambda_{ki} \boldsymbol{\alpha}_{ki} \boldsymbol{\alpha}_{ki}^* + S_e \mathbf{I}_n \tag{24}$$

where

$$\boldsymbol{\alpha}_{ki} = \mathbf{U}\mathbf{c}_{ki} = \begin{bmatrix} c_{k1i} \dfrac{\mathbf{u}_1}{\|\mathbf{u}_1\|} \\ \vdots \\ c_{kn_g i} \dfrac{\mathbf{u}_{n_g}}{\|\mathbf{u}_{n_g}\|} \end{bmatrix} \qquad i = 1,..., n_g \tag{25}$$

Using $\mathbf{U}^T\mathbf{U} = \mathbf{I}_{n_g}$ and the orthonormal properties of $\{\mathbf{c}_{ki}\}_{i=1}^{n_g}$, i.e., $\mathbf{c}_{ki}^*\mathbf{c}_{ki} = 1$ and $\mathbf{c}_{ki}^*\mathbf{c}_{kj} = 0 \ (i \neq j)$, it is easy to see that $\{\boldsymbol{\alpha}_{ki}\}_{i=1}^{n_g}$ form an orthonormal basis in a n_g-dimensional subspace of C^n. Define an orthonormal basis $\{\mathbf{a}_{ki}\}_{i=1}^{n}$ in C^n where $\mathbf{a}_{ki} = \boldsymbol{\alpha}_{ki}$ ($i = 1,..., n_g$) and let $\{\mathbf{a}_{ki}\}_{i=n_g+1}^{n}$ be an orthonormal basis in the orthogonal complement of this subspace. Note that $\mathbf{I}_n = \sum_{i=1}^{n} \mathbf{a}_{ki}\mathbf{a}_{ki}^*$, the eigenvector representation of $\mathbf{E}_k$ is then given by:

$$\mathbf{E}_k = \sum_{i=1}^{n_g} \underbrace{\left(SD_k \lambda_{ki} + S_e\right)}_{Eigenvalue} \mathbf{a}_{ki}\mathbf{a}_{ki}^* + \sum_{i=n_g+1}^{n} \underbrace{S_e}_{Eigenvalue} \mathbf{a}_{ki}\mathbf{a}_{ki}^* \tag{26}$$

The determinant and inverse of $\mathbf{E}_k$ then can be expressed as:

$$\det \mathbf{E}_k = S_e^{n-n_g} \prod_{i=1}^{n_g} \left(SD_k \lambda_{ki} + S_e\right) \tag{27}$$

and

$$\mathbf{E}_k^{-1} = \sum_{i=1}^{n_g} \left(SD_k \lambda_{ki} + S_e \right)^{-1} \mathbf{a}_{ki} \mathbf{a}_{ki}^* + \sum_{i=n_g+1}^{n} S_e^{-1} \mathbf{a}_{ki} \mathbf{a}_{ki}^* \tag{28}$$

The foregoing results illustrate the differences between synchronous and asynchronous data in the frequency domain. As shown in Eq.(13), there is only one significant eigenvalue $SD_k + S_e$ for synchronous data, indicating only one spectral peak around the resonance band of the mode in the SV spectrum. The remaining ones are all equal to S_e, which reflect the noise level of measured data. The eigenvector corresponding to this eigenvalue directly gives the global mode shape $\boldsymbol{\varphi}$.

This is not the case for asynchronous data, however. There are n_g significant eigenvalues $\{SD_k \lambda_{ki} + S_e\}_{i=1}^{n_g}$ of the PSD matrix for asynchronous data. Due to the common dynamic amplification factor D_k, n_g spectral peaks with the same frequency variation can be found in the SV spectrum for asynchronous data, which appear as several extremely close modes with almost identical damping. These eigenvalues are also proportional to $\{\lambda_{ki}\}_{i=1}^{n_g}$ (eigenvalues of $\mathbf{C}_k$ in Eq.(20)), which depend non-trivially on the coherence χ_{kij} between different groups and the norms of the partial mode shapes $\{\mathbf{u}_i\}_{i=1}^{n_g}$.

Finally, the global mode shape cannot be directly obtained based on the eigenvectors of the PSD matrix for asynchronous data. According to Eq.(25), the partition of the eigenvectors $\boldsymbol{\alpha}_{ki}$ regarding to a particular synchronous data group j can still give the normalised partial mode shape $\mathbf{u}_j / \|\mathbf{u}_j\|$. However, the relative scaling between the partial mode shapes depends in a non-trivial manner on $\{\mathbf{c}_{ki}\}_{i=1}^{n_g}$ (the eigenvectors of

$\mathbf{C}_k$). The latter varies with the norm of partial mode shapes $\left\{\left\|\mathbf{u}_i\right\|\right\}_{i=1}^{n_g}$ as well as the coherence χ_k.

Chapter 4: Bayesian Method with Zero Coherence Assumption

Based on the proposed asynchronous data model in the last chapter, a fast Bayesian modal identification method for asynchronous ambient data with zero coherence assumption is proposed in this chapter. Determining the most probable value of modal parameters requires minimising the NLLF, which involves the computation of the inverse and determinant of the theoretical PSD matrix $\mathbf{E}_k$ in Eq.(19) for different trials of modal parameters $\boldsymbol{\theta}$. As is typical in developing efficient modal identification algorithms, it is better to express these two terms in analytically tractable forms to facilitate computations instead of resorting to brute-force numerical optimisation. As shown in the last section, the inverse and determinant of the PSD matrix $\mathbf{E}_k$ for asynchronous data depend in a non-trivial manner on the coherence values among different synchronous data groups. It is difficult to express their analytical forms with respect to modal parameters directly. Balancing model simplicity and utility, zero coherence among different synchronous data groups is assumed for the proposed method in this chapter to facilitate computation. Based on this assumption, a fast iterative procedure is developed for determining the most probable value of modal parameters based on asynchronous ambient data. The analytical expressions of the posterior covariance matrix (inverse of the Hessian of NLLF) are also derived, which allows the identification uncertainty of modal parameters to be quantified.

4.1 Formulation of the NLLF

Recall the theoretical PSD matrix for asynchronous data in Eq.(19) and assume zero coherence between different synchronous data groups, the coherence matrix $\boldsymbol{\chi}_k$ now becomes an identity matrix and the resulting $\mathbf{E}_k$ has a block-diagonal form given by

$$\mathbf{E}_k = \begin{bmatrix} \mathbf{E}_{1k} & \mathbf{0} & \cdots & \mathbf{0} \\ \mathbf{0} & \mathbf{E}_{2k} & & \vdots \\ \vdots & & \ddots & \mathbf{0} \\ \mathbf{0} & \cdots & \mathbf{0} & \mathbf{E}_{n_g k} \end{bmatrix} \tag{29}$$

where

$$\mathbf{E}_{ik} = SD_k c_i \overline{\mathbf{u}}_i \overline{\mathbf{u}}_i^T + S_{ei} \mathbf{I}_{n_i} \tag{30}$$

and

$$\overline{\mathbf{u}}_i = \frac{\mathbf{u}_i}{\|\mathbf{u}_i\|} \tag{31}$$

$$c_i = \|\mathbf{u}_i\|^2 \tag{32}$$

The determinant and inverse of $\mathbf{E}_k$ can be expressed in terms of $\mathbf{E}_{ik}$ as

$$\det(\mathbf{E}_k) = \prod_{i=1}^{n_g} \det(\mathbf{E}_{ik}) \tag{33}$$

$$\mathbf{E}_k^{-1} = \begin{bmatrix} \mathbf{E}_{1k}^{-1} & \mathbf{0} & \cdots & \mathbf{0} \\ \mathbf{0} & \mathbf{E}_{2k}^{-1} & & \vdots \\ \vdots & & \ddots & \mathbf{0} \\ \mathbf{0} & \cdots & \mathbf{0} & \mathbf{E}_{n_g k}^{-1} \end{bmatrix} \tag{34}$$

Substituting Eq.(33) and Eq.(34) into the NLLF in Eq.(6), the resulting NLLF now can be given by:

$$L = \sum_{i=1}^{n_g} L_i \tag{35}$$

with

$$L_i = \sum_k \ln\left(\det\left(\mathbf{E}_{ik}\right)\right) + \sum_k \mathcal{F}_{ik}{}^{*}\mathbf{E}_{ik}^{-1}\mathcal{F}_{ik} \tag{36}$$

where $\mathcal{F}_{ik}$ is the corresponding partition of $\mathcal{F}_k$ for the ith synchronous group.

Note that $\mathbf{E}_{ik}$ has a similar form of $\mathbf{E}_k$ for synchronous data, its determinant and inverse can be expressed by its eigenspace decomposition. Define an orthonormal basis $B = \left\{\mathbf{a}_j \in R^{n_i}\right\}_{j=1}^{n_i}$ where $\mathbf{a}_1 = \overline{\mathbf{u}}_i \in R^{n_i}$ and let $\left\{\mathbf{a}_j \in R^{n_i}\right\}_{j=2}^{n_i}$ be an orthonormal basis in the orthogonal complement of the subspace spanned by $\mathbf{a}_1$. Using this basis, the identity matrix can be expressed as $\mathbf{I}_{n_i} = \sum_{j=1}^{n_i} \mathbf{a}_j\mathbf{a}_j^T$ and $\mathbf{E}_{ik}$ can be given by

$$\mathbf{E}_{ik} = \underbrace{\left(SD_k c_i + S_e\right)}_{Eigenvalue}\mathbf{a}_1\mathbf{a}_1^T + \sum_{j=2}^{n_i} \underbrace{S_e}_{Eigenvalue}\mathbf{a}_j\mathbf{a}_j^T \tag{37}$$

The determinant of $\mathbf{E}_{ik}$ is simply the product of the eigenvalues, i.e.,

$$\det\left(\mathbf{E}_{ik}\right) = \left(SD_k c_i + S_{ei}\right) S_{ei}^{n_i - 1} \tag{38}$$

and inverse of $\mathbf{E}_{ik}$ has the same eigenvectors but reciprocal of eigenvalues:

$$\mathbf{E}_{ik}^{-1} = S_{ei}^{-1}\mathbf{I}_n - S_{ei}^{-1}\left(1 + S_{ei} / SD_k c_i\right)^{-1}\overline{\mathbf{u}}_i\overline{\mathbf{u}}_i^T \tag{39}$$

Substituting Eq.(38) and Eq.(39) into Eq.(36) gives the resulting NLLF as:

$$L_i = \left(n_i - 1\right)N_f \ln S_{ei} + \sum_k \ln\left(SD_k c_i + S_{ei}\right) + S_{ei}^{-1}\left(d_i - \overline{\mathbf{u}}_i^T\mathbf{A}_i\overline{\mathbf{u}}_i\right) \tag{40}$$

where

$$d_i = \sum_k \mathcal{F}_{ik}^* \mathcal{F}_{ik} \tag{41}$$

and

$$\mathbf{A}_i = \sum_k \left(1 + S_{ei} / SD_k c_i\right)^{-1} \mathbf{D}_{ik} \tag{42}$$

$$\mathbf{D}_{ik} = \mathcal{F}_{ik} \mathcal{F}_{ik}^* \tag{43}$$

4.2 Fast algorithm for most probable value

Based on the NLLF with zero coherence assumptions, a fast modal identification algorithm is proposed in this section for efficient determination of the MPV of modal parameters. Some of the parameters in the NLLF are subjected to constraints. Instead of applying these constraints into the optimisation procedure using numerical techniques (e.g., Lagrange multiplier), a parameterisation scheme is first proposed to automatically take care of the constraints. As the NLLF is a quadratic form of the partial mode shape $\overline{\mathbf{u}}_i$ for each synchronous group, the MPV of the partial mode shape $\overline{\mathbf{u}}_i$ can be obtained by solving eigenvalue problems given the remaining parameters. This leads to an iterative procedure to be proposed. The resulting identification algorithm effectively suppresses the growth of computational effort with the increase of the measured DOFs n, which provides a fast estimation of the modal parameters.

4.2.1 Unconstrained parameterisation

First, consider the square norm of partial mode shapes $\{c_i\}_{i=1}^{n_g}$, it is subjected to the unit norm constraint from the global mode shape $\boldsymbol{\varphi}$, i.e,

$$\sum_{i=1}^{n_g} c_i = \sum_{i=1}^{n_g} \|\mathbf{u}_i\|^2 = \|\boldsymbol{\varphi}\|^2 = 1 \tag{44}$$

Optimising $\{c_i\}$ directly with the constraints through Lagrangian involves solving nonlinear equations. To see this, applying a Lagrange multiplier q that enforces the constraint in Eq.(44), the resulting NLLF is given by

$$J = \sum_{i=1}^{n_g} \left[(n_i - 1) N_f \ln S_{ei} + \sum_k \ln(SD_k c_i + S_{ei}) + S_{ei}^{-1} \left(d_i - \overline{\mathbf{u}}_i^T \mathbf{A}_i \overline{\mathbf{u}}_i \right) \right] + q \left(\sum_{i=1}^{n_g} c_i - 1 \right) \tag{45}$$

The gradient of J with respect to c_i can be expressed as

$$\frac{dJ}{dc_i} = \sum_k \left(c_i + \frac{S_{ei}}{SD_k} \right)^{-1} - S_{ei}^{-1} \overline{\mathbf{u}}_i^T \frac{d\mathbf{A}_i}{dc_i} \overline{\mathbf{u}}_i + q \tag{46}$$

where

$$\frac{d\mathbf{A}_i}{dc_i} = \sum_k \frac{S_{ei}}{SD_k} c_i^{-2} \left(1 + S_{ei} / SD_k c_i \right)^{-2} \mathbf{D}_{ik} \tag{47}$$

The MPV of $\{c_i\}$ should be obtained by solving $dJ / dc_i = 0$ using Eq.(46). Since dJ / dc depends on c_i in a nonlinear manner, it is hard to express the MPV of c_i in terms of the remaining parameters explicitly. In view of this, a parameterisation scheme is adopted that transfer the scaling of the modal force PSD to $\{c_i\}$ such that the resulting parameters are unconstrained. Specifically, let

$$S_i = S c_i \qquad\qquad i = 1, \ldots, n_g \tag{48}$$

The NLLF now can be expressed as

$$L_i = (n_i - 1) N_f \ln S_{ei} + \sum_k \ln(S_i D_k + S_{ei}) + S_{ei}^{-1} \left(d_i - \overline{\mathbf{u}}_i^T \mathbf{A}_i \overline{\mathbf{u}}_i \right) \tag{49}$$

where

$$\mathbf{A}_i = \sum_k \left(1 + S_{ei} / S_i D_k\right)^{-1} \mathbf{D}_{ik} \tag{50}$$

4.2.2 Most probable partial mode shapes

To obtain the MPV of normalised partial mode shapes $\{\overline{\mathbf{u}}_i\}$, the term $S_{ei}^{-1}\left(d_i - \overline{\mathbf{u}}_i^T \mathbf{A}_i \overline{\mathbf{u}}_i\right)$ in the NLLF needs to be optimised with the unit norm constraints, i.e.,

$$\left\|\overline{\mathbf{u}}_i\right\| = 1 \qquad\qquad i = 1,..., n_g \tag{51}$$

Note that the term is a quadratic form with respect to $\overline{\mathbf{u}}_i$, this can be done by applying the constraints into Eq.(49) using Lagrange multiplier. Specifically,

$$J_i = \left(n_i - 1\right) N_f \ln S_{ei} + \sum_k \ln\left(S_i D_k + S_{ei}\right) + S_{ei}^{-1}\left(d_i - \overline{\mathbf{u}}_i^T \mathbf{A}_i \overline{\mathbf{u}}_i\right) + q_i\left(\overline{\mathbf{u}}_i^T \overline{\mathbf{u}}_i - 1\right) \tag{52}$$

where q_i is the Lagrange multiplier that enforces the unit norm constraints of $\overline{\mathbf{u}}_i$. Setting the gradient of the function J_i with respect to $\overline{\mathbf{u}}_i$ equal to zero gives

$$\mathbf{A}_i \overline{\mathbf{u}}_i = q_i \overline{\mathbf{u}}_i \tag{53}$$

This is a standard eigenvalue problem. To minimise the NLLF, it follows that the MPV of $\overline{\mathbf{u}}_i$ is the eigenvector of $\mathbf{A}_i$ with the largest eigenvalue.

4.2.3 Iterative procedure

Based on the analysis in the previous section, the MPV of the partial mode shapes $\{\overline{\mathbf{u}}_i\}$ can be obtained analytically in terms of the remaining parameters and vice-versa. This leads to an iterative procedure to be proposed. Since the partial mode shapes can be obtained by solving an eigenvalue problem, the computational effort of this iterative procedure is insensitive to the measured DOFs n. The parameter set $\boldsymbol{\theta}$

to be optimised now includes $f,\zeta,\{S_i\},\{S_{ei}\}$ and $\{\overline{\mathbf{u}}_i\}$. Note that f and ζ are common to all L_i. They are the only parameters that connect the NLLF of different groups and need to be optimised using L in Eq.(35). The MPV of S_i and S_{ei} can be determined within each synchronous group by minimizing L_i only. The MPV of $\overline{\mathbf{u}}_i$ can be obtained with respect to other parameters by calculating the eigenvector of $\mathbf{A}_i$ with the largest eigenvalue for each asynchronous group i. After obtaining the MPV of S_i, the MPV of S and $\{c_i\}$ can be recovered. Specifically,

$$\hat{S} = \sum_{i=1}^{n_g} \hat{S}_i \tag{54}$$

and

$$\hat{c}_i = \frac{\hat{S}_i}{\hat{S}} \tag{55}$$

For $i = 1,...,n_g$. Here, a hat '^' denotes MPV.

The MPV of global mode shape can be recovered based on the MPV of $\{c_i\}$ and $\{\overline{\mathbf{u}}_i\}$ as

$$\hat{\boldsymbol{\varphi}} = \begin{bmatrix} s_1\sqrt{\hat{c}_1}\hat{\overline{\mathbf{u}}}_1 \\ \vdots \\ s_i\sqrt{\hat{c}_i}\hat{\overline{\mathbf{u}}}_i \\ \vdots \\ s_{n_g}\sqrt{\hat{c}_{n_g}}\hat{\overline{\mathbf{u}}}_{n_g} \end{bmatrix} \tag{56}$$

Here, $s_i = \pm 1$ is the relative direction between different partial mode shapes. Due to the zero coherence assumption, the local modes shapes $\{\overline{\mathbf{u}}_i\}$ are optimised within each synchronous group and the relative direction among these partial mode shapes

are not identified. That is, $+\overline{\mathbf{u}}_i$ and $-\overline{\mathbf{u}}_i$ give the same value in the NLLF. In practice, the relative direction $\{s_i\}$ can be empirically determined, e.g., spatial continuity of mode shapes. Of course, for complicated modes (e.g., modes with high natural frequencies) this may not be easy. This is one fundamental limitation of asynchronous data with the zero coherence assumption.

4.2.4 High signal-to-noise asymptotics

In this section, the asymptotic behaviour of the MPV of some modal parameters is investigated under high signal-to-noise ratio (SNR) conditions. It provides a rough estimation of the modal parameters that can be used as initial guesses for the proposed iterative procedure. High SNR refers to the condition when the PSD of modal responses is much larger than that of the prediction error. Specifically,

$$\gamma_{ki} = S_i D_k / S_{ei} = S D_k c_i / S_{ei} >> 1 \qquad i = 1,..., n_g \tag{57}$$

This is the standard SNR scaled by $c_i = \|\mathbf{u}_i\|^2$. Under this condition,

$$\left[1 + S_{ei} / S_i D_k\right]^{-1} = \left[1 + \gamma_{ki}^{-1}\right]^{-1} \sim 1 - \gamma_{ki}^{-1} \sim 1 \tag{58}$$

Here $\sim$ denotes 'asymptotically equivalent to'. The zeroth order approximation of $\mathbf{A}_i$ in Eq.(50) now can be given by

$$\mathbf{A}_i \sim \sum_{k=1}^{N_f} \mathcal{F}_{ik} \mathcal{F}_{ik}^{*} = \mathbf{A}_{0i} \tag{59}$$

which can be obtained directly based on the measured FFT data. In this context, the high SNR asymptotic MPV of the partial mode shapes $\{\overline{\mathbf{u}}_i\}$ can be determined as the eigenvector of $\mathbf{A}_{0i}$ with the largest eigenvalue (scaled to unit norm).

Now consider the first order approximation of $\mathbf{A}_i$:

$$\mathbf{A}_i \sim \sum_{k=1}^{N_f} \left[1 - S_{ei} / S_i D_k\right] \Phi_{ik} \Phi_{ik}^{*} = \mathbf{A}_{0i} - S_{ei} S_i^{-1} \sum_{k=1}^{N_f} D_k^{-1} \mathbf{D}_{ik} \tag{60}$$

Substituting Eq.(60) to the NLLF in Eq.(49) gives:

$$\begin{aligned} L_i = & \sum_{k=1}^{N_f} \ln D_k + (n_i - 1) N_f \left\{ \ln S_{ei} + S_{ei}^{-1} \left[\left(d_i - \overline{\mathbf{u}}_i^T \mathbf{A}_{0i} \overline{\mathbf{u}}_i \right) / (n_i - 1) N_f \right] \right\} \\ & + N_f \left\{ \ln S_i + (S_i)^{-1} \left[N_f^{-1} \sum_{k=1}^{N_f} \overline{\mathbf{u}}_i^T D_k^{-1} \mathbf{D}_{ik} \overline{\mathbf{u}}_i \right] \right\} \end{aligned} \tag{61}$$

It can be seen that S_i and S_{ei} are of the form $\ln x + a / x$ in the first and second braces of the resulting NLLF L_i. This form has a unique minimum of $1 + \ln a$ at $x = a$, which yields the high SNR asymptotic MPV of S_i and S_{ei} as

$$\hat{S}_{ei} \sim \left(d - d_i'\right) / \left(n_i - 1\right) N_f \tag{62}$$

and

$$\hat{S}_i \sim N_f^{-1} \sum_{k=1}^{N_f} \overline{\mathbf{u}}_i^T D_k^{-1} \mathbf{D}_{ik} \overline{\mathbf{u}}_i \tag{63}$$

Here $d_i' = \overline{\mathbf{u}}_i^T \mathbf{A}_{0i} \overline{\mathbf{u}}_i$, which is the maximum eigenvalue of $\mathbf{A}_{0i}$.

4.2.5 Summary of procedure

Based on the previous analysis, the procedure for determining the MPV of modal parameters can be summarised as follow. When updating certain parameters, the remaining ones are kept at their current value during iteration.

Step I. Initial Guess

1) Calculate the FFT of the measured data and plot the singular value spectrum.
2) Select the frequency band for the mode of interest.

3) Select the initial guess of f from the singular value spectrum and set the initial guess of ζ as 1%.

4) Calculate the initial guess of $\{\bar{\mathbf{u}}_i\}$ as the eigenvector with the largest eigenvalue of $\mathbf{A}_{0i}$ in Eq.(59).

5) Calculate the initial guess of $\{S_i, S_{ei}\}$ using Eq.(63) and Eq.(62) respectively.

Step II. Iteration Phase

6) Update $\{f, \zeta\}$ by minimising L in Eq.(35).

7) Update $\{S_i, S_{ei}\}$ by minimising L_i in Eq.(49).

8) Update $\{\bar{\mathbf{u}}_i\}$ as the eigenvector of $\mathbf{A}_i$ in Eq.(50) with the largest eigenvalue.

Repeat Steps 6) to 8) until convergence.

Step III. MPV of S and $\boldsymbol{\varphi}$

9) Calculate the MPV of S and $\{c_i\}$ based on the MPV of S_i using Eq.(54) and Eq.(55).

10) Calculate the MPV of $\boldsymbol{\varphi}$ based on the MPV of $\{c_i\}$ and $\{\bar{\mathbf{u}}_i\}$ using Eq.(56).

4.3 Posterior uncertainty

In a Bayesian context, the identification uncertainty of modal parameters can be quantified in terms of the posterior (i.e., given data) covariance matrix. For modal identification problems which are globally identifiable, the posterior covariance matrix is approximated by the inverse of Hessian of the NLLF. The Hessian matrix of the NLLF is a symmetric matrix containing the second derivatives with respect to the modal parameters $\boldsymbol{\theta} = \left\{f, \zeta, S, \{S_{ei}\}_{i=1}^{n_g}, \boldsymbol{\varphi}\right\}$. The analytical expressions of these

derivatives will be derived in this section, allowing an accurate and efficient determination of the identification uncertainty of modal parameters without resorting to finite difference methods.

Recall the NLLF in Eq.(40), it depends on the global mode shape $\boldsymbol{\varphi}$ through c_i and $\overline{\mathbf{u}}_i$. To investigate the identification uncertainty of $\boldsymbol{\varphi}$, it is better to express the NLLF explicitly in terms of $\boldsymbol{\varphi}$ to facilitate analysis. Define a selection matrix $\mathbf{L}_i \in R^{n_i \times n}$ so that the partial mode shape $\mathbf{u}_i$ can be expressed as $\mathbf{L}_i\boldsymbol{\varphi}$. The (j,k)-entry of $\mathbf{L}_i$ is equal to 1 if DOF k is measured by the j th channel in the i th synchronous group, and zero otherwise. Then c_i and $\overline{\mathbf{u}}_i$ can be expressed in terms of $\boldsymbol{\varphi}$:

$$c_i = \left\|\mathbf{L}_i\boldsymbol{\varphi}\right\|^2 = \boldsymbol{\varphi}^T\mathbf{L}_i^T\mathbf{L}_i\boldsymbol{\varphi} \tag{64}$$

$$\overline{\mathbf{u}}_i = \frac{\mathbf{L}_i\boldsymbol{\varphi}}{\left\|\mathbf{L}_i\boldsymbol{\varphi}\right\|} = \left(\boldsymbol{\varphi}^T\mathbf{L}_i^T\mathbf{L}_i\boldsymbol{\varphi}\right)^{-1/2}\mathbf{L}_i\boldsymbol{\varphi} \tag{65}$$

The unit norm constraint of the global mode shape (i.e., $\left\|\boldsymbol{\varphi}\right\|^2 = \boldsymbol{\varphi}^T\boldsymbol{\varphi} = 1$) needs to be accounted when deriving the derivatives of the NLLF. To preserve this constraint automatically, $\boldsymbol{\varphi}$ in the NLLF is replaced by its normalised counterpart, i.e.,

$$\overline{\boldsymbol{\varphi}} = \left\|\boldsymbol{\varphi}\right\|^{-1}\boldsymbol{\varphi} \tag{66}$$

Substituting Eq. (64) and (65) into the NLLF in Eq.(40) and replacing $\boldsymbol{\varphi}$ by $\overline{\boldsymbol{\varphi}}$ in Eq.(66), the NLLF is now given by

$$L = \sum_{i=1}^{n_g}(n_i - 1)N_f \ln S_{ei} + \sum_{i=1}^{n_g}\sum_k \ln\left(SD_k\frac{\left\|\mathbf{L}_i\boldsymbol{\varphi}\right\|^2}{\boldsymbol{\varphi}^T\boldsymbol{\varphi}} + S_{ei}\right) + \sum_{i=1}^{n_g} S_{ei}^{-1}d_i - \frac{\boldsymbol{\varphi}^T\mathbf{A}'\boldsymbol{\varphi}}{\boldsymbol{\varphi}^T\boldsymbol{\varphi}} \tag{67}$$

where

$$\mathbf{A}' = \sum_{i=1}^{n_g} S_{ei}^{-1} \sum_k \left(\frac{\|\mathbf{L}_i \boldsymbol{\varphi}\|^2}{\boldsymbol{\varphi}^T \boldsymbol{\varphi}} + \frac{S_{ei}}{SD_k} \right)^{-1} \mathbf{L}_i^T \mathbf{D}_{ik} \mathbf{L}_i \tag{68}$$

Since the resulting NLLF does not depend on the scaling of the global mode shape $\boldsymbol{\varphi}$, its Hessian at the MPV of modal parameters is singular along the direction of $\boldsymbol{\varphi}$ [78]. This singularity is immaterial to posterior uncertainty because mode shape uncertainty is by definition orthogonal to such direction. The posterior covariance matrix can be obtained by calculating the 'pseudo-inverse' of the Hessian. This can be done through the eigenvector representation of the Hessian matrix ignoring its singular component (i.e., zero eigenvalue and the corresponding eigenvector). Let $\{\lambda_i\}_{i=1}^{n_\theta}$ and $\{\mathbf{w}_i \in R^{n_\theta}\}_{i=1}^{n_\theta}$ be the eigenvalues (in ascending order) and eigenvectors of the Hessian of the NLLF at MPV, respectively. Here, n_θ is the number of modal parameters. Then $\lambda_1 = 0$ (singularity due to norm constraint) and

$$\mathbf{H}_L = \sum_{i=2}^{n_\theta} \lambda_i \mathbf{w}_i \mathbf{w}_i^T \tag{69}$$

The posterior covariance matrix $\mathbf{C}$ is given by the inverse of $\mathbf{H}_L$, which has the same eigenvectors but reciprocal of eigenvalues:

$$\mathbf{C} = \sum_{i=2}^{n_\theta} \lambda_i^{-1} \mathbf{w}_i \mathbf{w}_i^T \tag{70}$$

4.3.1 Derivatives of the NLLF

The analytical expressions for the derivatives of the NLLF are obtained by direct differentiation of Eq.(67). The NLLF is first rewritten with respect to a_{ik}, b_{ik} and p_{ik} to facilitate analysis:

$$L = \sum_{i=1}^{n_g} (n_i - 1) N_f \ln S_{ei} + \sum_{i=1}^{n_g} \sum_k \ln b_{ik} + \sum_{i=1}^{n_g} S_{ei}^{-1} \left(d_{ik} - \sum_k a_{ik} p_{ik} \right) \tag{71}$$

where

$$a_{ik} = \left(\frac{\left\| \mathbf{L}_i \boldsymbol{\varphi} \right\|^2}{\boldsymbol{\varphi}^T \boldsymbol{\varphi}} + \frac{S_{ei}}{SD_k} \right)^{-1} \tag{72}$$

$$b_{ik} = SD_k \frac{\left\| \mathbf{L}_i \boldsymbol{\varphi} \right\|^2}{\boldsymbol{\varphi}^T \boldsymbol{\varphi}} + S_{ei} \tag{73}$$

$$p_{ik} = \frac{\boldsymbol{\varphi}^T \mathbf{L}_i^T \mathbf{D}_{ik} \mathbf{L}_i \boldsymbol{\varphi}}{\boldsymbol{\varphi}^T \boldsymbol{\varphi}} \tag{74}$$

The derivatives of a_{ik}, b_{ik} and p_{ik} appear frequently in the derivatives of the NLLF, whose expressions will be presented later. In the following, a superscripted symbol denotes the derivative with respect to that variable.

Auto-derivatives

$$L^{(ff)} = \sum_{i=1}^{n_g} \sum_k \left(\ln b_{ik} \right)^{(ff)} - \sum_{i=1}^{n_g} S_{ei}^{-1} \left(\sum_k a_{ik}^{(ff)} p_{ik} \right) \tag{75}$$

(similar expression for $L^{(\zeta\zeta)}$ and $L^{(SS)}$)

$$\begin{aligned} L^{(S_{ei}S_{ei})} = & -S_{ei}^{-2} N_f (n_i - 1) + \sum_k \left(\ln b_{ik} \right)^{(S_{ei}S_{ei})} - S_{ei}^{-1} \sum_k a_{ik}^{(S_{ei}S_{ei})} p_{ik} \\ & + 2 S_{ei}^{-2} \sum_k a_{ik}^{(S_{ei})} p_{ik} + 2 S_{ei}^{-3} \left(d_{ik} - \sum_k a_{ik} p_{ik} \right) \end{aligned} \tag{76}$$

$$\begin{aligned} L^{(\varphi\varphi)} = & \sum_{i=1}^{n_g} \sum_k \left(\ln b_{ik} \right)^{(\varphi\varphi)} - \sum_{i=1}^{n_g} S_{ei}^{-1} \sum_k a_{ik}^{(\varphi\varphi)} p_{ik} - \sum_{i=1}^{n_g} S_{ei}^{-1} \sum_k \left(a_{ik}^{(\varphi)} \right)^T p_{ik}^{(\varphi)} \\ & - \sum_{i=1}^{n_g} S_{ei}^{-1} \sum_k \left(p_{ik}^{(\varphi)} \right)^T a_{ik}^{(\varphi)} - \sum_{i=1}^{n_g} S_{ei}^{-1} \sum_k a_{ik} p_{ik}^{(\varphi\varphi)} \end{aligned} \tag{77}$$

Cross derivatives

$$L^{(f\zeta)} = \sum_{i=1}^{n_g}\sum_{k}\left(\ln b_{ik}\right)^{(f\zeta)} - \sum_{i=1}^{n_g} S_{ei}^{-1}\left(\sum_{k} a_{ik}^{(f\zeta)} p_{ik}\right) \tag{78}$$

(similar expressions for $L^{(fS)}$ and $L^{(\zeta S)}$)

$$L^{(fS_{ei})} = \sum_{k}\left(\ln b_{ik}\right)^{(fS_{ei})} - S_{ei}^{-1}\sum_{k} a_{ik}^{(fS_{ei})} p_{ik} + S_{ei}^{-2}\sum_{k} a_{ik}^{(f)} p_{ik} \tag{79}$$

(similar expressions for $L^{(\zeta S_{ei})}$ and $L^{(SS_{ei})}$)

$$L^{(f\boldsymbol{\varphi})} = \sum_{i=1}^{n_g}\sum_{k}\left(\ln b_{ik}\right)^{(f\boldsymbol{\varphi})} - \sum_{i=1}^{n_g} S_{ei}^{-1}\sum_{k} a_{ik}^{(f\boldsymbol{\varphi})} p_{ik} - \sum_{i=1}^{n_g} S_{ei}^{-1}\sum_{k} a_{ik}^{(f)} p_{ik}^{(\boldsymbol{\varphi})} \tag{80}$$

(similar expressions for $L^{(\zeta\boldsymbol{\varphi})}$ and $L^{(S\boldsymbol{\varphi})}$)

$$\begin{aligned} L^{(S_{ei}\boldsymbol{\varphi})} = {} & \sum_{k}\left(\ln b_{ik}\right)^{(S_{ei}\boldsymbol{\varphi})} - S_{ei}^{-1}\left(\sum_{k} a_{ik}^{(S_{ei}\boldsymbol{\varphi})} p_{ik} + \sum_{k} a_{ik}^{(S_{ei})} p_{ik}^{(\boldsymbol{\varphi})}\right) \\ & + S_{ei}^{-2}\left(\sum_{k} a_{ik}^{(\boldsymbol{\varphi})} p_{ik} + \sum_{k} a_{ik} p_{ik}^{(\boldsymbol{\varphi})}\right) \end{aligned} \tag{81}$$

Derivatives of a_{ik}

Note that a_{ik} is in the form of x^{-1}. It is easier to evaluate the derivatives of its reciprocal a_{ik}^{-1}. For any two parameters x_1 and x_2 in $\{f, \zeta, S, \{S_{ei}\}, \boldsymbol{\varphi}\}$,

$$a_{ik}^{(x_1)} = -a_{ik}^2\left(a_{ik}^{-1}\right)^{(x_1)} \tag{82}$$

and

$$a_{ik}^{(x_1x_2)} = 2a_{ik}^3\left(a_{ik}^{-1}\right)^{(x_1)}\left(a_{ik}^{-1}\right)^{(x_2)} - a_{ik}^2\left(a_{ik}^{-1}\right)^{(x_1x_2)} \tag{83}$$

Specifically, the second derivative of a_{ik} with respect to $\boldsymbol{\varphi}$ is given by

$$a_{ik}^{(\boldsymbol{\varphi}\boldsymbol{\varphi})} = 2a_{ik}^3 \left[\left(a_{ik}^{-1}\right)^{(\boldsymbol{\varphi})}\right]^T \left(a_{ik}^{-1}\right)^{(\boldsymbol{\varphi})} - a_{ik}^2 \left(a_{ik}^{-1}\right)^{(\boldsymbol{\varphi}\boldsymbol{\varphi})} \tag{84}$$

The first and second derivatives of a_{ik}^{-1} are given in *Table 4.3-1* and *Table 4.3-2*, respectively. The expressions involve the derivatives of D_k, which are presented later.

Table 4.3-1 First derivatives of a_{ik}^{-1}

$x=$	f,ζ	S	S_{ei}	$\boldsymbol{\varphi}$
$\left(a_{ik}^{-1}\right)^{(x)}$	$\frac{S_{ei}}{S}\left(D_k^{-1}\right)^{(x)}$	$-\frac{S_{ei}}{S^2 D_k}$	$\frac{1}{SD_k}$	$\frac{2\boldsymbol{\varphi}^T \mathbf{L}_i^T \mathbf{L}_i}{\boldsymbol{\varphi}^T\boldsymbol{\varphi}} - \frac{2\boldsymbol{\varphi}^T \left\|\mathbf{L}_i\boldsymbol{\varphi}\right\|^2}{\left(\boldsymbol{\varphi}^T\boldsymbol{\varphi}\right)^2}$

Table 4.3-2 Second derivatives of a_{ik}^{-1}

$\left(a_{ik}^{-1}\right)^{(xy)}$ $y=$	f,ζ	S	S_{ei}	$\boldsymbol{\varphi}$
$x=$				
f,ζ	$\frac{S_{ei}}{S}\left(D_k^{-1}\right)^{(xy)}$	$-\frac{S_{ei}}{S^2}\left(D_k^{-1}\right)^{(x)}$	$\frac{1}{S}\left(D_k^{-1}\right)^{(x)}$	$\mathbf{0}$
S		$\frac{2S_{ei}}{S^3 D_k}$	$-\frac{1}{S^2 D_k}$	$\mathbf{0}$
S_{ei}	sym.		0	$\mathbf{0}$
$\boldsymbol{\varphi}$				See note

Note: $\left(a_{ik}^{-1}\right)^{(\boldsymbol{\varphi}\boldsymbol{\varphi})} = \frac{2\mathbf{L}_i^T\mathbf{L}_i}{\boldsymbol{\varphi}^T\boldsymbol{\varphi}} - \frac{4\boldsymbol{\varphi}\boldsymbol{\varphi}^T\mathbf{L}_i^T\mathbf{L}_i}{\left(\boldsymbol{\varphi}^T\boldsymbol{\varphi}\right)^2} + \frac{8\boldsymbol{\varphi}\boldsymbol{\varphi}^T\left\|\mathbf{L}_i\boldsymbol{\varphi}\right\|^2}{\left(\boldsymbol{\varphi}^T\boldsymbol{\varphi}\right)^3} - \frac{4\mathbf{L}_i^T\mathbf{L}_i\boldsymbol{\varphi}\boldsymbol{\varphi}^T}{\left(\boldsymbol{\varphi}^T\boldsymbol{\varphi}\right)^2} - \frac{2\left\|\mathbf{L}_i\boldsymbol{\varphi}\right\|^2}{\left(\boldsymbol{\varphi}^T\boldsymbol{\varphi}\right)^2}\mathbf{I}_n$.

Derivatives of $\ln b_{ik}$

The derivatives of $\ln b_{ik}$ can be expressed through those of b_{ik}, which is easier to derive. For any two parameters x_1 and x_2 in $\{f,\zeta,S,\{S_{ei}\},\boldsymbol{\varphi}\}$,

$$\left(\ln b_{ik}\right)^{(x_1)} = \frac{1}{b_{ik}} b_{ik}^{(x_1)} \tag{85}$$

$$\left(\ln b_{ik}\right)^{(x_1 x_2)} = -\left(\frac{1}{b_{ik}}\right)^2 b_{ik}^{(x_1)} b_{ik}^{(x_2)} + \frac{1}{b_{ik}} b_{ik}^{(x_1 x_2)} \tag{86}$$

Specifically, the second derivative of $\ln b_{ik}$ with respect to $\boldsymbol{\varphi}$ is given by

$$\left(\ln b_{ik}\right)^{(\boldsymbol{\varphi}\boldsymbol{\varphi})} = -\left(\frac{1}{b_{ik}}\right)^2 \left(b_{ik}^{(\boldsymbol{\varphi})}\right)^T b_{ik}^{(\boldsymbol{\varphi})} + \frac{1}{b_{ik}} b_{ik}^{(\boldsymbol{\varphi}\boldsymbol{\varphi})} \tag{87}$$

The first and second derivatives of b_{ik} are given in *Table 4.3-3* and *Table 4.3-4*, respectively. The expressions involve the derivatives of D_k, which are presented later.

Table 4.3-3 First derivatives of b_{ik}

$x=$	f,ζ	S	S_{ei}	$\boldsymbol{\varphi}$
$b_{ik}^{(x)}$	$D_k^{(x)} \dfrac{\left\|\mathbf{L}_i\boldsymbol{\varphi}\right\|^2}{\boldsymbol{\varphi}^T\boldsymbol{\varphi}}$	$D_k \dfrac{\left\|\mathbf{L}_i\boldsymbol{\varphi}\right\|^2}{\boldsymbol{\varphi}^T\boldsymbol{\varphi}}$	1	$2SD_k\left(\dfrac{\boldsymbol{\varphi}^T\mathbf{L}_i^T\mathbf{L}_i}{\boldsymbol{\varphi}^T\boldsymbol{\varphi}} - \dfrac{\boldsymbol{\varphi}^T\left\|\mathbf{L}_i\boldsymbol{\varphi}\right\|^2}{\left(\boldsymbol{\varphi}^T\boldsymbol{\varphi}\right)^2}\right)$

Table 4.3-4 Second derivatives of b_{ik}

$b_{ik}^{(xy)}$	$y=$	f,ζ	S	S_{ei}	$\boldsymbol{\varphi}$
$x=$					
f,ζ		$SD_k^{(xy)} \dfrac{\left\|\mathbf{L}_i\boldsymbol{\varphi}\right\|^2}{\boldsymbol{\varphi}^T\boldsymbol{\varphi}}$	$D_k^{(x)} \dfrac{\left\|\mathbf{L}_i\boldsymbol{\varphi}\right\|^2}{\boldsymbol{\varphi}^T\boldsymbol{\varphi}}$	0	$2SD_k^{(x)}\left(\dfrac{\boldsymbol{\varphi}^T\mathbf{L}_i^T\mathbf{L}_i}{\boldsymbol{\varphi}^T\boldsymbol{\varphi}} - \dfrac{\boldsymbol{\varphi}^T\left\|\mathbf{L}_i\boldsymbol{\varphi}\right\|^2}{\left(\boldsymbol{\varphi}^T\boldsymbol{\varphi}\right)^2}\right)$
S			0	0	$2D_k\left(\dfrac{\boldsymbol{\varphi}^T\mathbf{L}_i^T\mathbf{L}_i}{\boldsymbol{\varphi}^T\boldsymbol{\varphi}} - \dfrac{\boldsymbol{\varphi}^T\left\|\mathbf{L}_i\boldsymbol{\varphi}\right\|^2}{\left(\boldsymbol{\varphi}^T\boldsymbol{\varphi}\right)^2}\right)$
S_{ei}		sym.		0	$\mathbf{0}$

$\boldsymbol{\varphi}$	See note

Note: $b_{ik}^{(\varphi\varphi)} = SD_k\left(\frac{2\mathbf{L}_i^T\mathbf{L}_i}{\boldsymbol{\varphi}^T\boldsymbol{\varphi}} - \frac{4\boldsymbol{\varphi}\boldsymbol{\varphi}^T\mathbf{L}_i^T\mathbf{L}_i}{\left(\boldsymbol{\varphi}^T\boldsymbol{\varphi}\right)^2} + \frac{8\boldsymbol{\varphi}\boldsymbol{\varphi}^T\left\|\mathbf{L}_i\boldsymbol{\varphi}\right\|^2}{\left(\boldsymbol{\varphi}^T\boldsymbol{\varphi}\right)^3} - \frac{4\mathbf{L}_i^T\mathbf{L}_i\boldsymbol{\varphi}\boldsymbol{\varphi}^T}{\left(\boldsymbol{\varphi}^T\boldsymbol{\varphi}\right)^2} - \frac{2\left\|\mathbf{L}_i\boldsymbol{\varphi}\right\|^2}{\left(\boldsymbol{\varphi}^T\boldsymbol{\varphi}\right)^2}\mathbf{I}_n\right)$.

Derivatives of p_{ik}

The first and second derivatives of p_{ik} with respect to the global mode shape $\boldsymbol{\varphi}$ are given by

$$p_{ik}^{(\varphi)} = \frac{2\boldsymbol{\varphi}^T\mathbf{L}_i^T\mathbf{D}_{ik}\mathbf{L}_i}{\boldsymbol{\varphi}^T\boldsymbol{\varphi}} - \frac{2\boldsymbol{\varphi}^T\mathbf{L}_i^T\mathbf{D}_{ik}\mathbf{L}_i\boldsymbol{\varphi}\boldsymbol{\varphi}^T}{\left(\boldsymbol{\varphi}^T\boldsymbol{\varphi}\right)^2} \tag{88}$$

$$\begin{aligned} p_{ik}^{(\varphi\varphi)} = {} & \frac{2\mathbf{L}_i^T\mathbf{D}_{ik}\mathbf{L}_i}{\boldsymbol{\varphi}^T\boldsymbol{\varphi}} - \frac{4\boldsymbol{\varphi}\boldsymbol{\varphi}^T\mathbf{L}_i^T\mathbf{D}_{ik}\mathbf{L}_i}{\left(\boldsymbol{\varphi}^T\boldsymbol{\varphi}\right)^2} + \frac{8\boldsymbol{\varphi}\boldsymbol{\varphi}^T\left(\boldsymbol{\varphi}^T\mathbf{L}_i^T\mathbf{D}_{ik}\mathbf{L}_i\boldsymbol{\varphi}\right)}{\left(\boldsymbol{\varphi}^T\boldsymbol{\varphi}\right)^3} \\ & - \frac{4\mathbf{L}_i^T\mathbf{D}_{ik}\mathbf{L}_i\boldsymbol{\varphi}\boldsymbol{\varphi}^T}{\left(\boldsymbol{\varphi}^T\boldsymbol{\varphi}\right)^2} - \frac{2\boldsymbol{\varphi}^T\mathbf{L}_i^T\mathbf{D}_{ik}\mathbf{L}_i\boldsymbol{\varphi}\mathbf{I}_n}{\left(\boldsymbol{\varphi}^T\boldsymbol{\varphi}\right)^2} \end{aligned} \tag{89}$$

Derivatives of D_k

The derivatives of a_{ik}, b_{ik} involve the first and second derivatives of D_k, whose expressions are presented here. It is easier to express its derivatives with respect to the derivatives of its reciprocal D_k^{-1}. In general, for any two variables x_1 and x_2:

$$D_k^{(x_1)} = -D_k^{\,2}\left(D_k^{-1}\right)^{(x_1)} \tag{90}$$

$$D_k^{(x_1x_2)} = 2D_k^{\,3}\left(D_k^{-1}\right)^{(x_1)}\left(D_k^{-1}\right)^{(x_2)} - D_k^2\left(D_k^{-1}\right)^{(x_1x_2)} \tag{91}$$

The derivatives of D_k^{-1} with respect to f and ζ are given by

$$\left(D_k^{-1}\right)^{(f)} = 4f_k^{-1}\left[\beta_k^3 - \beta_k\left(1-2\zeta^2\right)\right] \tag{92}$$

$$\left(D_k^{-1}\right)^{(\zeta)} = 8\zeta\beta_k^2 \tag{93}$$

$$\left(D_k^{-1}\right)^{(ff)} = 4f_k^{-2}\left[3\beta_k^2 - 1 + 2\zeta^2\right] \tag{94}$$

$$\left(D_k^{-1}\right)^{(\zeta\zeta)} = 8\beta_k^2 \tag{95}$$

$$\left(D_k^{-1}\right)^{(f\zeta)} = 16f_k^{-1}\zeta\beta_k \tag{96}$$

4.3.2 Dimensionless scaling

The modal parameters have different units and hence different order of magnitude in the NLLF. Different entries in the Hessian matrix will have large disparities in the order of magnitude. The computation of the inverse of the Hessian is ill-conditioned. To address this problem, the entries of the Hessian matrix can be normalised by the corresponding MPV of modal parameters before calculating the inverse. Let $\boldsymbol{\theta} = [f;\zeta;S;S_{e1};...;S_{en_g};\boldsymbol{\varphi}]$ denote the vector of modal parameters and $\hat{\boldsymbol{\theta}} = [\hat{f};\hat{\zeta};\hat{S};\hat{S}_{e1};...;\hat{S}_{en_g}]$ denote the vector of MPVs except for the global mode shape. Define the dimensionless vector

$$\mathbf{a} = \mathbf{T}\boldsymbol{\theta} \tag{97}$$

where

$$\mathbf{T} = \begin{bmatrix} diag\left\{\hat{\boldsymbol{\theta}}\right\}^{-1} & \\ & \mathbf{I}_n \end{bmatrix} \tag{98}$$

Except for the mode shape (which already have unit norm), the entries of $\mathbf{a}$ are the ratio of the modal parameters to the corresponding MPVs, which are dimensionless. The dimensionless form of the Hessian matrix then can be expressed with respect to $\mathbf{a}$ at MPV as:

$$\mathbf{H}'_L = \mathbf{T}^{-T}\mathbf{H}_L\mathbf{T}^{-1} \tag{99}$$

The pseudo-inverse of $\mathbf{H}'_L$ is also dimensionless and its diagonal entires now give directly the square of coefficient of variation (c.o.v.) of the corresponding modal parameters.

4.3.3 Summary of procedure

Based on the previous analysis, the procedure for determining the identification uncertainty of modal parameters can be summarised as follow.

1) Calculate the entries of the Hessian matrix based on the derivatives of the NLLF in Section 4.3.1 with the help of the derivatives of a_{ik} , b_{ik} and p_{ik} .
2) Assemble the Hessian matrix $\mathbf{H}_L$ and calculate its dimensionless form $\mathbf{H}'_L$ using Eq.(99).
3) Perform eigenvector decomposition of $\mathbf{H}'_L$ and calculate the posterior covariance matrix $\mathbf{C}$ (pseudo-inverse of $\mathbf{H}'_L$) using Eq.(70).
4) The posterior c.o.v. of modal parameters can be directly obtained from the square root of the corresponding diagonal term of the posterior covariance matrix.
5) The posterior c.o.v. of the overall mode shape $\boldsymbol{\varphi}$ can be expressed as the square root sum of the eigenvalues of its covariance matrix, equal to the corresponding partition in the full posterior covariance matrix [117].

Chapter 5: Bayesian Method with General Coherence Assumption

A Bayesian modal identification method with zero coherence assumption has been proposed in the last Chapter. It provides a quick estimation of modal parameters using asynchronous ambient data. In this chapter, a Bayesian modal identification method with general coherence assumption is proposed, which strictly obeys the asynchronous data model. As mentioned previously, the theoretical PSD matrix for asynchronous ambient data depends on the coherence values among different synchronous groups in a non-trivial manner. The optimisation procedure based on the original formulation turns out to be computationally non-trivial and ill-conditioned. Efficient strategies for numerical optimisation are proposed, which significantly suppress the dimension of matrix computation involved. An iterative scheme is then developed, which allows the MPV of modal parameters as well as coherence values to be determined efficiently. Although more computational effort is expected compared to the Bayesian method with zero coherence assumption, the method proposed in this chapter provides a more robust means to identify the modal parameters and quantify the asynchronous degree among different synchronous data groups from asynchronous ambient data without extra modelling error involved.

5.1 Computational difficulties and solving strategies

The MPV of modal parameters are determined by minimising the NLLF, which involves computation of the determinant and inverse of the theoretical PSD matrix $\mathbf{E}_k$ repeatedly with different trails of $\boldsymbol{\theta}$. The eigenvalue and eigenvector properties of the theoretical PSD matrix $\mathbf{E}_k$ based on the asynchronous data model with the general coherence assumption (see Eq.(26)) depend on the coherence values in a

non-trivial manner. It is difficult to express the determinant and inverse of $\mathbf{E}_k$ in analytically tractable forms. The computation of these two terms is also ill-conditioned. In the resonance frequency band of the mode, the modal response (first term in Eq.(19)) is normally much larger than the prediction error (second term in Eq.(19)). $\mathbf{E}_k$ is close to be singular with a rank of at most n_g. It is better to express $\mathbf{E}_k$ in better forms to address the foregoing computational difficulties and facilitate analysis.

First rewrite $\mathbf{E}_k$ in Eq.(19) as

$$\mathbf{E}_k = SD_k\mathbf{U}\mathbf{C}\mathbf{U}^T + S_e\mathbf{I}_n \tag{100}$$

where

$$\mathbf{C} = diag\left\{\left\|\mathbf{u}_i\right\|\right\}_{i=1}^{n_g}\boldsymbol{\chi}diag\left\{\left\|\mathbf{u}_i\right\|\right\}_{i=1}^{n_g} \tag{101}$$

The coherence matrix $\boldsymbol{\chi}$ is assumed to be constant (hence $\mathbf{C}$) within the selected frequency band, which is justified when the band is not wide (typical in real applications).

Define a condensed form $\mathbf{E}'_k \in C^{n_g}$ as

$$\mathbf{E}'_k = SD_k\mathbf{C} + S_e\mathbf{I}_{n_g} \tag{102}$$

Similar to the case of $\mathbf{E}_k$, the determinant and inverse of $\mathbf{E}'_k$ can be given by

$$\det \mathbf{E}'_k = \prod_{i=1}^{n_g} \left(SD_k \lambda_i + S_e \right) \tag{103}$$

$$\mathbf{E}'^{-1}_k = \sum_{i=1}^{n_g} \left(SD_k \lambda_i + S_e \right)^{-1} \mathbf{c}_i \mathbf{c}_i^* \tag{104}$$

The determinant and inverse of $\mathbf{E}_k$ now can be expressed in terms of $\mathbf{E}'_k$ as

$$\det \mathbf{E}_k = S_e^{n-n_g} \det \mathbf{E}'_k \tag{105}$$

$$\mathbf{E}_k^{-1} = \mathbf{U} \mathbf{E}'^{-1}_k \mathbf{U}^T + S_e^{-1} \left(\mathbf{I}_n - \mathbf{U} \mathbf{I}_{n_g} \mathbf{U}^T \right) \tag{106}$$

Substituting Eq.(105) and Eq.(106) into the NLLF in Eq.(6), it now can be written as

$$L(\boldsymbol{\theta}) = \left(n - n_g \right) N_f \ln S_e + \sum_k \ln \det \mathbf{E}'_k + S_e^{-1} \left(d - d' \right) + \sum_k \mathcal{F}_k'^* \mathbf{E}'^{-1}_k \mathcal{F}'_k \tag{107}$$

where

$$d = \mathcal{F}_k \mathcal{F}_k^* \tag{108}$$

$$d' = \mathcal{F}_k'^* \mathcal{F}'_k \tag{109}$$

$$\mathcal{F}'_k = \mathbf{U}^T \mathcal{F}_k \tag{110}$$

The dimension of the matrix computation involved in the resulting NLLF has now been suppressed to n_g (the number of synchronous data groups), which is smaller than n (the number of measured DOFs) in the initial NLLF. The condensed form $\mathbf{E}'_k$ has full rank so the computation of its inverse and determinant is well-defined. Based on this NLLF, the MPV of modal parameters are investigated and an iterative scheme will be proposed.

5.2 Most probable value of modal parameters

In this section, the MPV of modal parameters are investigated, which allows an iterative scheme to be proposed. First, consider the MPV of normalised mode shape matrix $\mathbf{U}$. It is subjected to unit norm constraints of the partial mode shape in each synchronous group as

$$\left\|\overline{\mathbf{u}}_i\right\| = 1 \qquad i = 1,...,n_g \tag{111}$$

The NLLF depends on $\mathbf{U}$ through the last two terms, which can be written as

$$\begin{aligned} L_Q &= S_e^{-1}\left(d - d'\right) + \sum_k \mathcal{F}_k'^{*}\mathbf{E}_k'^{-1}\mathcal{F}_k' \\ &= S_e^{-1}d - S_e^{-1}\sum_k \mathcal{F}_k^{*}\mathbf{U}\left(\mathbf{I}_{n_g} - S_e\mathbf{E}_k'^{-1}\right)\mathbf{U}^T\mathcal{F}_k \end{aligned} \tag{112}$$

The MPV of $\mathbf{U}$ should be obtained by minimising Eq.(112). It is better to swap the order of $\mathcal{F}_k$ and $\mathbf{U}$ so that the MPV of $\mathbf{U}$ can be obtained by solving eigenvalue problems. To see this, rewrite $\mathbf{U}^T\mathcal{F}_k$ as

$$\mathbf{U}^T\mathcal{F}_k = \mathbf{F}_k\mathbf{U}' \tag{113}$$

where

$$\mathbf{F}_k = \begin{bmatrix} \mathcal{F}_{1k}^T & & \\ & \ddots & \\ & & \mathcal{F}_{n_g k}^T \end{bmatrix} \tag{114}$$

$$\mathbf{U}' = \begin{bmatrix} \overline{\mathbf{u}}_1 \\ \vdots \\ \overline{\mathbf{u}}_{n_g} \end{bmatrix} \tag{115}$$

Here, $\mathcal{F}_{ik}$ ($i = 1,...,n_g$) is the FFT of the measured data corresponding to the ith synchronous data groups. The resulting L_Q then can be expressed as

$$L_Q = S_e^{-1} d - S_e^{-1} \mathbf{U}'^T \mathbf{A} \mathbf{U}' \tag{116}$$

where

$$\mathbf{A} = \sum_k \mathbf{F}_k^* \left(\mathbf{I}_{n_g} - S_e \mathbf{E}_k'^{-1} \right) \mathbf{F}_k \tag{117}$$

To apply the unit norm constraints in Eq.(111), it is better to express $\bar{\mathbf{u}}_i$ in terms of $\mathbf{U}'$ to facilitate analysis. Define a selection matrix $\mathbf{L}_i \in R^{n_i \times n}$ such that

$$\bar{\mathbf{u}}_i = \mathbf{L}_i \mathbf{U}' \tag{118}$$

where the (j,k)-entry of $\mathbf{L}_i$ is equal to 1 if DOF k is measured by the j th channel in the i th synchronous group, and zero otherwise. Applying the constraints in Eq.(111) through Lagrange multiplier, the resulting function is given by

$$J = S_e^{-1} d - S_e^{-1} \mathbf{U}'^T \mathbf{A} \mathbf{U}' + \sum_{i=1}^{n_g} q_i \left(\mathbf{U}'^T \mathbf{L}_i^T \mathbf{L}_i \mathbf{U}' - 1 \right) \tag{119}$$

where $\{q_i\}_{i=1}^{n_g}$ are the Lagrange multipliers that enforce the norm of $\bar{\mathbf{u}}_i \left(i = 1..., n_g \right)$ to be 1. The gradient of J with respect to $\mathbf{U}'$ is given by

$$\nabla_{\mathbf{U}'} J = -2 S_e^{-1} \mathbf{A} \mathbf{U}' + 2 \sum_{i=1}^{n_g} q_i \mathbf{L}_i^T \mathbf{L}_i \mathbf{U}' \tag{120}$$

Solving $\nabla_{\mathbf{U}'} J = \mathbf{0}$ gives the MPV of $\mathbf{U}'$, which can be expressed (after rearranging) as

$$S_e^{-1} \mathbf{A} \mathbf{U}' = \sum_{i=1}^{n_g} q_i \mathbf{L}_i^T \mathbf{L}_i \mathbf{U}' \tag{121}$$

It is not a standard eigenvalue problem and optimising $\mathbf{U}'$ using Eq.(121) involves solving nonlinear equations. Instead of updating $\mathbf{U}'$ directly, it is better to update its

partition $\overline{\mathbf{u}}_i$ in each synchronous group separately by assuming other $\overline{\mathbf{u}}_j$ ($i \neq j$) to be constant. Eq.(121) then can be written as:

$$\mathbf{A}_{ii}\overline{\mathbf{u}}_i + \sum_{j=1(j\neq i)}^{n_g} \mathbf{A}_{ij}\overline{\mathbf{u}}_j = q_i\overline{\mathbf{u}}_i \qquad i = 1,...,n_g \tag{122}$$

where $\mathbf{A}_{ij} \in C^{n_i \times n_j}$ is the corresponding (i, j) partition matrix of $\mathbf{A}$. It now becomes a 'constrained eigenvalue problem' [118] where the MPV of $\overline{\mathbf{u}}_i$ can be obtained by taking the first half of the eigenvectors of $\mathbf{D}_i$ with the largest eigenvalue and normalised to unit norm:

$$\mathbf{D}_i = \begin{bmatrix} \mathbf{A}_{ii} & \mathbf{b}_i\mathbf{b}_i^* \\ \mathbf{I}_{n_i} & \mathbf{A}_{ii} \end{bmatrix} \tag{123}$$

$$\mathbf{b}_i = \sum_{j=1(j\neq i)}^{n_g} \mathbf{A}_{ij}\overline{\mathbf{u}}_j \tag{124}$$

The MPV of $\mathbf{U}'$ now can be obtained given other modal parameters. The MPV of the remaining parameters can be obtained through numerical optimisation of the NLLF. It should be noted that some of modal parameters are subjected to constraints. Specifically,

$$\sum_{i=1}^{n_g} \|\mathbf{u}_i\|^2 = 1 \tag{125}$$

due to the unit norm of the global mode shape and

$$\chi_{ij} \leq 1 \tag{126}$$

Comparing to numerical techniques (e.g., Lagrange multiplier), it is more efficient to adopt a parameterisation scheme that can automatically take care of these constraints.

Define

$$S_i = \sqrt{S}\,\|\mathbf{u}_i\| \qquad i = 1,...,n_g \tag{127}$$

The constraints in Eq.(125) have now been transferred into the scaling of the modal force PSD and the resulting variable S_i is unconstrained. The condensed PSD matrix $\mathbf{E}'_k$ then can be expressed as:

$$\mathbf{E}'_k = D_k diag\{S_i\}\boldsymbol{\chi} diag\{S_i\} + S_e \mathbf{I}_{n_g} \tag{128}$$

For the constraints of χ_{ij} in Eq.(126), χ_{ij} can be parameterised through angles $u_{ij}, v_{ij} \in R^n \left(i = 1,...,n_g; j < i\right)$ such that

$$\chi_{ij} = \left(\sin u_{ij}\right)\exp\left(\mathbf{i}v_{ij}\right) \tag{129}$$

The constraints then can be automatically satisfied.

Based on the above parameterisation scheme, the unconstrained parameters S_i and $\{u_{ij}, v_{ij}\}$ can be used for optimisation in place of S, $\{\|\mathbf{u}_i\|\}$ and $\{\chi_{ij}\}$. Once the MPV of S_i and $\{u_{ij}, v_{ij}\}$ have been found, the MPV of S, $\{\|\mathbf{u}_i\|\}$ and $\{\chi_{ij}\}$ can be recovered. Specifically

$$\hat{S} = \sum_{i=1}^{n_g} \hat{S}_i^2 \tag{130}$$

$$\|\hat{\mathbf{u}}_i\| = \frac{\hat{S}_i^2}{\sqrt{\sum_{i=1}^{n_g} \hat{S}_i^2}} \qquad i = 1,...,n_g \tag{131}$$

where a hat '^' denotes MPV.

The MPV of global mode shape then can be recovered based on the MPV of $\{\|\mathbf{u}_i\|\}$ and $\{\overline{\mathbf{u}}_i\}$ as

$$\hat{\boldsymbol{\varphi}} = \begin{bmatrix} s_1 \|\hat{\mathbf{u}}_1\| \hat{\overline{\mathbf{u}}}_1 \\ \vdots \\ s_i \|\hat{\mathbf{u}}_i\| \hat{\overline{\mathbf{u}}}_i \\ \vdots \\ s_{n_g} \|\hat{\mathbf{u}}_{n_g}\| \hat{\overline{\mathbf{u}}}_{n_g} \end{bmatrix} \tag{132}$$

Here $s_i = \pm 1 \left(i = 1,...,n_g \right)$ is the sign of the relative direction between partial mode shapes. It should be noted that swapping the sign of the coherence value and the partial mode shapes gives the same $\mathbf{E}_k$ and hence the NLLF. Without additional assumptions on the sign of coherence (e.g., the coherence value shall be positive in the low frequency range when the synchronisation degree between two synchronous data groups are high), the relative direction between partial mode shapes cannot be directly identified. This is one fundamental limitation when dealing with asynchronous ambient data. In real implementation, the relative direction among partial mode shapes can be either determined intuitively based on spatial continuity or an empirical analysis of the coherence among different synchronous data groups.

5.3 High signal-to-noise asymptotics

The asymptotic behaviours of modal parameters under high SNR condition are investigated in this section. It turns out that the asymptotic MPVs of $\{\overline{\mathbf{u}}_i\}$, S_e and S_i can be obtained directly based on the measured data, which can be used as initial guesses for the iterative procedure.

Asymptotic MPV of prediction error

For high SNR condition, $\mathbf{E}'_k$ in Eq.(102) is dominated by the modal response (i.e., the first term) and hence asymptotically independent from the prediction error S_e. The NLLF in Eq.(107) then depends on S_e through the first and third term. Rearrange these two terms as

$$\begin{aligned}&\left(n-n_g\right)N_f \ln S_e + S_e^{-1}\left(d-d'\right)\\&=\left(n-n_g\right)N_f\left\{\ln S_e + S_e^{-1}\left[\left(d-d'\right)/\left(n-n_g\right)N_f\right]\right\}\end{aligned} \tag{133}$$

which are of the form $\ln x + a/x$. This form has a unique minimum of $1+\ln a$ at $x=a$. The asymptotic MPV of S_e then can be given by

$$\hat{S}_e \sim \left(d-d'\right)/\left(n-n_g\right)N_f \tag{134}$$

Asymptotic MPV of $\overline{\mathbf{u}}_i$

For high SNR condition, the modal response is much larger than the prediction error (i.e. $SD_k \gg S_e$). $\mathbf{E}'_k$ is in the order of SD_k and $S_e\mathbf{E}'^{-1}_k \ll \mathbf{I}_{n_g}$. The term $\mathbf{I}_{n_g} - S_e\mathbf{E}'^{-1}_k$ in $\mathbf{A}$ (see Eq.(117)) can be approximated as an identity matrix so that

$$\mathbf{A} \sim \sum_k \mathbf{F}_k^* \mathbf{F}_k \tag{135}$$

which becomes a constant matrix with off-diagonal partitions equal to zero (i.e., $\mathbf{A}_{ij} = \mathbf{0}$ for $i \neq j$). Eq.(122) now can be expressed as

$$\mathbf{A}_{ii}\overline{\mathbf{u}}_i = \lambda_i \overline{\mathbf{u}}_i \qquad\qquad i = 1,...,n_g \tag{136}$$

which is a standard eigenvalue problem. The asymptotic MPV of $\overline{\mathbf{u}}_i$ can be obtained as the eigenvector of $\mathbf{A}_{ii}$ with the largest eigenvalues (normalised to unit norm).

Asymptotic MPV of S_i

The asymptotic MPV of S_i cannot be directly obtained from the NLLF under high SNR condition. This is because the determinant and inverse of $\mathbf{E}_k'$ depends non-trivially on $\boldsymbol{\chi}$ and $\{\|\mathbf{u}_i\|\}$, whose analytical forms cannot be explicitly expressed in terms of S_i. However, the asymptotic MPV of S_i can be estimated by noting that different synchronous data groups share the same modal force PSD S. When analysing the data separately within each group, the identified modal force PSD is scaled by the square norm of the partial mode shape (i.e., $\|\mathbf{u}_i\|^2$) due to the unit norm constraint of mode shapes. Since the data channels in each data group are synchronised, the asymptotic MPV of S_i can be estimated using based on the existing Bayesian formulation for synchronous data [78]. Specifically,

$$\hat{S}_i \sim \sqrt{N_f^{-1}\sum_{k=1}^{N_f}\overline{\mathbf{u}}_i^T D_k^{-1}\mathcal{F}_{ik}\mathcal{F}_{ik}^{*}\overline{\mathbf{u}}_i} \tag{137}$$

For $i = 1,...,n_g$.

5.4 Summary of procedure

Based on the foregoing analysis, the procedure for determining the MPV of modal parameters can be summarised as follow.

Step I. Initial Guess

1) Calculate the FFT of the measured data and plot the singular value spectrum.
2) Select the frequency band for the mode of interest.

3) Pick the initial guess of f from the singular value spectrum and set the initial guess of ζ as 1%.

4) Calculate the initial guess of $\overline{\mathbf{u}}_i \;\; i=1,...,n_g$ as the eigenvector with the largest eigenvalue of $\mathbf{A}_{ii}$ in Eq.(136).

5) Calculate the initial guess of S_e using Eq.(134).

6) Calculate the initial guess of $S_i \;\; i=1,...,n_g$ using Eq.(137).

7) The angles $\{u_{ij}, v_{ij}\}$ can be nominally assigned as 0.1.

Step II. Iteration Phase

In the following, parameters that are not updated are kept at their current value during iteration.

8) Update $\{u_{ij}, v_{ij}\}$ by minimising L in Eq.(107) .

9) Update $\{f, \zeta\}$ by minimising L in Eq.(107).

10) Update $\{S_i\}$ by minimising L in Eq.(107).

11) Update S_e by minimising L in Eq.(107).

12) Update $\overline{\mathbf{u}}_i$ ($i=1,...,n_g$) as the first half of the eigenvectors of $\mathbf{D}_i$ in Eq.(123) with the largest eigenvalue and normalised to unit norm.

Repeat Steps 8) to 12) until convergence.

Step III. MPV of S and $\boldsymbol{\varphi}$

13) Calculate the MPV of S using Eq.(130).

14) Calculate the MPV of $\{\|\mathbf{u}_i\|\}$ using Eq.(131).

15) Calculate the MPV of $\boldsymbol{\varphi}$ using Eq.(132)

Chapter 6: Illustrative Examples

The consistency of the proposed asynchronous data model and the Bayesian modal identification methods are verified using synthetic, laboratory and field test data in this chapter. The eigenvalue properties of the PSD matrix based on the proposed asynchronous data model are verified using simulated data, where there is no modelling error. The feasibility of the proposed model is then investigated using real asynchronous data measured on a laboratory shear frame structure. A synthetic data example is presented to verify the consistency of the proposed Bayesian zero and general coherence methods. For the Bayesian zero coherence method, the potential modelling error due to zero coherence approximation is also investigated through a parametric study. Ambient vibration data measured from a multi-storey laboratory shear building model is used to illustrate the proposed Bayesian modal identification methods with both zero coherence and general coherence assumptions. These two proposed methods are also validated using the asynchronous data measured on a full-scale building, where the identification results are compared with those identified based on synchronous data.

6.1 Synthetic data examples

6.1.1 Verification of asynchronous data model

Consider a set of simulated structural response data with six measured DOFs and two synchronous data groups. The first synchronous data group contains the first three DOFs and the second group contains the last three DOFs. One mode is assumed for the structure with a natural frequency of 5Hz and a damping ratio of 1%. The measured mode shape of this mode is assumed to be $\begin{bmatrix}1 & 2 & 3 & 4 & 5 & 6\end{bmatrix}/\sqrt{91}$ (normalised to unit norm) corresponding to the six measured DOFs. The structure is

subjected to i.i.d. Gaussian white noise excitation with a PSD of $S = 1\times10^{-8}\,\mathrm{g}^2/\mathrm{Hz}$. To simulate asynchronous data, the modal excitation between these two synchronous data groups are correlated with a coherence of χ. This is done by generating two independent modal excitations (say p_1 and p_2), using p_1 as the modal excitation for the first group and $\chi p_1 + \sqrt{1-\chi^2}\,p_2$ for the second group. The coherence of modal response between these two groups is equal to the coherence between their modal excitation. The data are contaminated by white noise measurement error with a PSD of $1\times10^{-7}\,\mathrm{g}^2/\mathrm{Hz}$ for all data channels. The data are generated for 1000s with a sampling rate of 100Hz.

Six scenarios with different coherence values, i.e., $\chi = 0$ (perfectly asynchronous), 0.2, 0.4, 0.6, 0.8, 1 (synchronous), are considered to illustrate the eigenvalue properties of the PSD matrix and validate the proposed asynchronous model. For each scenario, the sample PSD matrix of the simulated data is obtained by averaging 40 non-overlapping segments (each 25s), giving a frequency resolution of 0.04Hz. *Figure 6.1-1* shows the root SV spectrum of these six scenarios. The solid lines illustrate the square root of the eigenvalues of the sample PSD matrix and the dashed lines illustrate the theoretical values calculated based on the proposed asynchronous data model using the given coherence values and modal properties. These two types of line agree well with each other, verifying the consistency of the theoretical prediction. Although details are omitted here, the eigenvectors calculated based on the proposed asynchronous data model are also consistent with those of the sample PSD matrix at the natural frequency of the mode, with MAC values extremely close to 1 (to 4 decimal places).

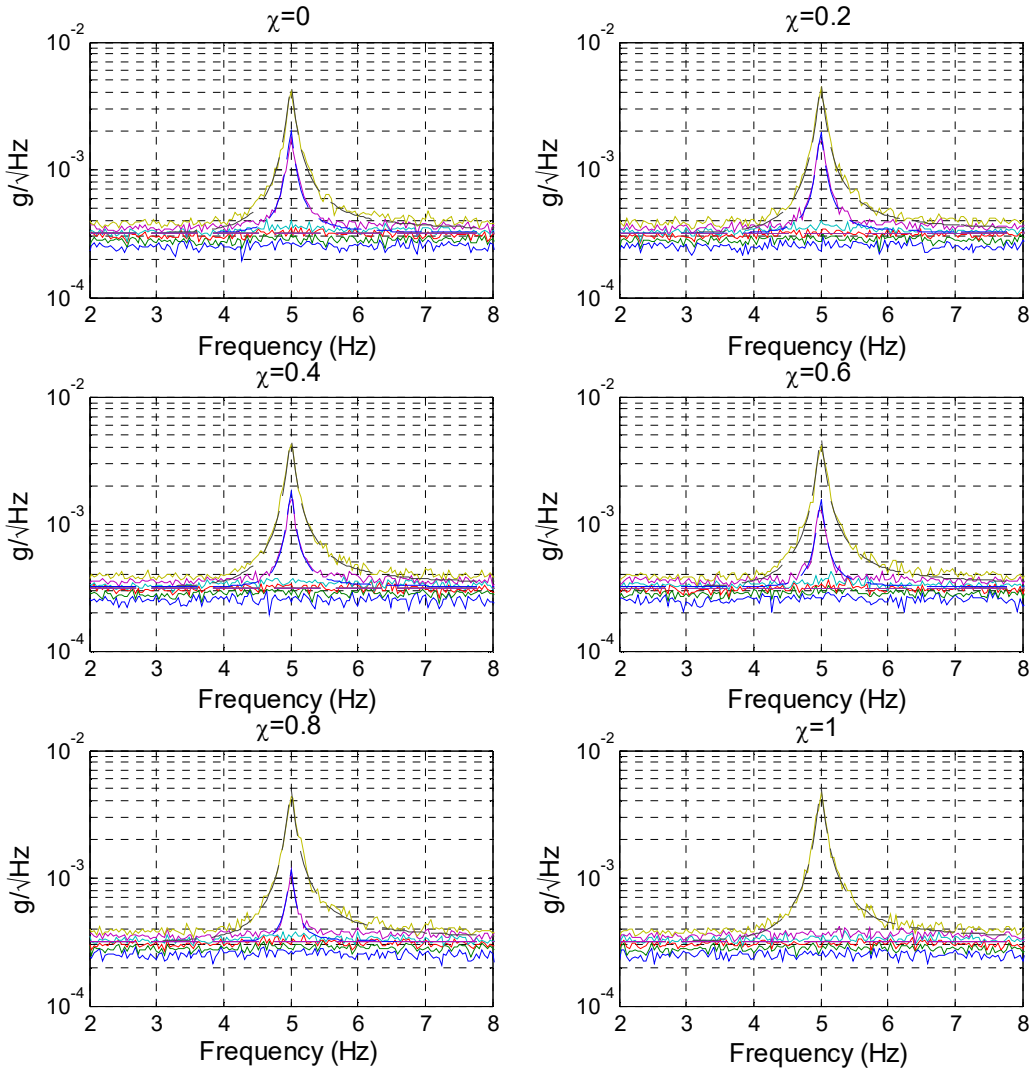

Figure 6.1-1. Root SV spectrum with different coherence values (solid line: estimated value from sample PSD; dashed line: theoretical values)

6.1.2 Verification of Bayesian zero and general coherence methods

The synthetic data simulate a six-storey shear building with a uniform inter-storey stiffness of 3000kN/mm and floor mass of 600 tons. The natural frequency of the first mode can be calculated as 2.71Hz. The damping ratios of all the modes are assumed to be 1%. I.i.d. Gaussian white noise excitation with a (root) PSD of

$11.8\text{N}/\sqrt{\text{Hz}}$ is applied to the structure in the lateral direction of each floor, which is the typical excitation level in full-scale ambient tests. *Figure 6.1-2* shows the configuration of the test. Two synchronous data groups are assumed, measuring the acceleration response of 1/F to 3/F and 4/F to 6/F, respectively. These two synchronous groups are not fully synchronised, the coherences of the measured modal excitations between these two groups are assumed to be 0.8, 0.6, 0.6, 0.5, 0.2 and 0 for the six modes, respectively. The data are contaminated by i.i.d Gaussian white noise with a PSD of $90\mu g^2/\text{Hz}$ for all data channels, which simulates the typical noise level of force-balanced accelerometers used in full-scale tests. Twenty minutes of data are generated for modal analysis with a sampling rate of 100Hz.

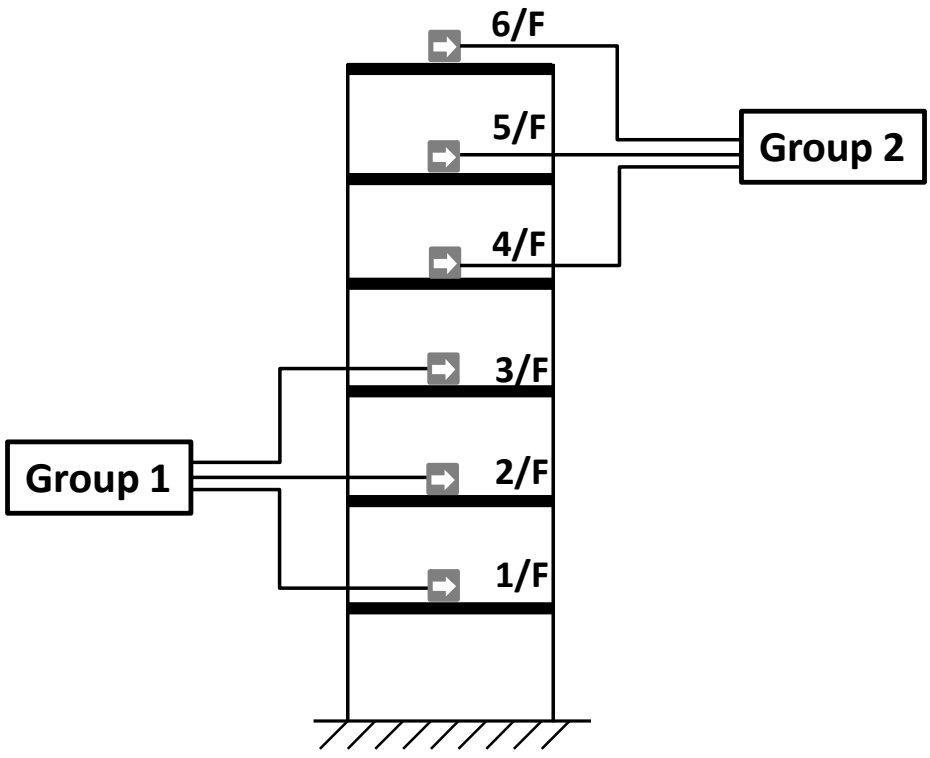

Figure 6.1-2. Test configuration, synthetic data example

The root SV spectrum of the data is shown in *Figure 6.1-3*. Modal identification focuses on the six modes indicated in the spectrum. The selected frequency bands and the initial guess of natural frequencies for these modes are also shown with symbols '[-]' and 'o' in the figure, respectively. An additional spectral peak can be found for each mode, indicating the asynchronisation issue among the measured data channels. The MPV of modal parameters determined using the proposed Bayesian methods and the exact values that generated the data are listed in *Table 6.1-1*. The MPVs are quite close to the exact ones for both zero and general coherence methods. The identified prediction error PSD tends to be larger than the exact values for higher modes, which is mainly due to the modelling error caused by the modal contribution of lower modes. For the general coherence method, small discrepancies can be found in the phase of the identified coherence values for Mode 4 and Mode 5. This may be due to the effect of non-resonant part of other modes as well as the measurement error. *Figure 6.1-4* plots the exact mode shape values (solid lines) and the identified ones (where circles denote the ones identified based on zero coherence method and the squares denote the ones identified based on general coherence method). The identified mode shapes based on these two methods almost coincide and are very close to the exact values, with MACs extremely close to 1 (up to 4 decimal points). The proposed Bayesian zero and general coherence methods can both provide a good estimation of modal parameters based on asynchronous data. In addition, the general coherence method is also capable of quantifying the coherence values among the synchronous data groups. In this example, different coherence values are assumed for different modes. Synthetic data assuming the same coherence value for all the modes have also been investigated, showing qualitatively the same results.

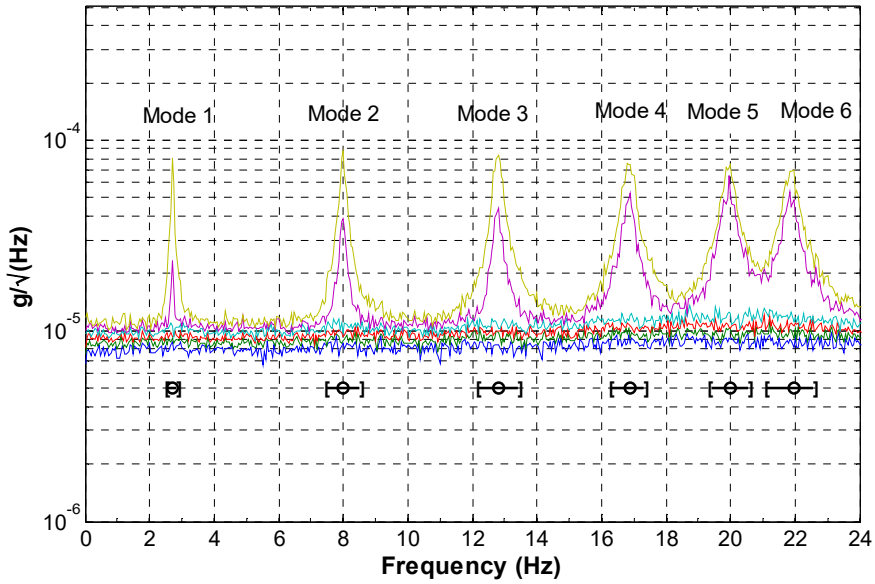

Figure 6.1-3. Root SV spectrum, synthetic data example

Table 6.1-1 Modal identification results, synthetic data example

Modal Parameters		Mode					
		1	2	3	4	5	6
f(Hz)	Exact	2.713	7.981	12.785	16.847	19.930	21.854
	Zero Coh.	2.710	7.980	12.789	16.841	19.935	21.850
	Gen. Coh.	2.710	7.978	12.788	16.840	19.934	21.850
$\zeta(\%)$	Exact	1.00	1.00	1.00	1.00	1.00	1.00
	Zero Coh.	0.95	1.02	0.98	1.00	1.01	1.04
	Gen. Coh.	0.96	1.02	0.97	0.99	1.04	1.03
$\sqrt{S}\left(\mu g/\sqrt{Hz}\right)$	Exact	2.00	2.00	2.00	2.00	2.00	2.00
	Zero Coh.	1.96	1.97	1.90	1.87	1.85	1.73
	Gen. Coh.	1.97	1.97	1.90	1.87	1.87	1.74
$\sqrt{S_e}\left(\mu g/\sqrt{Hz}\right)$	Exact	9.49	9.49	9.49	9.49	9.49	9.49
	Zero Coh.	9.49 9.12	9.72 9.55	9.81 9.58	10.24 10.16	10.47 10.13	10.62 10.16
	Gen. Coh.	9.30	9.64	9.70	10.20	10.30	10.39
χ	Exact	0.8	0.6	0.6	0.5	0.2	0
	Gen. Coh.	0.8	0.6	0.6	0.4 +0.3i	0.1 -0.1i	0

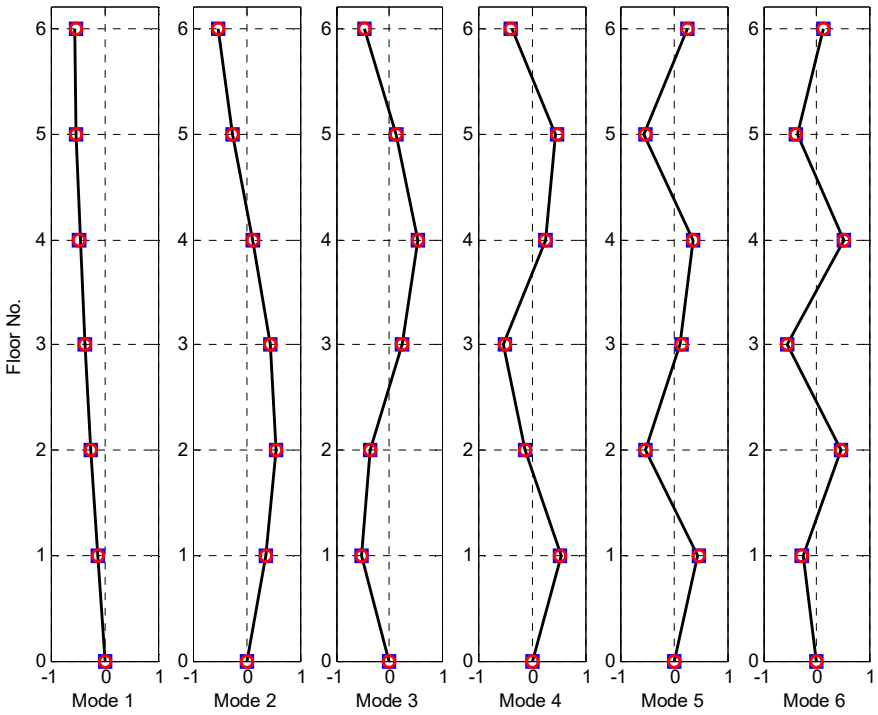

Figure 6.1-4. Mode shape MPV, synthetic data example (solid line: exact value; circle: zero coherence method; square: general coherence method)

6.1.3 Bias estimation of Bayesian zero coherence method

To facilitate identification, the proposed fast Bayesian method in Chapter 4 assumes zero coherence among different synchronous data groups. This assumption may not be true for real asynchronous data, which may cause modelling errors. The effect of such modelling error on the MPV and identification uncertainty is investigated in this example through a parametric study using synthetic data. Potential bias caused by the modelling error is investigated by comparing Bayesian and frequentist statistics. It has been shown that if there is no modelling error, the ensemble average of modal parameter MPV is approximately equal to the exact value that generated the synthetic data and the posterior variance is approximately equal to the ensemble variance of MPV [91]. The effect of the modelling error can be illustrated based on the discrepancy between these two types of values.

The same simulated structure and test configurations have been considered in this example as the ones in Section 6.1.2. It is a six-storey shear building with uniform inter-storey stiffness of 3000kN/mm and floor mass of 600t. The natural frequency of the first mode is calculated to be 2.71Hz. The damping ratios of all the modes are set to be 1%. The excitation subjecting to the structure is assumed to be i.i.d. Gaussian white noise with a PSD of $11.8\text{N}/\sqrt{\text{Hz}}$ in the horizontal direction, giving the resulting acceleration response in the order of few tens of $\mu\text{g}/\sqrt{\text{Hz}}$ around the resonance peak of modes. The structural responses in horizontal direction on all storeys are measured. The data comprises two synchronous groups measuring 1/F to 3/F (Group 1) and 4/F to 6/F (Group 2). To simulate asynchronous data, the modal excitation between these two groups are correlated with a coherence of χ, which will be varied in the parametric study. The data are contaminated by Gaussian white noise with PSDs of $40\mu\text{g}^2/\text{Hz}$ and $90\mu\text{g}^2/\text{Hz}$ for Group 1 and 2, respectively.

Consider four scenarios with increasing coherence values, i.e., $\chi = 0$ (totally asynchronous, no modelling error), 0.2 (low coherence), 0.6 (high coherence) and 1 (perfectly synchronous). For each scenario, 1000 i.i.d. acceleration data sets are generated to investigate the statistic properties of MPV and identification uncertainty. Each data set is sampled at 100Hz with a duration of 500s. *Figure 6.1-5* shows the root SV spectrum of one data set with a coherence of 0.2 (as a reference). There are two significant peaks in the spectrum, indicating two asynchronous data groups. The horizontal bars '[-]' denote the selected frequency band for modal identification and the circles denote the initial guesses of natural frequency. Modal identification focuses on the six modes indicated in the figure. The modes are identified separately within each selected frequency band. As a typical case, *Figure 6.1-6* and *Figure*

6.1-7 show the histogram of the natural frequency and damping ratio MPVs among the data sets for coherence of 0.2, respectively. It can be seen that MPVs determined among the data sets generally follow Gaussian distributions with mean values close to the exact ones. Compared to natural frequency, the MPVs of damping ratio have larger variation.

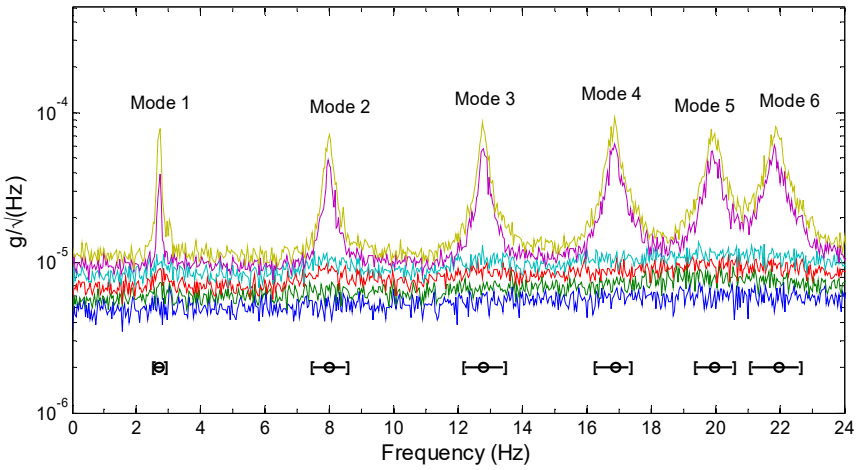

Figure 6.1-5. Root SV spectrum of a data set, coherence=0.2

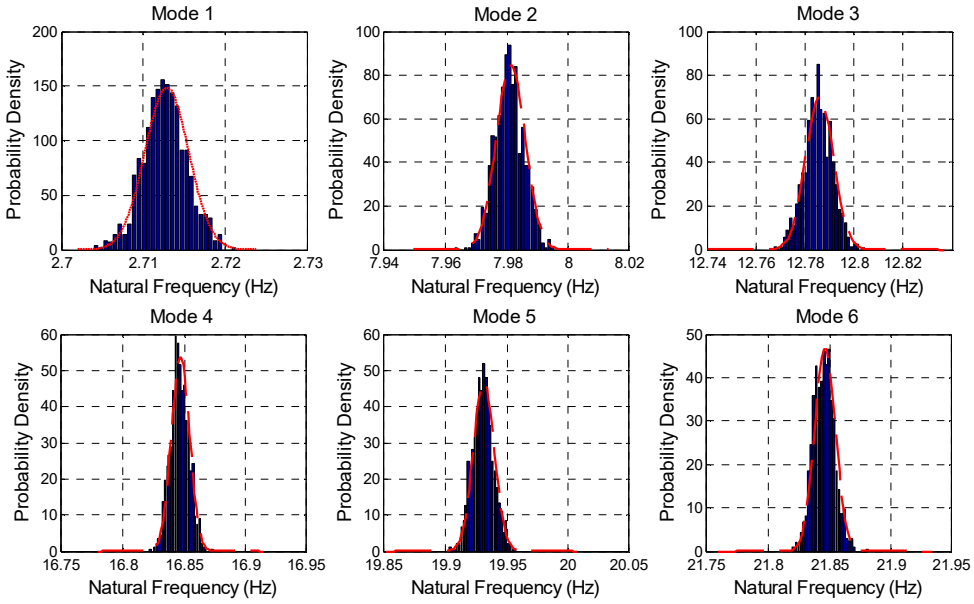

Figure 6.1-6. Histogram of natural frequency MPVs, coherence=0.2 (bar: histogram; dashed line: normal distribution)

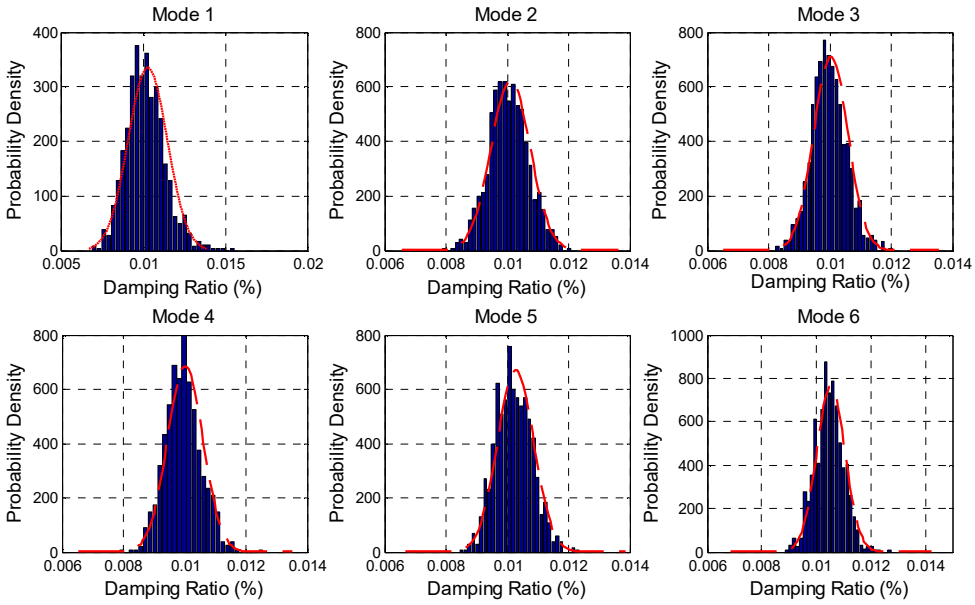

Figure 6.1-7. Histogram of damping ratio MPVs, coherence=0.2 (bar: histogram; dashed line: normal distribution)

Table 6.1-2 to *Table 6.1-5* summarise the frequentist and Bayesian statistics of MPV and posterior uncertainty for these four scenarios, respectively. The first column 'Exact' lists the exact modal parameters used for data generation. The second column shows the sample mean of MPV among the 1000 data sets. The ratios between these two values are shown in the third column. The ratios are very close to 1, suggesting little or practically no bias in the MPV of natural frequencies and damping ratios. The forth column 'Freq.' (short for 'frequentist') shows the sample c.o.v. of the MPV (i.e., the ratio of the sample standard deviation to the sample mean of MPV) and the fifth column 'Bay.' (short for 'Bayesian') shows the sample root mean square value of the posterior c.o.v. of the identified modal parameters. The final column shows the ratio between these two values. The ratio stays above 1 and increases with the coherence value, suggesting an increasing under-estimation of the identification uncertainty due to the zero coherence approximation. Nevertheless, the bias is not significant unless the coherence is very high. For the coherence of 0.6, the under-

estimation is about 10%. In the extreme case when the coherence is 1 (perfectly synchronous), the under-estimation is 40%. In this case, the data among the channels are actually synchronised and it is more appropriate to identify the modal parameters using conventional methods that assumes synchronous data.

Table 6.1-2 Sample and Bayesian statistics of identification results, coherence=0

Mode		Exact (A)	Sample Mean (B)	A/B	c.o.v.		C/D
					Freq. (%) (C)	Bay. (%) (D)	
$f(\mathrm{Hz})$	1	2.713	2.713	1.00	0.09	0.10	0.98
	2	7.981	7.981	1.00	0.06	0.06	1.05
	3	12.786	12.786	1.00	0.04	0.04	0.95
	4	16.847	16.847	1.00	0.04	0.04	1.04
	5	19.930	19.931	1.00	0.04	0.04	0.99
	6	21.854	21.846	1.00	0.04	0.04	0.96
$\zeta(\%)$	1	1	1.02	0.98	11.55	11.20	1.03
	2	1	1.01	0.99	6.35	6.36	1.00
	3	1	1.01	0.99	5.44	5.38	1.01
	4	1	1.00	1.00	5.77	5.78	1.00
	5	1	1.02	0.98	5.64	5.48	1.03
	6	1	1.05	0.95	4.75	4.86	0.98

Table 6.1-3 Sample and Bayesian statistics of identification results, coherence=0.2

Mode		Exact (A)	Sample Mean (B)	A/B	c.o.v.		C/D
					Freq. (%) (C)	Bay. (%) (D)	
$f(\mathrm{Hz})$	1	2.713	2.713	1.00	0.10	0.10	1.02
	2	7.981	7.981	1.00	0.06	0.06	1.06
	3	12.786	12.786	1.00	0.04	0.04	1.00

	4	16.847	16.847	1.00	0.04	0.04	1.03
	5	19.930	19.931	1.00	0.04	0.04	1.05
	6	21.854	21.846	1.00	0.04	0.04	1.02
$\zeta(\%)$	1	1	1.02	0.98	11.62	11.20	1.04
	2	1	1.01	0.99	6.32	6.35	1.00
	3	1	1.00	1.00	5.59	5.38	1.04
	4	1	1.00	1.00	5.81	5.78	1.01
	5	1	1.03	0.97	5.78	5.48	1.05

Table 6.1-4 Sample and Bayesian statistics of identification results, coherence=0.6

Mode		Exact (A)	Sample Mean (B)	A/B	c.o.v.		C/D
					Freq. (%) (C)	Bay. (%) (D)	
$f(\mathrm{Hz})$	1	2.713	2.713	1.00	0.11	0.10	1.16
	2	7.981	7.981	1.00	0.06	0.06	1.14
	3	12.786	12.786	1.00	0.05	0.04	1.09
	4	16.847	16.847	1.00	0.05	0.04	1.11
	5	19.930	19.932	1.00	0.05	0.04	1.13
	6	21.854	21.846	1.00	0.04	0.04	1.08
$\zeta(\%)$	1	1	1.02	0.98	13.02	11.20	1.16
	2	1	1.01	0.99	7.26	6.36	1.14
	3	1	1.00	1.00	6.20	5.38	1.15
	4	1	1.00	1.00	6.42	5.78	1.11
	5	1	1.03	0.97	6.12	5.48	1.12
	6	1	1.05	0.95	5.58	4.86	1.15

Table 6.1-5 Sample and Bayesian statistics of identification results, coherence=1

Mode		Exact (A)	Sample Mean (B)	A/B	c.o.v.		C/D
					Freq. (%) (C)	Bay. (%) (D)	

$f(\text{Hz})$	1	2.713	2.713	1.00	0.13	0.10	1.36
	2	7.981	7.982	1.00	0.08	0.06	1.38
	3	12.786	12.786	1.00	0.06	0.04	1.33
	4	16.847	16.846	1.00	0.06	0.04	1.36
	5	19.930	19.932	1.00	0.05	0.04	1.35
	6	21.854	21.846	1.00	0.05	0.04	1.33
$\zeta(\%)$	1	1	1.02	0.98	15.26	11.22	1.36
	2	1	1.01	0.99	8.47	6.36	1.33
	3	1	1.00	1.00	7.57	5.38	1.41
	4	1	1.01	0.99	8.04	5.78	1.39
	5	1	1.03	0.97	7.66	5.48	1.40
	6	1	1.05	0.95	6.47	4.86	1.33

The effect of zero coherence approximation on the identification uncertainty of the mode shape is also investigated. The results are summarised in *Table 6.1-6* to *Table 6.1-9* for the four scenarios, respectively. The first column 'Freq.' (short for 'frequentist') shows the sample mean of MAC between the MPV of mode shape and the exact one. The values are all close to 1, suggesting practically no bias in the identified mode shapes. The second column 'Bay.' (short for 'Bayesian') shows the sample mean of the expected MAC, which can be calculated based on the mode shape c.o.v. as [117]:

$$\text{Expected MAC} = \left(1 + \text{mode shape c.o.v.}^2\right)^{-1/2} \tag{138}$$

The ratio between the frequentist and Bayesian identification uncertainty is shown in the third column, which is close to 1 for all the four scenarios. This illustrates that the zero coherence approximation does not cause bias in the identification uncertainty of the mode shape.

Table 6.1-6 Sample and Bayesian statistics of mode shapes, coherence=0

Mode	Freq. (C)	Bay. (D)	C/D
1	0.99943	0.99944	0.99999
2	0.99975	0.99977	0.99998
3	0.99976	0.99983	0.99994
4	0.99962	0.99982	0.99980
5	0.99947	0.99983	0.99964
6	0.99922	0.99986	0.99936

Table 6.1-7 Sample and Bayesian statistics of mode shapes, coherence=0.2

Mode	Freq. (C)	Bay. (D)	C/D
1	0.99946	0.99944	1.00003
2	0.99976	0.99977	0.99999
3	0.99977	0.99983	0.99994
4	0.99965	0.99982	0.99983
5	0.99946	0.99983	0.99963
6	0.99923	0.99986	0.99937

Table 6.1-8 Sample and Bayesian statistics of mode shapes, coherence=0.6

Mode	Freq. (C)	Bay. (D)	C/D
1	0.99953	0.99944	1.00010
2	0.99979	0.99977	1.00002
3	0.99980	0.99983	0.99997
4	0.99969	0.99982	0.99987
5	0.99949	0.99983	0.99966
6	0.99928	0.99986	0.99942

Table 6.1-9 Sample and Bayesian statistics of mode shapes, coherence=1

Mode	Freq. (C)	Bay. (D)	C/D
1	0.99973	0.99944	1.00029
2	0.99989	0.99977	1.00012
3	0.99993	0.99983	1.00010
4	0.99993	0.99982	1.00012
5	0.99990	0.99983	1.00007
6	0.99976	0.99986	0.99991

The parametric study in this section verifies the consistency of the proposed Bayesian method with zero coherence assumption and investigates the effect of modelling error on the modal identification results. The number of data sets is large enough so that the statistical estimation error is negligible. Repeated trials have also been conducted, showing qualitatively the same results. The foregoing analysis indicates that the modelling error due to zero coherence assumption practically causes no bias in the MPV of modal parameters. There is an under-estimation in the posterior uncertainty. Nevertheless, such effect is not significant unless the coherence among the synchronous data groups is extremely high.

6.2 Laboratory data examples

6.2.1 Single storey shear frame model

In this section, the asynchronous data model is validated using real asynchronous OMA data based on a laboratory example. The instrumented structure is a one-storey laboratory shear frame structure as shown in *Figure 6.2-8*. Three piezoelectric accelerometers were placed on the first floor of the structure measuring the structural response in the weak direction. Within the frequency range of interest, the

measurement noise is about $2\times10^{-5}\,\mathrm{g}/\sqrt{\mathrm{Hz}}$. *Figure 6.2-9* shows the schematic diagram of the experiment setup. Sensor A and B are connected to the same DAQ units so that the analogue signals from these sensors are sampled synchronously based on the same clock. The signal in Sensor C is recorded using another DAQ unit, where the sampled data from Sensor C is not synchronised with those from Sensor A and B. In the following discussion, the data from Sensor A and B are combined and referred as the 'synchronous data set' while the data from Sensor A and C are combined and referred as the 'asynchronous data set'. The DAQ units are connected to the sample computer and controlled to start/stop measuring at the same time with the sample sampling rate setting. Two hours of ambient vibration data was measured with a sampling rate of 2048Hz.

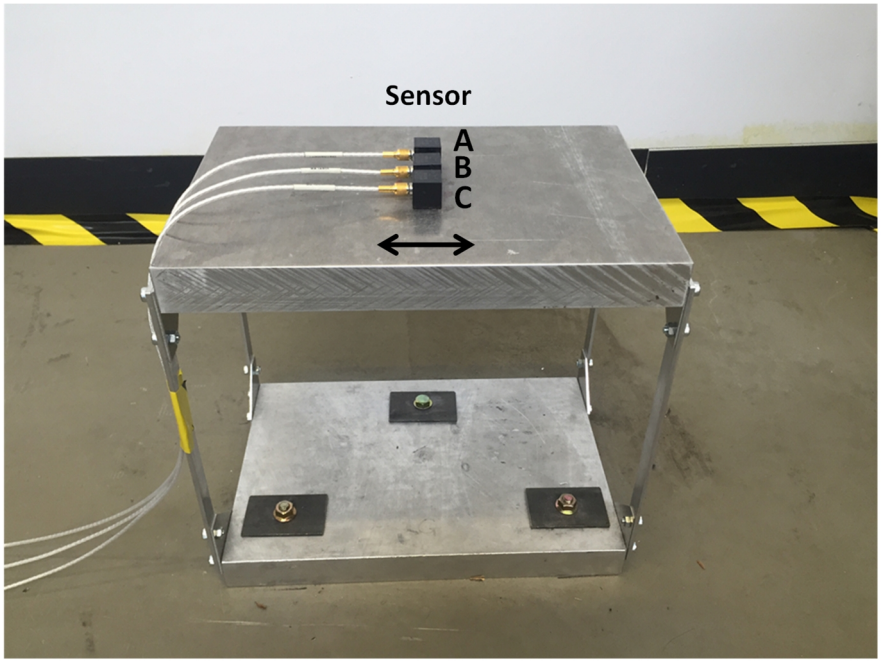

Figure 6.2-8. One-storey shear frame laboratory model

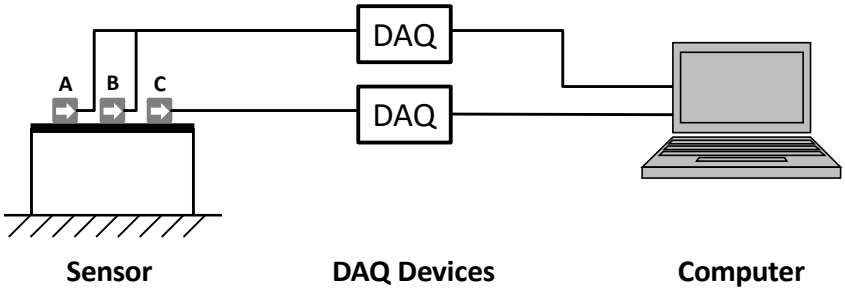

Figure 6.2-9. Experimental setup

Figure 6.2-10 shows the root PSD and SV spectra for both synchronous and asynchronous data set. The spectral peaks in the figure indicate the presence of a mode around 10Hz. The PSD spectra of these two data sets almost coincide. This is reasonable as the PSD spectrum only plots the diagonal entries of the PSD which cannot reflect the time synchronisation issue among the data channels. For asynchronous data set, the PSD spectra among the data channels agree well with each other. Since the two data channels measure the structural response in the same duration, this verifies that different synchronous data groups share the same PSD of modal force. Time synchronisation issue can be revealed in the SV spectra. For synchronous data set, there is only one peak and the remaining flat lines reflect the measurement noise (as shown in *Figure 6.2-10*(c)). However, for asynchronous data set, there are two spectral peaks at the same frequency with almost the same spread (as shown in *Figure 6.2-10*(d)). This is consistent with the eigenvalue properties based on the proposed asynchronous data model. The number of peaks indicates the number of synchronous data groups among the measured data channels. The peaks have the same variation with frequency due to the same dynamic amplification factor in the eigenvalues.

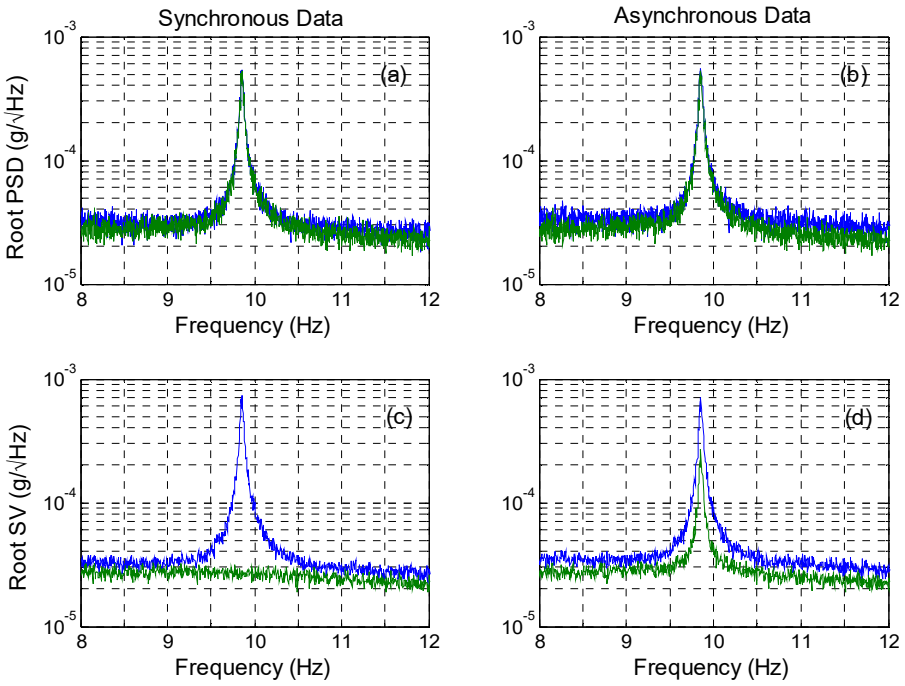

Figure 6.2-10. Root PSD and SV spectrum of synchronous (left column) and asynchronous data set (right column)

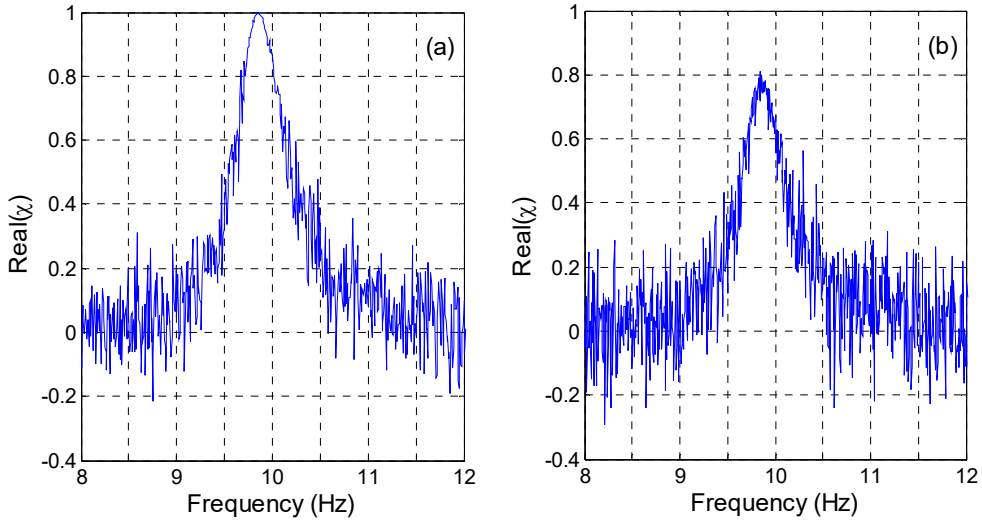

Figure 6.2-11. Real part of coherence for (a) synchronous and (b) asynchronous data set

According to the proposed asynchronous data model, the magnitude of eigenvalues depends on the coherence between the modal responses among the synchronous data groups. To verify the consistency of the asynchronous data model, the coherence value among the data groups needs to be estimated. However, the FFT of the data

contains the modal responses as well as prediction error. The coherence value cannot be directly obtained without identification. In view of this, it is estimated using the FFT data around the resonance peak of the mode where the modal response is much larger than the prediction error. *Figure 6.2-11* shows the real part of the coherence for synchronous and asynchronous data set, respectively. It can be seen that the coherence for synchronous data set is very close to one around the resonance peak of the mode. This is not the case for asynchronous data set, however. The real part of the coherence is about 0.8 for asynchronous data set near the resonance peak. The coherence decreases for frequencies away from the resonance peak for both data sets. This is because the FFT data are no longer dominated by modal response. To help estimate the coherence value of the asynchronous data set, the ratio of the coherence for the asynchronous data to the synchronous data set is plotted in *Figure 6.2-12*. The ratio does not vary a lot within the resonance band, which can be assumed to be constant. Assume that the coherence of the synchronous data set to be 1, the coherence for the asynchronous data set is estimated to be 0.79 after averaging. The modal parameters of the structure are estimated from the synchronous data set using the Bayesian FFT method [79]. The selected frequency band is [9.6 10.1]Hz (hand-picked), which yields a most probable value of $f = 9.855\text{Hz}$ (natural frequency), $\zeta = 0.17\%$ (damping ratio), $\sqrt{S} = 2.35\mu\text{g}/\sqrt{\text{Hz}}$ (root modal force PSD) and $\sqrt{S_e} = 27.1\mu\text{g}/\sqrt{\text{Hz}}$ (root measurement noise PSD). The MPV of mode shape is $[0.71 \quad 0.71]^T$, which is consistent with the fact that Sensor A and B measure the same DOF.

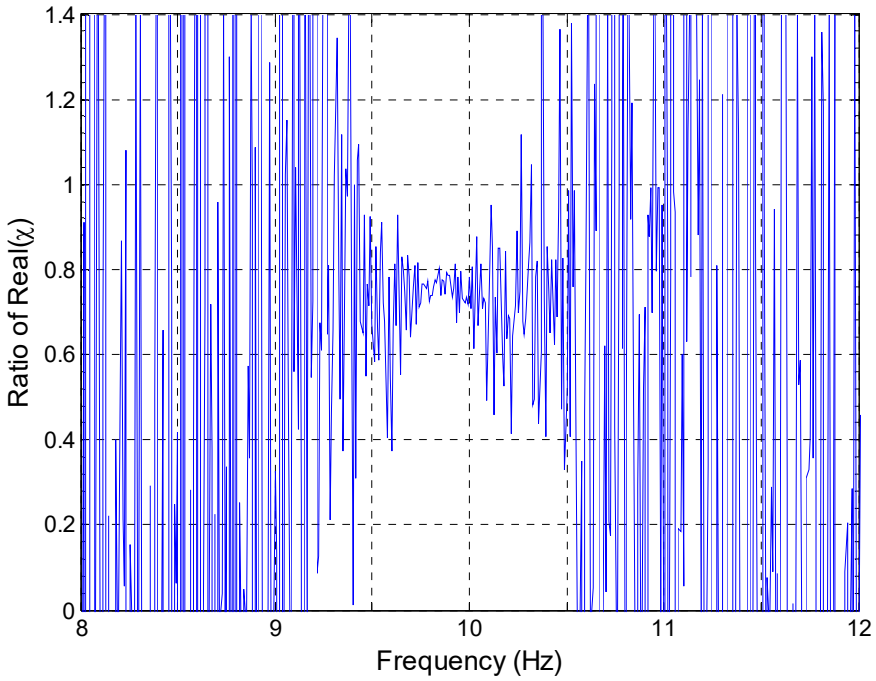

Figure 6.2-12. Ratio of real part coherence

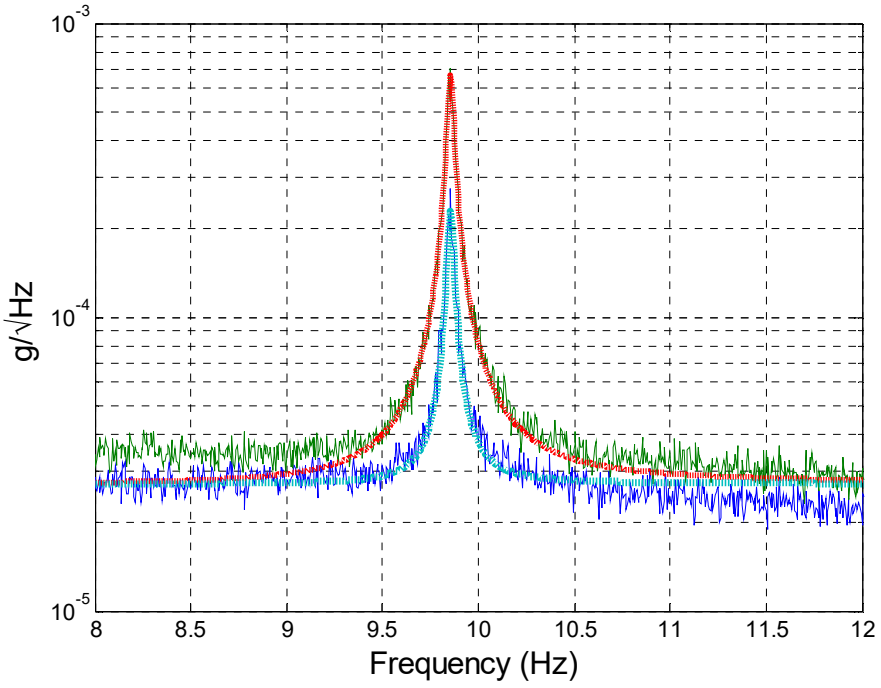

Figure 6.2-13. Root SV spectrum of asynchronous data set (solid line: singular values based on sample PSD; dashed line: theoretical values)

Using the estimated coherence value and the identified modal parameters, the theoretical eigenvalues of the PSD matrix for asynchronous data are calculated based on Eq.(26). The results are plotted with the singular values estimated based on the sample PSD matrix in *Figure 6.2-13*. It can be seen that these two values almost coincide, demonstrating the applicability of the asynchronous model to real data. Multiple trails have also been conducted, showing qualitatively the same results.

6.2.2 Laboratory shear frame model

The laboratory data example presented in this section investigates the applicability of Bayesian methods proposed in this thesis to real asynchronous data while still under well controlled environment. It is the same set of data used in Section 2.2 when investigating the effect of time synchronisation problems on OMA results. The instrumented structure and test configurations are reviewed here. The instrumented structure is a four-storey laboratory shear building model measuring $30\text{cm} \times 20\text{cm}$ in plan with a uniform storey height of 25cm (as shown in *Figure 6.2-14*). *Figure 6.2-15* shows the setup of this example. Six piezoelectric accelerometers are distributed at the centre the floors measuring the vibration response of the structure in the weak direction. Sensor 1 to 4 are connected to one DAQ unit which measure the data synchronously. Sensor 5 and 6 are synchronised using another DAQ unit. Data recording of these two DAQ units is set to start and finish at the same time with the same sampling rate. Thirty minutes of ambient data were recorded with a sampling rate of 2048Hz (later decimated to 256Hz for analysis). The data from Sensor 1 to 4 are combined and referred as the synchronous data set while the data from sensor 1,2,5,6 are combined and referred as the asynchronous data set. For synchronous data, modal identification has been conducted using the fast Bayesian FFT method [79,80]. The proposed Bayesian methods based on both zero coherence

assumption and general coherence assumption are applied to modal identification of the asynchronous data set, where the identification results are compared with those identified based on the synchronous data set.

Figure 6.2-14. Laboratory shear frame model

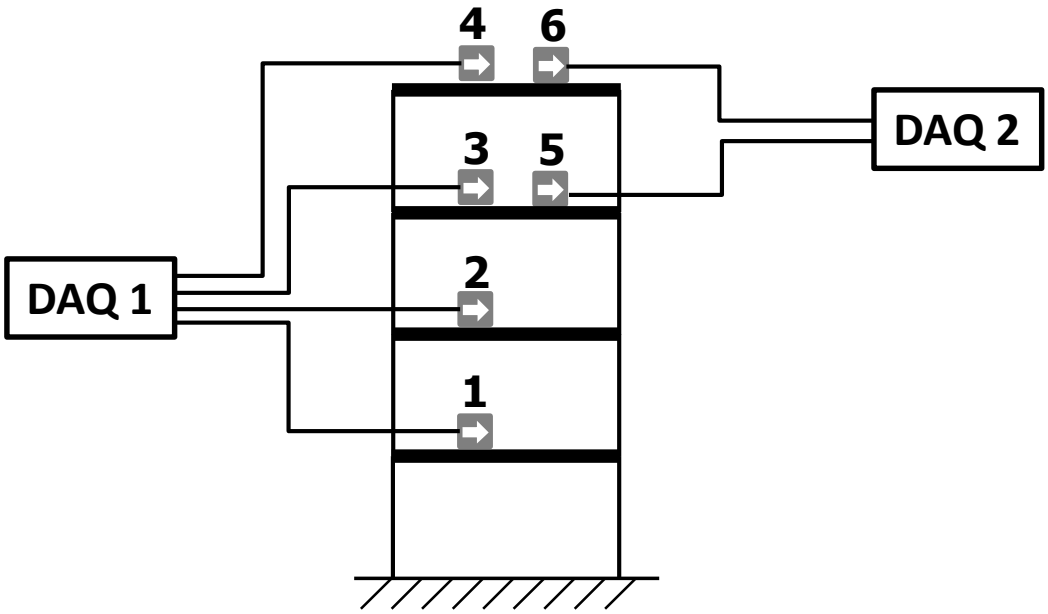

Figure 6.2-15. Experimental setup, laboratory shear frame model

Figure 6.2-16 shows the root SV spectrum of the asynchronous data set. The first five modes of the structure indicated in the figure are identified in this example.

Additional peaks can be found for these modes in the spectrum, reflecting the asynchronisation issue among the data channels. The number of peaks for each mode (i.e., 2) is also consistent with the fact that there are two synchronous data groups. The symbols '[-]' and 'o' in the spectrum represent the selected frequency bands and initial guess of natural frequencies for modal identification. The MPVs of the modal parameters determined for both data sets are listed in *Table 6.2-10*. It can be seen that the values identified based on the asynchronous data set are quite close to their synchronous counterparts for both methods. *Figure 6.2-17* and *Figure 6.2-18* plot the mode shapes identified by these two methods respectively, where the solid line denotes the one for the synchronous data set and the square represents the one for the asynchronous data set. Using the mode shape MPVs based on the synchronous data set as a reference, *Table 6.2-11* shows the MAC values for the mode shapes identified based on the two proposed methods for asynchronous data. The values are extremely close to 1, suggesting good identification quality of mode shapes. The above analysis shows that the proposed Bayesian methods with zero coherence and general coherence assumptions can both provide precise estimations of modal parameters for real asynchronous data. Compared to the zero coherence method, the general coherence method can also quantify the coherence values among the synchronous data groups.

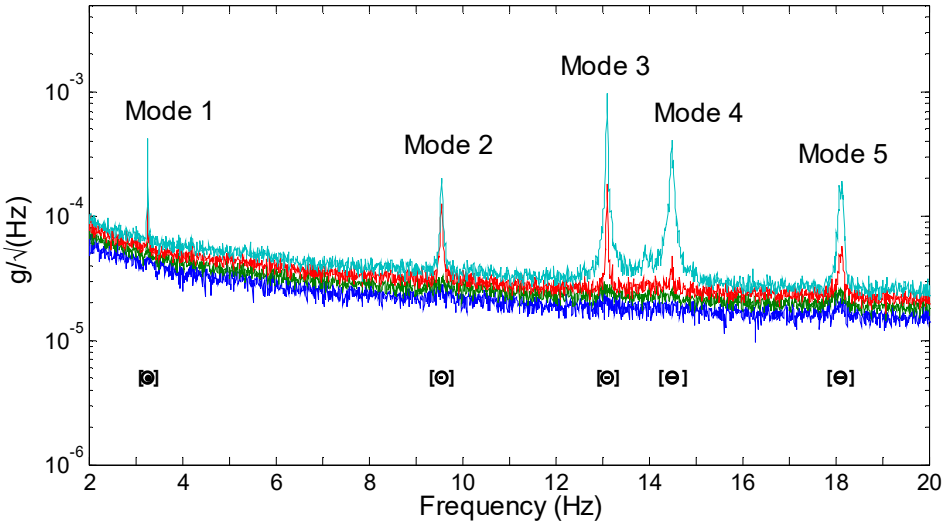

Figure 6.2-16. Root SV spectrum of asynchronous data set, laboratory shear frame model

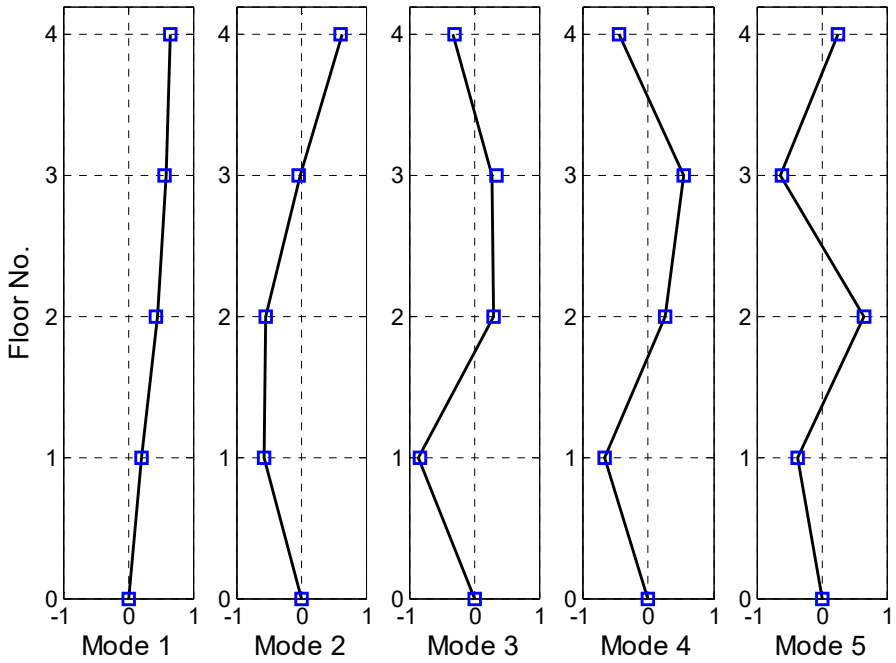

Figure 6.2-17. Identified mode shapes (solid line: synchronous data, squares: asynchronous data based on zero coherence method)

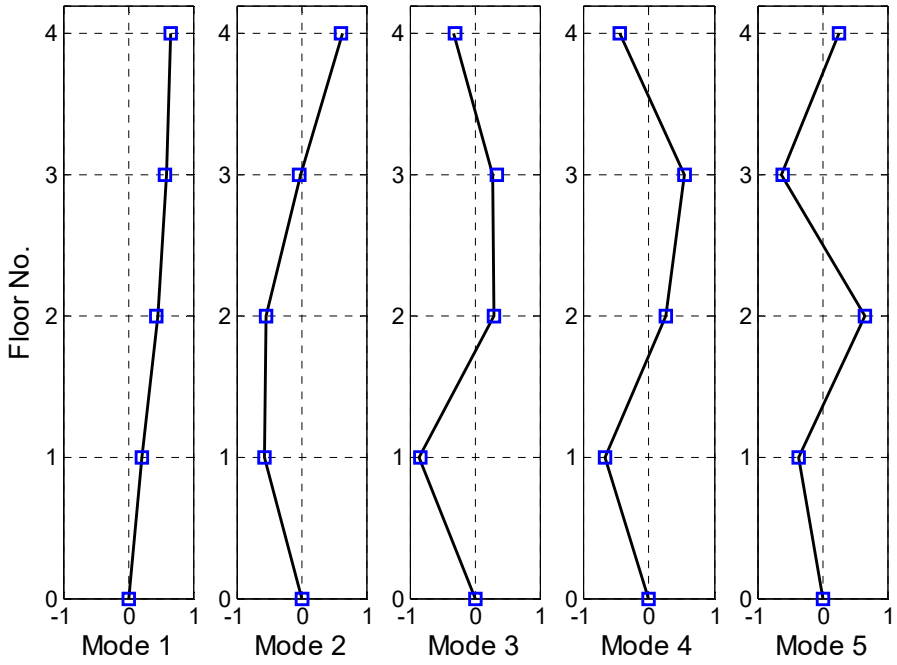

Figure 6.2-18. Identified mode shapes (solid line: synchronous data, squares: asynchronous data based on general coherence method)

Table 6.2-10 Identified modal parameters (MPVs), laboratory shear frame model

Modal Parameters		Mode				
		1	2	3	4	5
f(Hz)	Syn.	3.260	9.559	13.108	14.496	18.128
	Asyn. (Zero Coh.)	3.260	9.560	13.108	14.496	18.128
	Asyn. (Gen. Coh.)	3.260	9.560	13.108	14.496	18.128
$\zeta(\%)$	Syn.	0.07	0.15	0.04	0.15	0.22
	Asyn. (Zero Coh.)	0.08	0.15	0.04	0.15	0.23
	Asyn. (Gen. Coh.)	0.08	0.14	0.04	0.15	0.22
$\sqrt{S}\left(\mu g/\sqrt{Hz}\right)$	Syn.	0.89	0.76	1.03	1.21	0.83

	Asyn. (Zero Coh.)	0.97	0.74	1.05	1.21	0.83
	Asyn. (Gen. Coh.)	0.97	0.73	1.05	1.21	0.82
$\sqrt{S_e}\left(\mu g/\sqrt{Hz}\right)$	Syn.	54.1	28.1	25.1	23.5	22.0
	Asyn.	54.1	28.9	22.9	20.5	22.7
	(Zero Coh.)	50.1	27.8	23.8	22.9	21.1
	Asyn. (Gen. Coh.)	52.3	28.3	23.4	21.8	22.0
χ	Asyn. (Gen. Coh.)	0.77-0.63i	0.37+0.93i	0.90+0.45i	0.98+0.17i	0.85-0.52i

Table 6.2-11 Mode shape MAC values, Laboratory Shear Frame Model

		Mode				
		1	2	3	4	5
MAC Values	Asyn. (Zero Coh.)	0.9995	0.9998	0.9975	0.9998	0.9999
	Asyn. (Gen. Coh.)	0.9998	0.9999	0.9974	0.9999	0.9999

The identification uncertainty obtained based on the Bayesian method with zero coherence assumption is also investigated in this example. Theoretically, the posterior uncertainty of these two data sets cannot be directly compared as they are obtained based on different measured data. Considering the fact that the data from these two sets is measured based on the same experimental condition (i.e., the same duration, excitation and sensor specification), the posterior uncertainty for the asynchronous data set should be intuitively larger than that of the synchronous one. *Table 6.2-12* shows posterior c.o.v.s of the identified modal parameters for both the synchronous and asynchronous data sets. It can be seen that this is not the case with

the results in the table, however. The posterior c.o.v.s of the natural frequency, damping ratio and modal force PSD for the asynchronous data are generally less than the synchronous counterparts, which are in the order of 20% lower. This is attributed to the under-estimation nature of the proposed method due to the zero coherence approximation as illustrated in the bias estimation example (see Section 6.1.2). Further analysis reveals that the coherence between the synchronous data groups is about 0.9, which is relatively high. Referring to the results in bias estimation example, such bias is reasonable.

Table 6.2-12 Identification uncertainty, laboratory shear frame model

Mode	f c.o.v. (10^{-3})		ζ c.o.v. (%)		$\sqrt{S}$ c.o.v. (%)		$\sqrt{S_{ej}}$ c.o.v. (%)	
	Asyn.	Syn.	Asyn.	Syn.	Asyn.	Syn.	Asyn.	Syn.
1	0.13	0.17	21.5	29.3	10.4	12.7	8.10 8.22	4.74
2	0.11	0.16	9.91	13.3	5.11	6.67	3.71 3.70	2.15
3	0.04	0.06	10.9	15.4	3.55	4.47	3.71 3.70	2.15
4	0.08	0.11	6.65	7.78	2.83	3.89	2.63 2.63	1.52
5	0.11	0.16	7.08	9.66	4.21	5.60	2.61 2.62	1.52

The posterior uncertainty of the prediction error for the asynchronous data set is larger than those for the synchronous data set. This is because the prediction error PSD for the asynchronous data is assumed to be the same within each synchronous group and identified based on the data channels within the group individually. For the synchronous data set, the prediction error PSD is assumed to be the same among

all the data channels and hence more data are involved for inference. However, more modelling error may be involved since the prediction error PSD need not be the same among the channels.

6.3 Full-scale test example

The proposed methods are applied to modal identification of field test data measured in an asynchronous manner. The instrumented structure is the Brodie Tower (as shown in *Figure 6.3-19*) at the University of Liverpool, UK. It is a reinforced concrete building with eight storeys and a total height of approximately 25m. The ground floor is connected to another building on the Liverpool campus (i.e., Muspratt Building, see *Figure 6.3-19*) with a rectangular shape. The remaining floors are T-shaped spanning over a $25\text{m} \times 28\text{m}$ area.

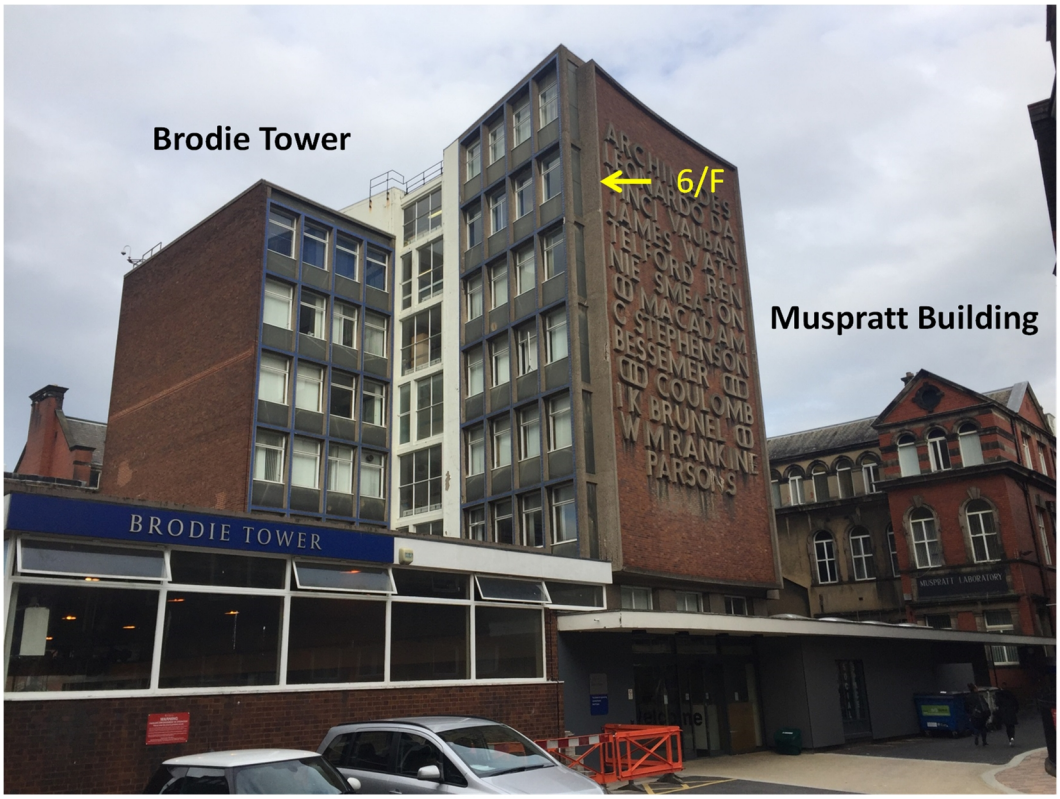

Figure 6.3-19. Brodie Tower

Four forced-balanced triaxial accelerometers (Guralp CMD-5TCDE) are distributed on the sixth floor of the building measuring the structural responses under ambient excitation condition. The test focuses on the lateral modes of the building and biaxial acceleration are used for analysis, giving $2 \times 4 = 8$ measured DOFs. *Figure 6.3-20* shows the plan view of the building with sensor location and measured DOFs. Both asynchronous and synchronous data sets are measured in this test. For each data set, twenty minutes of ambient data are measured with a sampling rate of 50Hz. The sampling clocks in the sensors first run independently without synchronisation to obtain the asynchronous data set. They are then synchronised using GPS to obtain the synchronous data set.

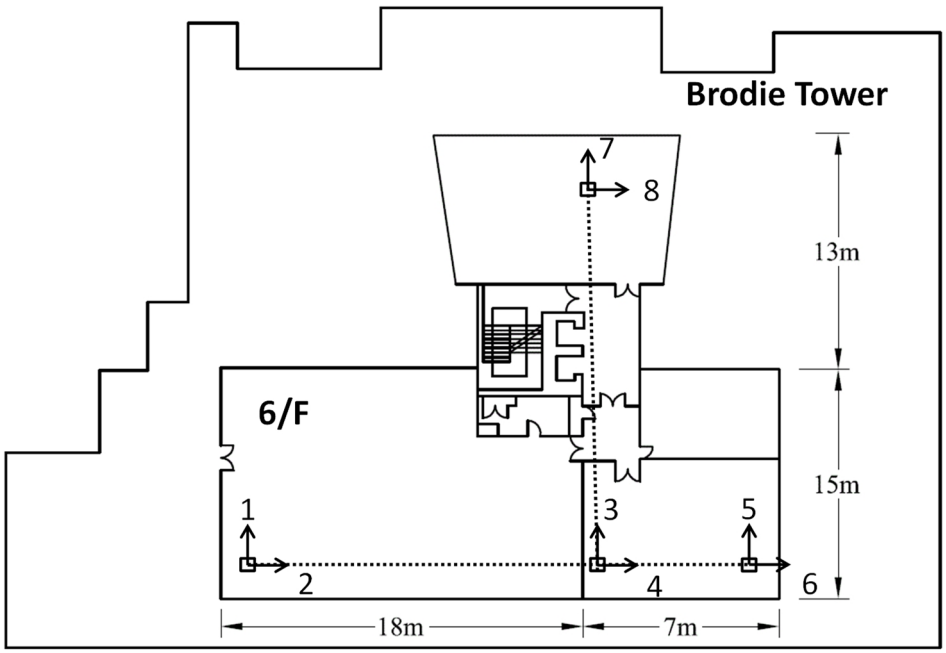

Figure 6.3-20. Plan view of Brodie Tower with sensor locations

Figure 6.3-21 and *Figure 6.3-22* show the root SV spectrum of the synchronous and asynchronous data sets, respectively. Modal identification focuses on the first six modes marked in the figure. The initial guesses of natural frequencies and selected

frequency bands are also indicated as '[-]' and 'o' in the figures, respectively. For the synchronous data set, only one significant peak can be found for each mode. This is not the case for the asynchronous data set. Multiple peaks can be found for each mode, reflecting the asynchronisation issue among the data channels. It can be seen than the first two modes are close to each other with some overlapping of modal contributions. Since the proposed method assumes single mode in the selected frequency band, narrower bands have to be used for these two modes where only the mode of interest is dominant in each band. Modal identification for asynchronous data has been conducted using the Bayesian methods proposed in this work with zero coherence assumption and general coherence assumption, respectively. The modal parameters for synchronous data are identified using the Bayesian FFT method that assumes synchronous data [79,80]. The identification results are summarised in *Table 6.3-13*. For asynchronous data, the identified modal parameters based on these two proposed methods are quite close to their synchronous counterparts. Small discrepancies can be found. This is reasonable and can be attributed to the environmental variation since these two data sets were recorded at different time. The identification uncertainties of the modal parameters for the synchronous data set and asynchronous data set based on the zero coherence method are listed in *Table 6.3-14*. It can be seen that the posterior c.o.v. of the damping ratio for the first two modes are relatively high compared to other modes. This is mainly due to the narrow band where the number of FFT data used for inference is limited.

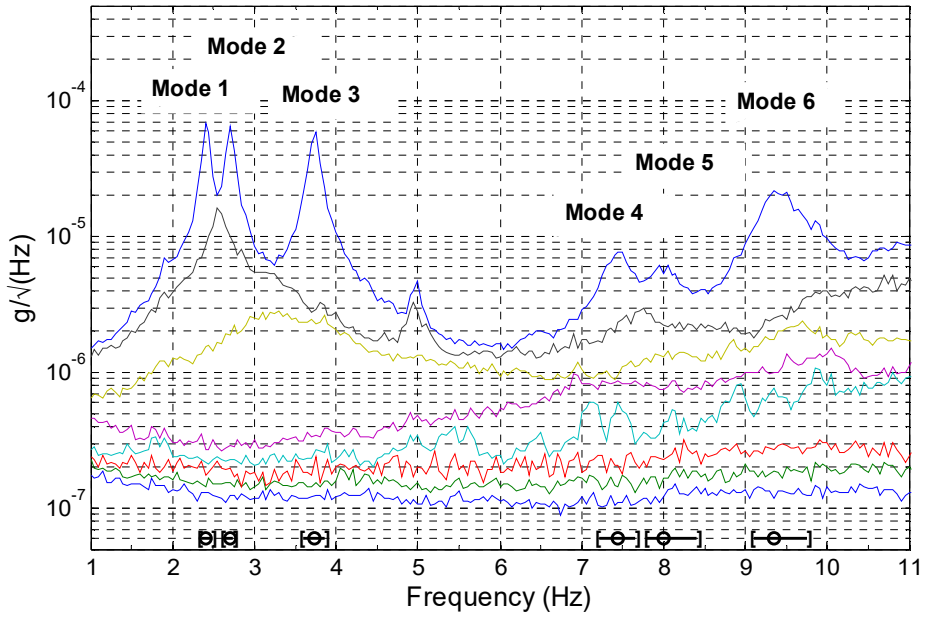

Figure 6.3-21. Root SV spectrum of synchronous data set, Brodie Tower

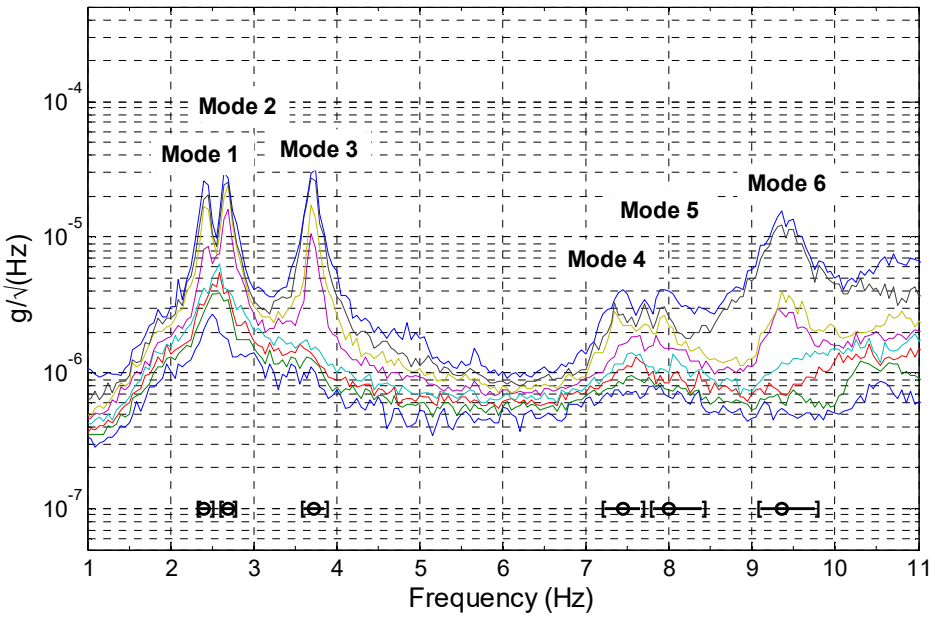

Figure 6.3-22. Root SV spectrum of asynchronous data set, Brodie Tower

Table 6.3-13 Identified modal parameters (MPVs), Brodie Tower

Modal parameters		Mode					
		1	2	3	4	5	6
$f\,(\mathrm{Hz})$	Syn.	2.428	2.698	3.751	7.379	7.983	9.441
	Asyn. (Zero Coh.)	2.418	2.678	3.714	7.419	7.932	9.391
	Asyn. (Gen. Coh.)	2.417	2.679	3.714	7.420	7.932	9.390
$\zeta(\%)$	Syn.	1.14	0.94	0.78	2.43	3.20	2.33
	Asyn. (Zero Coh.)	1.32	1.08	0.90	2.21	2.41	1.97
	Asyn. (Gen. Coh.)	1.18	1.16	0.89	2.20	2.16	1.95
$\sqrt{S}\left(\mu g/\sqrt{\mathrm{Hz}}\right)$	Syn.	1.10	1.01	0.80	0.22	0.32	0.80
	Asyn. (Zero Coh.)	1.28	1.32	1.05	0.24	0.27	0.77
	Asyn. (Gen. Coh.)	1.20	1.37	1.05	0.24	0.25	0.77
$\sqrt{S_e}\left(\mu g/\sqrt{\mathrm{Hz}}\right)$	Syn.	1.94	2.28	1.07	0.96	0.88	1.01
	Asyn. (Zero Coh.)	3.04	3.27	1.49	1.10	1.07	0.96
	Asyn. (Gen. Coh.)	3.04	3.27	1.49	1.10	1.09	0.96

Figure 6.3-23 to *Figure 6.3-25* plot the identified mode shapes for the synchronous and asynchronous (based on the two proposed methods) data sets, respectively. The squares represent the measured locations. The undeformed and deformed mode shapes are shown as dashed and solid lines, respectively. Mode 1 and Mode 4 are translational modes dominated in x-direction with small rotations which may be due to the shape of the floor and the mass distribution. Mode 2 is also a translational mode but dominated in y-direction. Mode 3, 5 and 6 are rotational modes while Mode 5 and 6 also involves deformation of the T-shaped floor plan. Using the mode shape MPVs determined based on the synchronous data set for reference,

Table 6.3-15 lists the MAC values for the identified mode shapes based on the zero coherence and general coherence methods, respectively. It can be seen that the identified mode shapes using the proposed methods based on asynchronous data

agree well with those based on the synchronous data. The MAC values are extremely close to 1, suggesting good identification quality of mode shapes based on these two methods.

Table 6.3-14 Identification uncertainty, Brodie Tower

Mode	f c.o.v. (%)		ζ c.o.v. (%)		$\sqrt{S}$ c.o.v. (%)		$\sqrt{S_{ej}}$ c.o.v. (%)	
	Asyn.	Syn.	Asyn.	Syn.	Asyn.	Syn.	Asyn.	Syn.
1	0.07	0.13	8.4	15	5.4	9.2	4.2	1.6
2	0.06	0.11	8.5	16	5.4	9.6	4.3	1.6
3	0.04	0.06	5.0	9.9	2.5	4.3	2.9	1.1
4	0.08	0.17	7.3	12	5.6	9.3	2.2	0.8
5	0.12	0.22	5.8	10	4.5	8.1	1.7	0.7
6	0.05	0.10	3.8	7.9	2.6	5.5	1.8	0.7

Table 6.3-15 Mode shape MAC values, Brodie Tower

		Mode					
		1	2	3	4	5	6
MAC	Asyn. (Zero Coh.)	0.9994	0.9995	0.9994	0.9373	0.9794	0.9988
Values	Asyn. (Gen. Coh.)	0.9994	0.9995	0.9993	0.9345	0.9817	0.9988

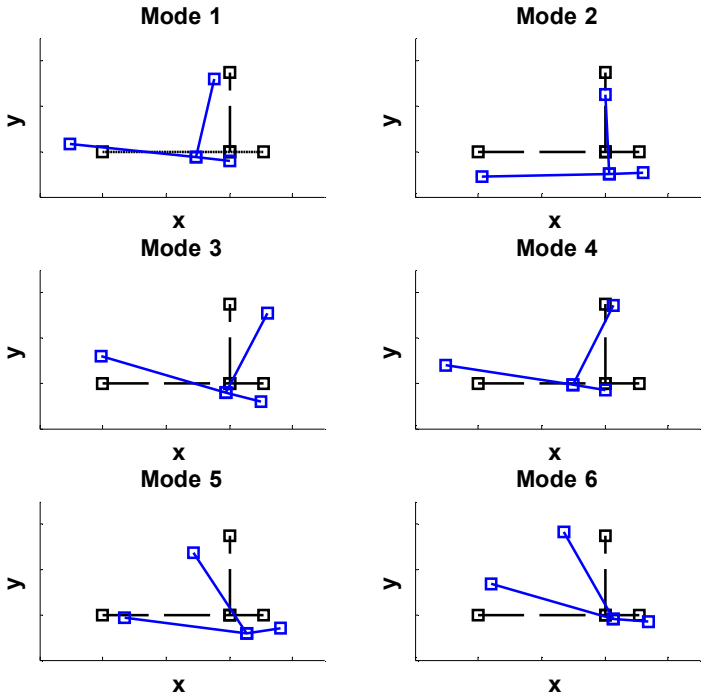

Figure 6.3-23. Mode shape MPVs of synchronous data, Brodie Tower

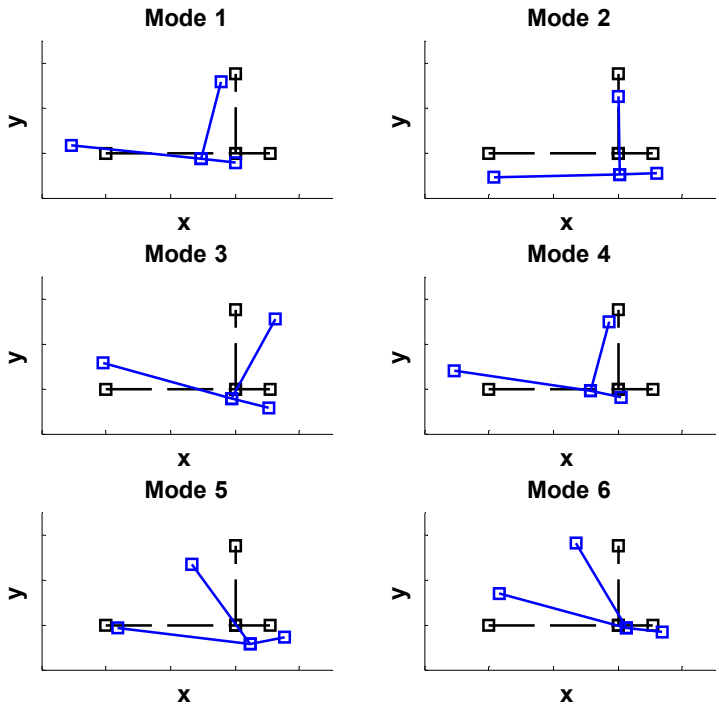

Figure 6.3-24. Mode shape MPVs of asynchronous data (Zero Coh.), Brodie Tower

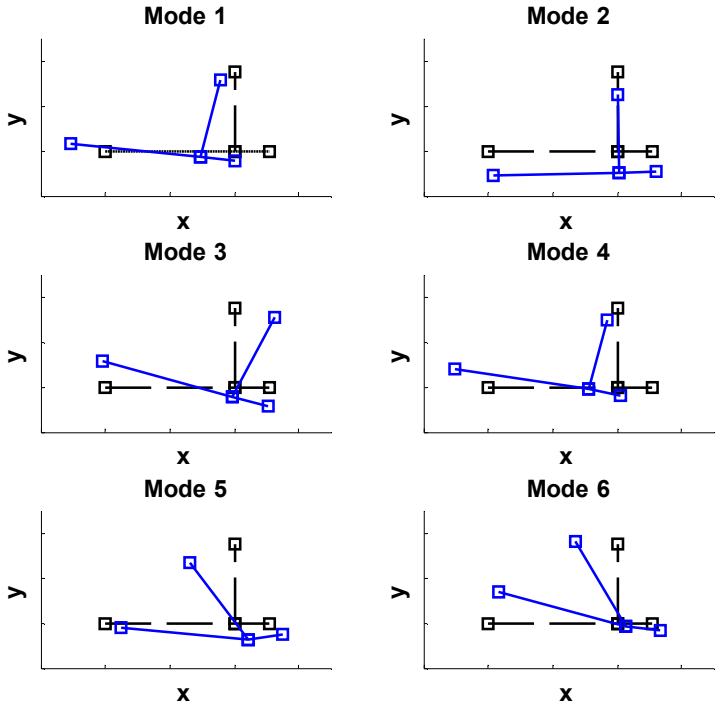

Figure 6.3-25. Mode shape MPVs of asynchronous data (Gen. Coh.), Brodie Tower

Compared to the asynchronous data, additional effort on synchronisation is needed in order to get synchronous data, especially for field tests. In this example, it takes about thirty minutes to synchronise all the sensors with the GPS. For asynchronous data, such configuration time can be saved and the field test can also be more flexibly and efficiently conducted. The computational time for determining the MPVs of modal parameters in this test is listed in *Table 6.3-16*. The modal analysis is conducted using MATLAB R2014a on an HP Compaq 800 G1 Elite Desktop (Intel Core i5, 2GHz and 8GB of RAM). The convergence tolerance is set as 10^{-6} on a fractional basis for all parameters. Generally, it takes more time to identify the modal parameters based on the asynchronous data set. It is especially so for the general coherence method. This is reasonable as it still involves matrix computation

with dimension equals to the number of synchronous data groups (which is four in this example). Nevertheless, the general coherence method provides a rigorous means to determining the MPVs of modal parameters where the asynchronous model is strictly obeyed. It can also investigate the time synchronisation degrees among different synchronisation data groups quantitatively by identifying the coherence values among the groups. The computational process can be done in the order of minutes for the proposed method, which is still acceptable even for on-site implementation.

Table 6.3-16 Computational time, Brodie Tower

		Mode					
		1	2	3	4	5	6
Computational Time (s)	Syn.	1.2	1.0	0.9	3.5	4.1	2.8
	Asyn. (Zero Coh.)	3.4	3.2	3.4	26.6	31.8	27.7
	Asyn. (Gen. Coh.)	384.8	303.1	181.2	445.9	377.9	468.9

6.4 Discussion

Synthetic, laboratory and field test examples have been presented in this chapter to verify the consistency of the proposed asynchronous data model and two Bayesian OMA methods. It is shown that the eigenvalues and eigenvectors of the PSD matrix estimated based on the proposed asynchronous data model fit well with the ones based on both the synthetic and laboratory data. The proposed Bayesian OMA methods have also been verified using synthetic data, where the identified modal parameters are consistent with the exact ones that generate the data. For laboratory and field test examples, the identified modal parameters based on these two methods are compared with the ones identified based on synchronous data, where they almost coincide. The modelling error due to zero coherence approximation has also been

investigated through a parametric study. It is shown that such modelling error does not cause bias in the MPV of modal parameters, but leads to under-estimation in the posterior uncertainty. Nevertheless, such effect is not significant unless the actual coherence among the synchronous data groups in the measured data is extremely high. In the case of field application, more investigation is needed. The next chapter focuses on the OMA of a full-scale building with multiple setups, where the OMA results based on asynchronous ambient data and the associated practical issues are discussed.

Chapter 7: Field Application

In this chapter, ambient modal identification of an eight-storey concrete building is presented. The structural responses of the building on all the floors are measured through multiple setups and both synchronous and asynchronous data are measured for modal analysis. The proposed Bayesian zero coherence method for asynchronous data and the Bayesian FFT method for synchronous data are applied to modal analysis of each setup individually. The global mode shape of the building is assembled from the most probable local mode shapes in individual setups based on the global least square method. The modal identification results based on the asynchronous data are compared against their synchronous counterparts. In addition to the MPV, the identification uncertainties are also discussed. This chapter investigates the modal identification quality of the proposed method incorporating multiple setups based on a full-scale ambient test, where the complication and practical aspects in field implementation are naturally reflected in the measured data. Detailed instrumentation, logistic and time synchronisation issues are also discussed in this chapter, which provides more insights in conducting full-scale ambient vibration tests based on asynchronous data.

7.1 Description of the structure

The instrumented structure in this test is Brodie Tower, an eight-storey office building on the campus of the University of Liverpool. It is the same structure described in the field test verification example in Section 6.3. In this test, the structure responses of the building on all the floors are measured, which intends to identify the overall response pattern of the building. The building is ‘T-shaped’,

which is of interest to investigate the dynamic properties of the building. Triaxial sensors are used to capture the modal modes of the building in all three directions.

7.2 Instrumentation

Portable data logging units are used in this test for mobile field deployments. The equipments are hosted in a water-proof rugged case for each unit, which comprises accelerometer, GPS receiver, high-precision clock, battery and accessories (e.g., cables). *Figure 7.2-1* shows a typical set of the unit at one measurement location. Five sets of such data acquisition units are deployed to measure the ambient vibration of the structure. The on-site view of the measurement units are shown in *Figure 7.2-2*.

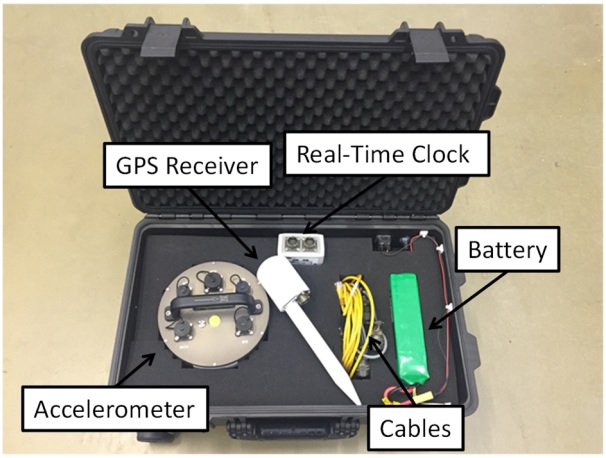

Figure 7.2-1. A set of equipment for data measurement

Figure 7.2-2. On-site view of data measurement units

7.2.1 Sensor performance

Five triaxial force-balanced accelerometers (Guralp CMG-5TCDE) are used in this test for vibration data measurement. Despite the accelerometer itself, it is also embedded with a 24bit digitiser, an on-board Flash memory storage and a web-based user interface. The accelerometer has a maximum measurement range of $\pm 2g$. A 'huddle test' [119] has been conducted to evaluate the noise level of the sensor. *Figure 7.2-3* shows the noise spectrum of a typical accelerometer used in this test based on a four hour measurement. There is an increase of the noise level at low frequencies, which is the typical situation for all types of accelerometers. The noise level is in the order of $0.1\mu g/\sqrt{Hz}$ for the frequency larger than 1Hz, which is sufficient for full-scale ambient vibration test.

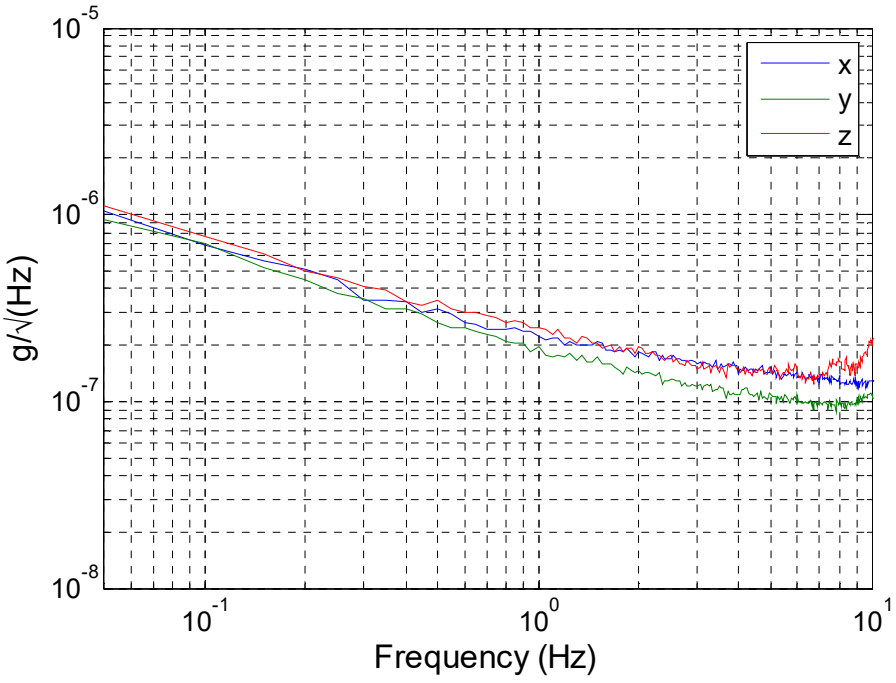

Figure 7.2-3. Noise spectrum of the sensor

7.2.2 Sensor location

Based on the floor plan of the building, it is intended to obtain a mode shape with the 'T-shape'. *Figure 7.2-4* shows the plan view of the building with measured DOFs. Compromising the available number of sensors, four locations on each floor from 1/F to 7/F are measured with one reference location on 7/F for mode shape assembling. The total number of measured DOFs is given by $(4\times 7+1)\times 3=87$. Considering feasibility and convenience of logistic and sensor deployment, the sensors are placed in the corridors and aligned along the frame direction of the building.

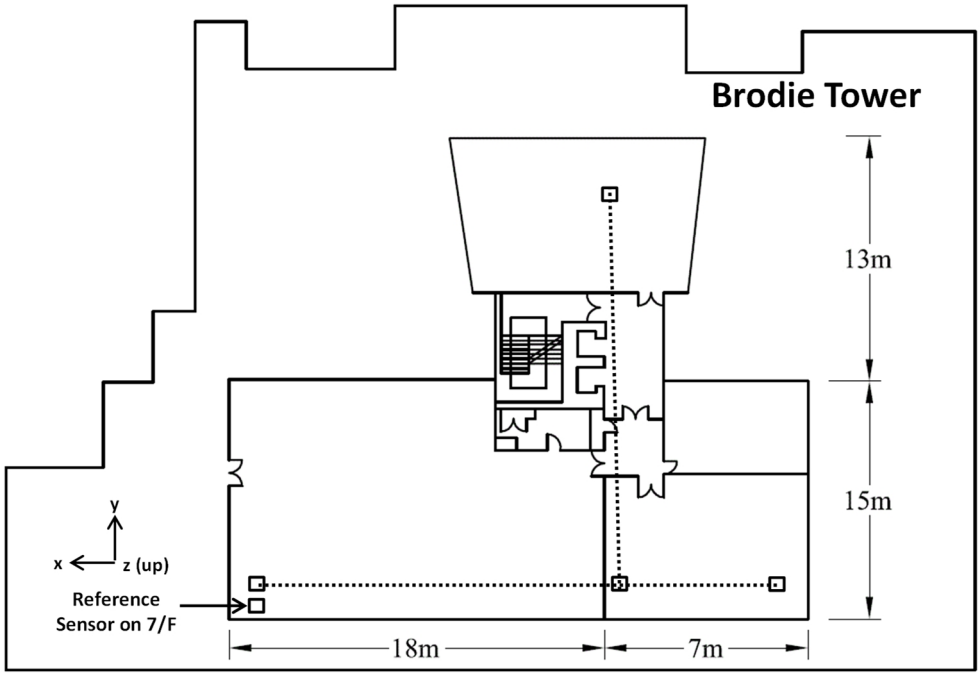

Figure 7.2-4. Plan view of the structure with sensor locations and measured directions

7.2.3 Reference sensor

Due to the limited number of sensors, the DOFs of interest cannot be measured in a single setup. One feasible way is to conduct multiple setups to cover all the

measurement locations. The mode shape values identified in different setups have different scaling so it is necessary to have reference DOFs among the setups for mode shape assembling. The mode shape values at the reference DOFs should be significant for all the modes of interest in order to reduce the errors in the assembling procedure. In this test, one reference location is chosen on the top floor of the building (i.e., 7/F) near the lower left corner (see *Figure 7.2-4*), which is expected to have significant structural responses and unlikely to be at a node of the modes.

7.2.4 Roving setups

Except for the reference sensor, the remaining sensors are roved to different floors in different setups. The DOFs of interest on one floor are measured in a single setup, giving seven setups in total for the test. To investigate the modal identification quality based on asynchronous ambient data, it would be ideal if both synchronous and asynchronous data are measured during exactly the same time period. Unfortunately, this is practically not feasible as the number of sensors is limited and it is impossible to place two sensors at exactly the same location. As a compromise, setups for asynchronous data were first conducted, followed by the setups where the sensors were synchronised.

Figure 7.2-5 shows the schematic diagram of the setup plans. For asynchronous data, the setups are conducted in the morning from 8:30 to 12:30 roving from 7/F to 1/F. The order of the setups on 3/F and 2/F is swapped as there was an examination in the lecture room on 3/F. To minimise the effect of vibration test to the examination, the setup on 2/F was conducted first and the one on 3/F was conducted after the examination was finished. After the setups for asynchronous data, the sensors are synchronised using ‘real-time’ clocks (which is discussed in the next section) and

setups were then conducted in the afternoon from 14:30 to 17:10 with the order from 7/F to 1/F.

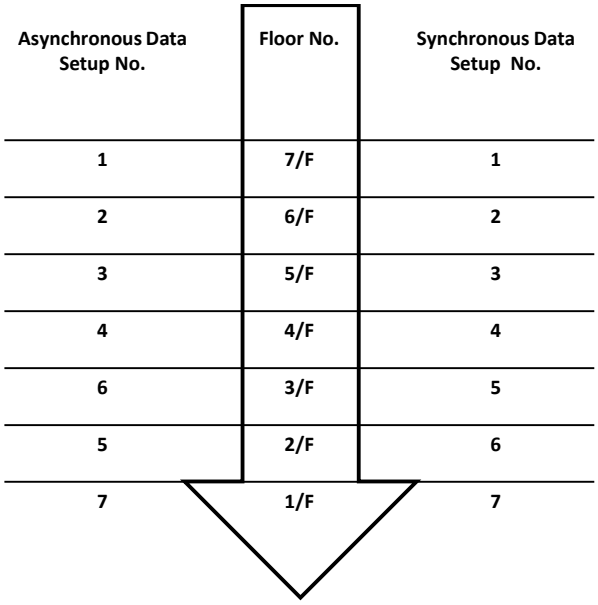

Figure 7.2-5. Schematic diagram of roving setups

Two participants were involved in this test, each responsible for two sensors. Twenty five minutes of data were measured for each setup, allowing five minutes as a buffer. The transition time between setups took about five minutes, including levelling and alignment.

7.2.5 Time synchronisation

In this test, the asynchronous data are simply obtained by running the sampling clocks among the sensors independently without synchronisation. As most of the measurement locations in this test are indoor where the GPS signal is weak, synchronising the sensors using GPS is not feasible. 'Real-time' clocks (Guralp CMG-RTM) were used to synchronise the sensors in this test. They are high-precision clocks which can control the sampling procedure with extremely low time drift after being trained with a common time source. The 'real-time' clocks used in this test were first trained using GPS receivers. Once the clocks were locked, the

GPS receivers were disconnected and the clocks ran as the substitutions of GPS providing high-precision time basis for the sensors. The real-time clocks used in this test have an accuracy of 0.038ppm (parts per million). This corresponds to a relative time drift of $2\times0.038\times10^{-6}\times3600\times12\approx3\text{ms}$ over 12 hours. In the frequency range of interest $\ll1/3\times10^{-3}\approx300\text{Hz}$, the data can be considered as practically synchronised.

7.3 Modal analysis

Modal identification has been conducted and the identified modal parameters as well as the associated uncertainties are investigated in this section. For synchronous data, the MPV of modal parameters and the posterior uncertainties are determined using the Bayesian FFT method [79,80]. For asynchronous data, the proposed Bayesian method with zero coherence assumption is applied to identify modal parameters and quantify uncertainties. Modal identification is conducted within individual setups and the global mode shapes are assembled using the global least-square method [120]. The identification results based on asynchronous data are assessed by comparing with those identified based on synchronous data.

Considering the fact that the setup number for synchronous and asynchronous data may not refer to the same measured DOFs, the results listed in the tables and figures are referred based on the floor number of the measured DOFs for each setup rather than the setup number.

7.3.1 Data spectrum

Figure 7.3-6 and *Figure 7.3-7* show the root SV spectrum of Setup 1 (i.e. 7/F) for synchronous and asynchronous data, respectively, which help locate potential modes and select frequency bands for analysis. The peaks in the spectrum indicate the

presence of potential modes. The selected frequency bands and initial guesses of natural frequencies for modal identification are indicated in the figures with symbol '[-]' and 'o', respectively. For synchronous data, there is only one significant peak within each selected frequency band, indicating only one mode dominated in the band. However, multiple peaks can be found for asynchronous data, which merely reflects the number of synchronous data groups among the measured data.

The first six modes indicated in the spectrum are analysed in this test. These modes are representative in full-scale ambient tests. The spectral peaks of the first three modes are significant, indicating relatively high SNRs. The SNRs for the last three modes are low compared to the first three modes. This is common in full-scale tests when the modes are not well excited or the measurement noise is high. This is especially so for the sixth mode where the SNR is extremely low. *Table 7.3-1* summarises the sample mean of SNR among the setups for both asynchronous and synchronous data calculated based on the identified modal parameters as a reference.

Compared to the spectrum of laboratory data (as presented in previous sections), the SNRs of the modes in this test are much smaller. Besides the MPVs of modal parameters, the associated identification uncertainty shall also be concerned, which will be investigated later in this example.

Table 7.3-1 Sample mean of SNR among setups

		Mode					
		1	2	3	4	5	6
Modal	Asyn.	712	954	5101	36	68	33
SNR	Syn.	1384	1612	3967	32	59	22

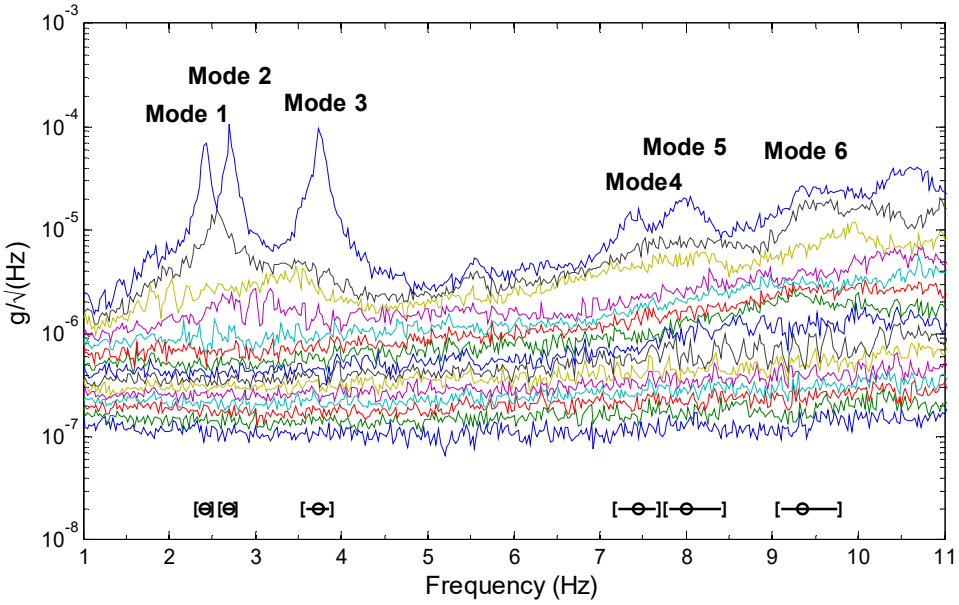

Figure 7.3-6. Root SV spectrum of synchronous data, Setup 1(7/F)

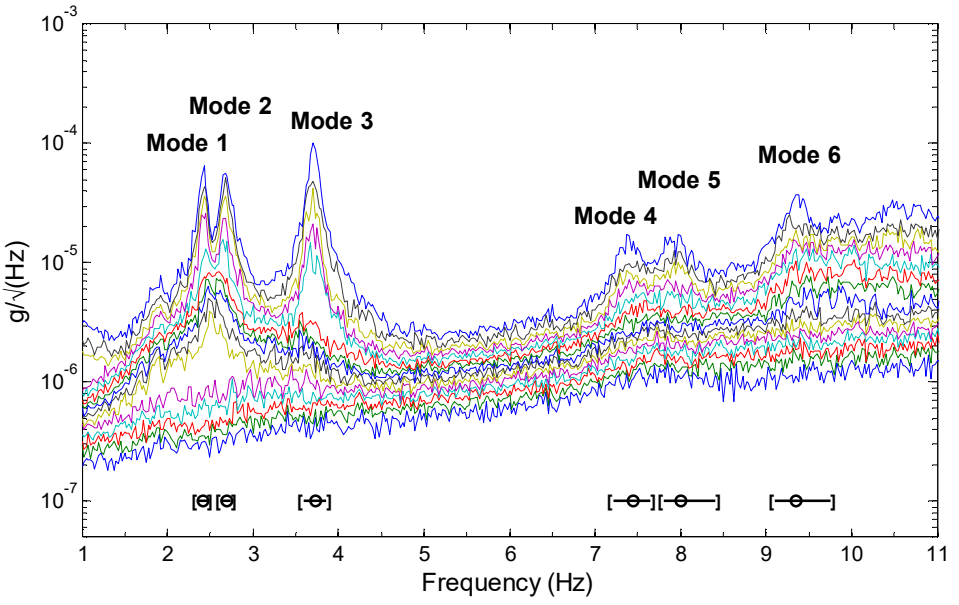

Figure 7.3-7. Root SV spectrum of asynchronous data, Setup 1(7/F)

7.3.2 Identified modal parameters

Figure 7.3-8 and *Figure 7.3-9* plot the MPVs of natural frequency and damping ratio among the setups, respectively. The MPVs based on synchronous data and asynchronous data are shown in the figures with circles and squares, respectively. The error bars represent +/- 2 posterior standard deviation. The identified natural frequencies and damping ratios from the synchronous and asynchronous data generally agree well with each other. Small discrepancies can be found in some setups, e.g., the MPVs of Mode 5 on 5/F. Possible reasons can be the low SNR that affects the identification quality or the environmental variation since the synchronous and asynchronous data were measured over different time periods.

Table 7.3-2 and *Table 7.3-3* summarise the sample mean and c.o.v. of the identified modal parameters among the setups respectively for both asynchronous and synchronous data. It can be seen that the sample mean of identified natural frequencies of the modes based on asynchronous data is very close to the synchronous counterpart. This is also the case for the identified damping ratios. The sample c.o.v.s of the identified damping ratios are larger than those of the identified natural frequencies, which is common in ambient vibration tests. Significant variation lies in the identified modal force PSD although this merely reflects the variation of the environmental conditions during the test.

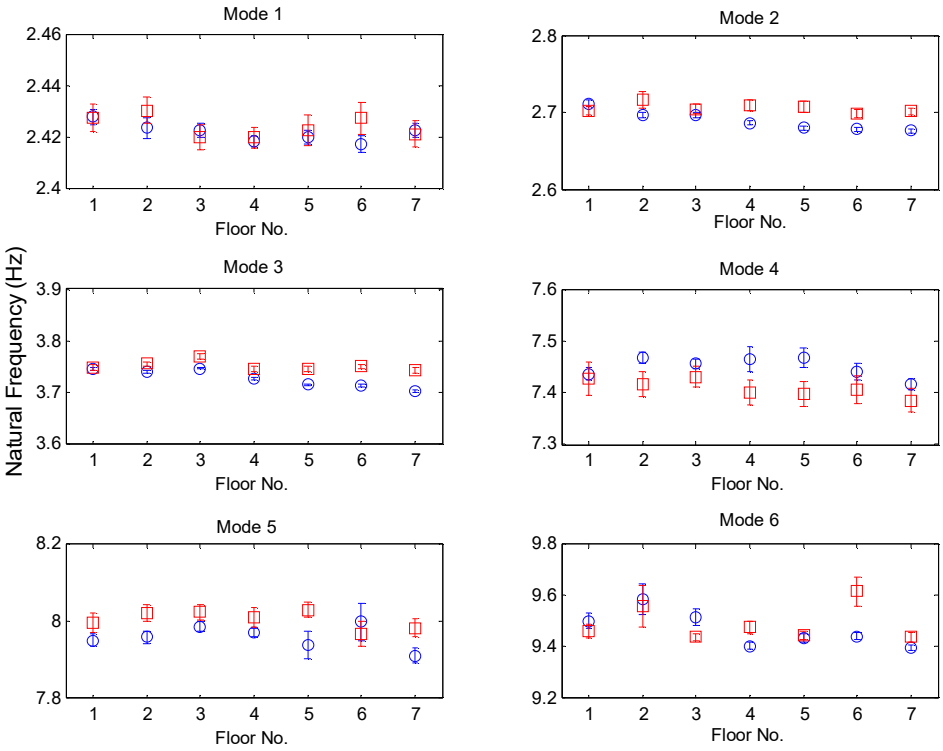

Figure 7.3-8. Identified natural frequencies among setups (circle: asynchronous data; square: synchronous data; error bar: +/-2 posterior standard deviation)

Table 7.3-2 Sample mean of identified modal parameters among setups

		Mode					
		1	2	3	4	5	6
Natural Frequency (Hz)	Asyn.	2.422	2.689	3.728	7.450	7.959	9.469
	Syn.	2.424	2.705	3.752	7.409	8.005	9.492
Damping Ratio (%)	Asyn.	1.24	1.15	0.94	2.72	3.40	3.62
	Syn.	0.99	0.96	0.82	2.69	2.58	2.65
Root Modal Force PSD ($\mu g/\sqrt{Hz}$)	Asyn.	1.40	1.48	1.56	0.84	1.19	1.76
	Syn.	1.07	1.09	1.00	0.58	0.89	1.16

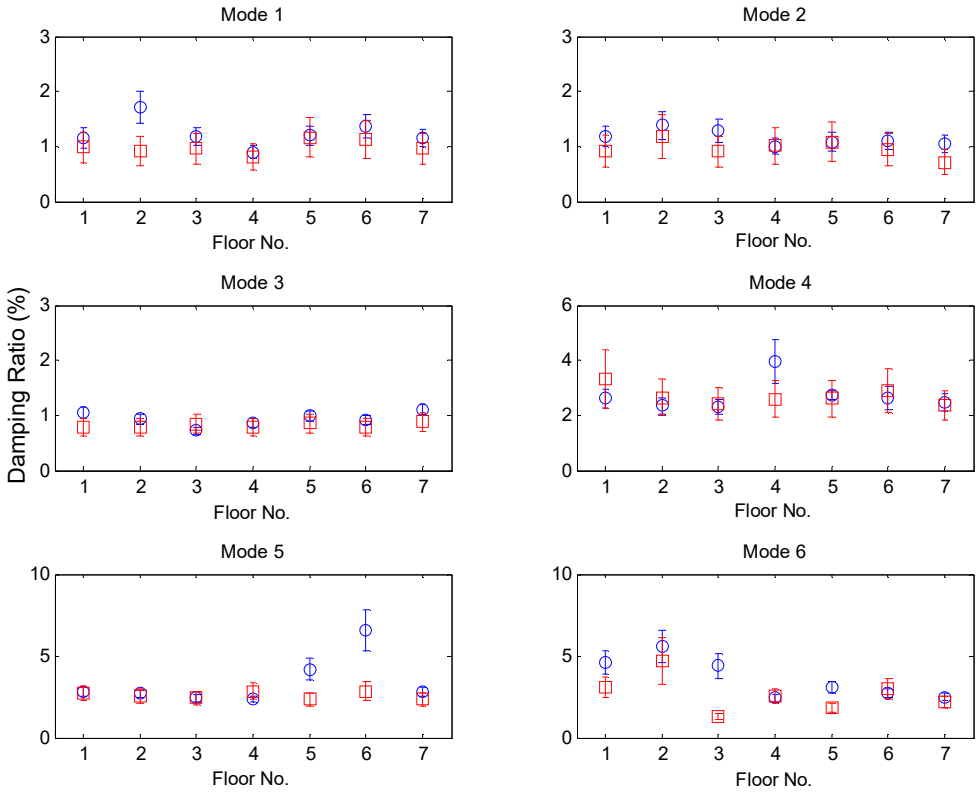

Figure 7.3-9. Identified damping ratios among setups (circle: asynchronous data; square: synchronous data; error bar: +/-2 posterior standard deviation)

Table 7.3-3 Sample c.o.v. (%) of identified modal parameters among setups

		Mode					
		1	2	3	4	5	6
Natural Frequency	Asyn.	0.15	0.48	0.47	0.26	0.37	0.73
	Syn.	0.18	0.23	0.24	0.22	0.29	0.73
Damping Ratio	Asyn.	20	12	14	21	45	34
	Syn.	13	15	5	12	9	41
Root Modal Force PSD	Asyn.	40	28	51	40	18	22
	Syn.	43	33	55	14	27	31

7.3.3 Identified mode shapes

Figure 7.3-10 to *Figure 7.3-15* show the assembled global mode shapes of these six modes based on both synchronous and asynchronous data. The MAC values between the identified mode shapes based on these two types of data for both individual setup and the global assembled cases are listed in *Table 7.3-4*. Mode 1 is a whole building translational mode in the x-direction. Small rotation can be found about the top left corner of the figure in the plan view, which is possibly due to the mass distribution of the whole building. Mode 2 is also a translational mode but in the y-direction without rotation. Mode 3 is a torsional mode with the torsional centre at the left side of the 'T-shape' connection. For the first three modes, the assembled mode shapes based on asynchronous data are very close to the ones based on synchronous data. It can be seen that the MAC values are extremely close to one for these three modes, suggesting good identification quality of the mode shapes based on asynchronous data. Mode 4 is the second translation mode in the x-direction. Similar to Mode 1, small rotation can also be detected in this mode. Mode 5 is the second translation mode in the y-direction. The MAC values of the assembled mode shapes for these two modes between synchronous and asynchronous cases are calculated to be 0.9465 and 0.9813, respectively. The SNRs for these two modes are not high compared to the first three modes. Nevertheless, the identified mode shapes based on asynchronous data for these two modes are physically sound.

Significant discrepancy lies in the identified mode shapes of Mode 6. The MAC value for the assembled overall mode shapes is only 0.02. The MAC values for Mode 6 are not low in individual setups (ranging from 0.65 to 0.91) but the errors are magnified in the assembled global mode shapes. Further analysis reveals that this may be due to the erroneous modelling in the z-direction of the measured data.

Figure 7.3-17 and *Figure 7.3-18* shows the root PSD spectrum based on the data measured by the reference sensor in Setup 2 (i.e., 6/F) for both synchronous and asynchronous data as a typical case. It can be seen that the PSD spectra are not dominated by modal response of Mode 6 in the z-direction for both synchronous and asynchronous data, where spectral peaks cannot be found. Similar situations can be found in the z-direction of other sensors and setups. The mode shape MPVs of Mode 6 in z-direction are erroneously determined. When assembling the global mode shape, such errors are taken into consideration and lead to further estimation errors in the relative scaling of the mode shapes among the setups. In this context, the errors exist in the assembled global mode shapes for both synchronous and asynchronous data.

To investigate whether the vibration data in the z-direction have spurious effects on the identified mode shape of Mode 6. Additional analysis has been conducted excluding the measured data from the z-direction. *Figure 7.3-16* shows the resulting global mode shapes. The assembled global mode shapes between the synchronous and asynchronous data are quite close with a MAC value of 0.978, suggesting that the problem is associated with the modelling error in the z-direction of the measured data.

Table 7.3-4 MAC values of identified mode shapes

Floor No.	Mode					
	1	2	3	4	5	6
1/F	0.9999	0.9999	0.9996	0.9143	0.9949	0.9082
2/F	0.9995	0.9998	0.9979	0.9717	0.9857	0.9112
3/F	0.9993	0.9995	0.9979	0.9775	0.9904	0.6904
4/F	0.9994	0.9993	0.9990	0.9642	0.9936	0.7955

5/F	0.9993	0.9996	0.9988	0.8398	0.8709	0.7941
6/F	0.9995	0.9996	0.9995	0.9410	0.8763	0.6583
7/F	0.9991	0.9997	0.9986	0.9637	0.9904	0.8348
Global	0.9991	0.9994	0.9980	0.9465	0.9813	0.0249

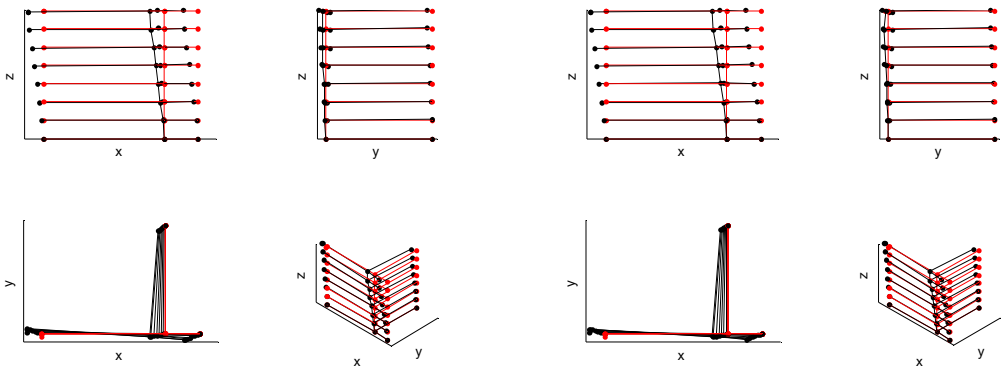

(a) (b)

Figure 7.3-10. Assembled global mode shape of Mode 1 (a) asynchronous data (b) synchronous data

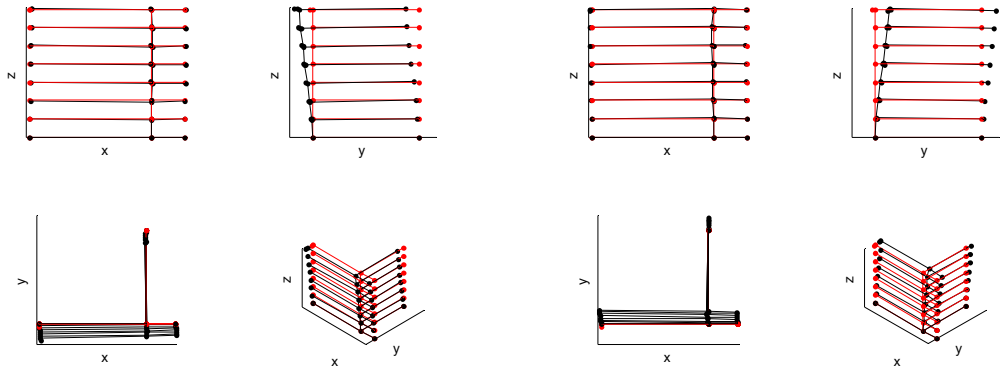

(a) (b)

Figure 7.3-11. Assembled global mode shape of Mode 2 (a) asynchronous data (b) synchronous data

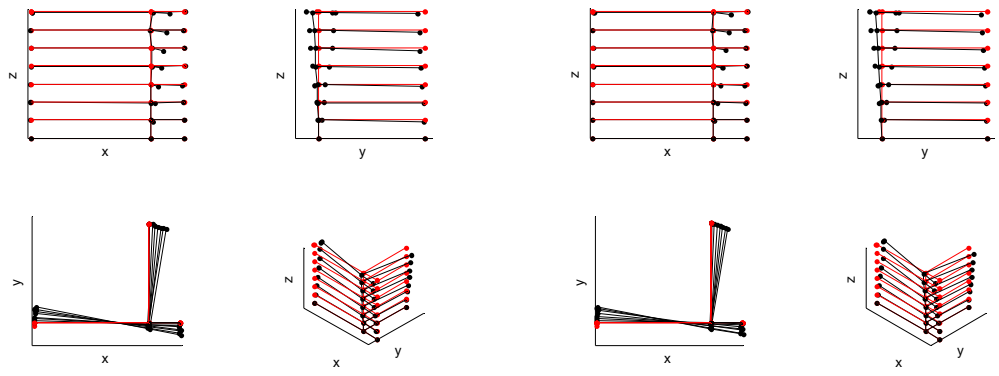

(a) (b)

Figure 7.3-12. Assembled global mode shape of Mode 3 (a) asynchronous data (b) synchronous data

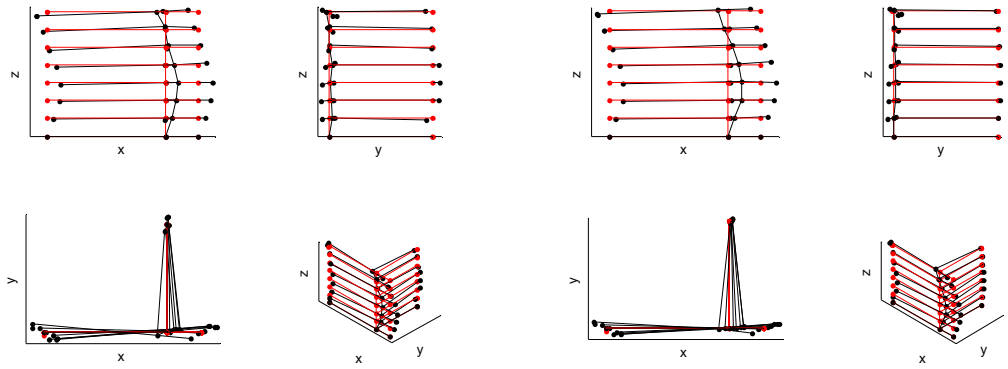

(a) (b)

Figure 7.3-13. Assembled global mode shape of Mode 4 (a) asynchronous data (b) synchronous data

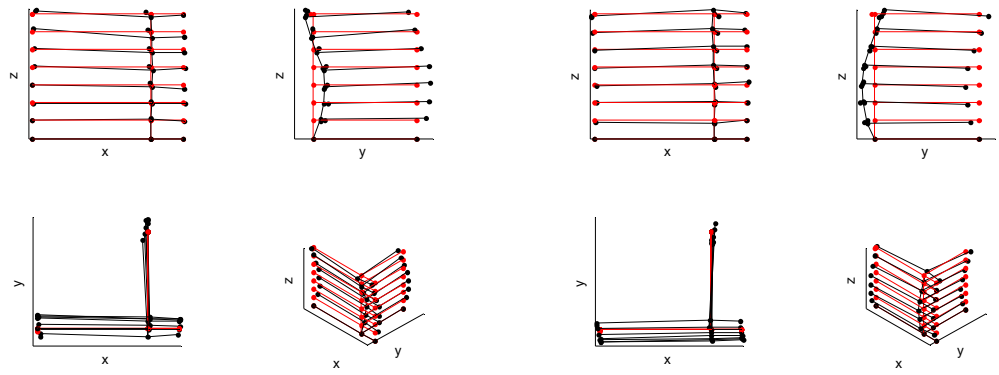

(a) (b)

Figure 7.3-14. Assembled global mode shape of Mode 5 (a) asynchronous data (b) synchronous data

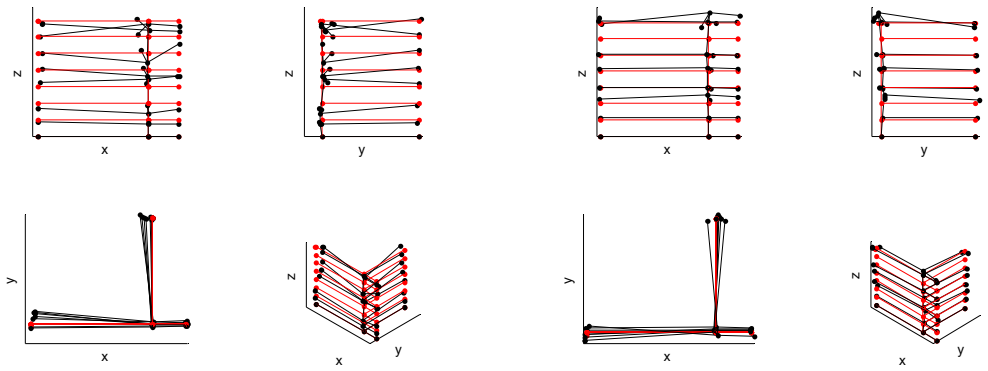

(a) (b)

Figure 7.3-15. Assembled global mode shape of Mode 6 (a) asynchronous data (b) synchronous data

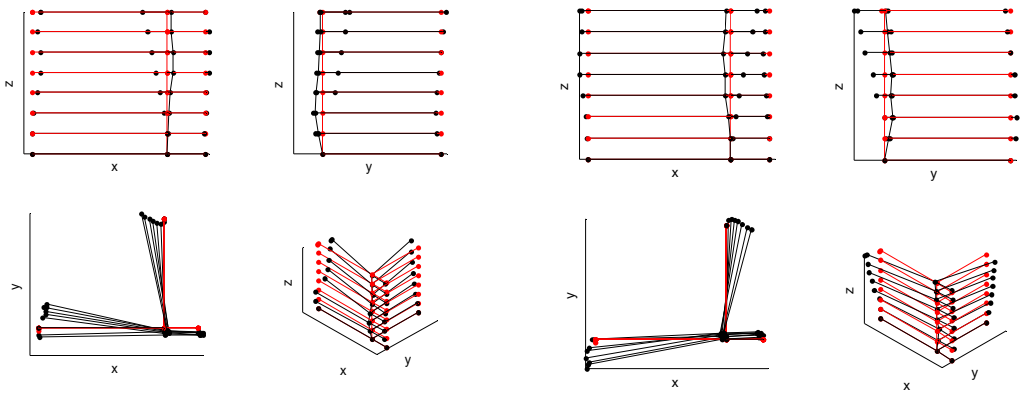

(a) (b)

Figure 7.3-16. Assembled global mode shape of Mode 6 (excluding z-direction) (a) asynchronous data (b) synchronous data

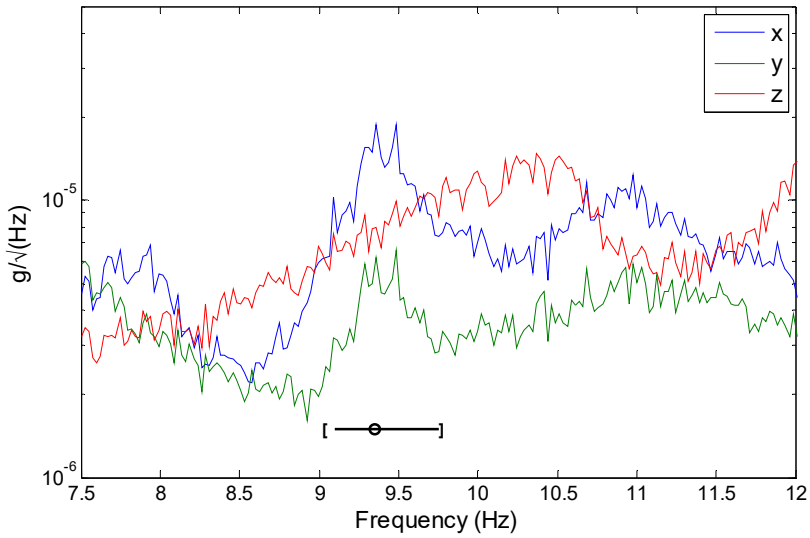

Figure 7.3-17. Root PSD spectrum of Setup 2 (6/F), asynchronous data

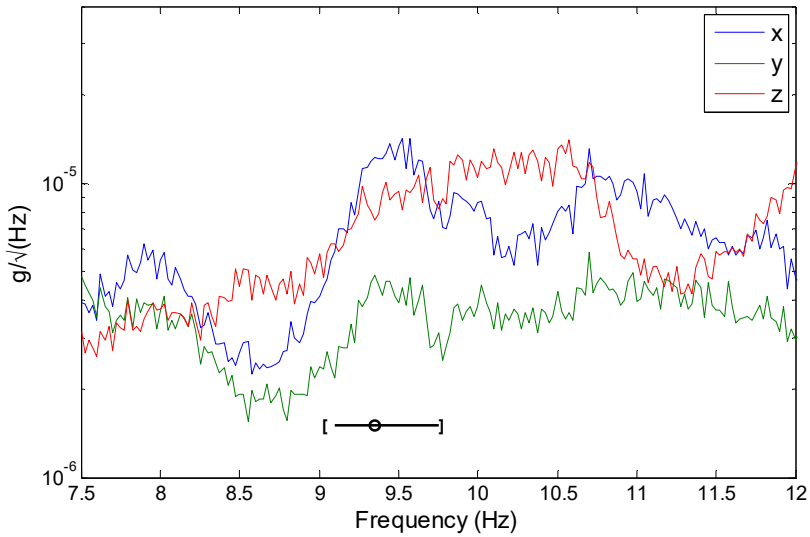

Figure 7.3-18. Root PSD spectrum of Setup 2 (6/F), synchronous data

7.3.4 Posterior uncertainty

Table 7.3-5 to *Table 7.3-7* list the posterior c.o.v.s of natural frequencies, damping ratios and mode shapes among the setups for both synchronous and asynchronous data, respectively. Compared to the posterior c.o.v.s of natural frequencies (which is

less than 1%), the posterior c.o.v.s of damping ratios are much higher, which is common in OMA. The posterior c.o.v.s of the modal parameters based on asynchronous data are of the same order compared to those based on synchronous data. The identification uncertainty of the mode shapes based on asynchronous data is larger than the synchronous counterparts. This is reasonable as the mode shapes for asynchronous data are partially identified within each synchronous group hence intuitively less data are involved for inference.

The posterior c.o.v. here reflects the unresolved uncertainty of a modal parameter given measured data and model assumptions in a particular setup. It does not imply how close the identified results are to the 'true' values due to the modelling error. Although there is no existing method that can tell what the exact uncertainty should be when identifying modal parameters. It is possible to gain more insights on the asymptotic behaviour of the identification uncertainty (i.e., the leading order behaviour of the posterior uncertainty assuming long measurement duration, high SNR and small damping) against the test configurations, which is often referred as 'uncertainty law'. *Figure 7.3-19* plots the uncertainty behaviour of the damping ratios among the setups against the modal SNR based on synchronous data for the six modes identified in this test. The curves in the figure represent ratios of the first order term in the uncertainty law (i.e., the achievable identification uncertainty based on the given SNR) to the zeroth order (i.e., the achievable identification precision for infinite SNR). The circles denote the identification uncertainty based on the current test configurations and the values in the legend denote the actual posterior c.o.v. values determined based on the measured data. It can be seen that for the first three modes, the current posterior uncertainties all lies in the flat region of the curves. Further increasing the SNR do not have significant help in reducing the identification

uncertainty of damping ratios. This is not the case for the last three modes, especially for Mode 5 and 6. For example, further increase the SNR for Mode 5 in Setup 2 can reduce the identification uncertainty up to 10%.

Table 7.3-5 Posterior c.o.v.s of natural frequencies among setups

Mode		Floor No.							Mean
		1/F	2/F	3/F	4/F	5/F	6/F	7/F	
1	Asyn.	0.06	0.09	0.06	0.04	0.06	0.06	0.06	0.06
	Syn.	0.11	0.11	0.10	0.09	0.12	0.13	0.10	0.11
2	Asyn.	0.08	0.07	0.07	0.05	0.05	0.05	0.05	0.06
	Syn.	0.11	0.20	0.11	0.14	0.14	0.10	0.08	0.13
3	Asyn.	0.04	0.03	0.03	0.03	0.03	0.03	0.04	0.03
	Syn.	0.06	0.06	0.07	0.06	0.07	0.06	0.07	0.07
4	Asyn.	0.08	0.07	0.07	0.16	0.13	0.10	0.07	0.10
	Syn.	0.22	0.16	0.14	0.16	0.17	0.19	0.15	0.17
5	Asyn.	0.10	0.10	0.07	0.07	0.24	0.31	0.13	0.15
	Syn.	0.16	0.13	0.12	0.16	0.12	0.21	0.14	0.15
6	Asyn.	0.16	0.31	0.18	0.07	0.08	0.07	0.06	0.13
	Syn.	0.15	0.43	0.07	0.13	0.09	0.29	0.10	0.18

Table 7.3-6 Posterior c.o.v.s of damping ratios among setups

Mode		Floor No.							Mean
		1/F	2/F	3/F	4/F	5/F	6/F	7/F	
1	Asyn.	8	8	7	7	7	7	7	7
	Syn.	15	14	15	14	15	15	15	15
2	Asyn.	8	9	8	7	8	8	7	8
	Syn.	16	17	16	16	17	16	15	16
3	Asyn.	5	5	5	4	4	4	4	5
	Syn.	10	10	10	10	10	10	10	10
4	Asyn.	7	6	6	10	2	8	6	6

	Syn.	16	13	12	12	13	14	12	13
5	Asyn.	4	5	4	4	8	10	5	6
	Syn.	9	8	8	9	8	10	8	9
6	Asyn.	8	9	9	5	6	5	4	6
	Syn.	10	15	7	9	8	10	8	10

Table 7.3-7 Posterior c.o.v.s of mode shapes among setups

Mode		Floor No.							Mean
		1/F	2/F	3/F	4/F	5/F	6/F	7/F	
1	Asyn.	1.66	2.72	3.36	3.65	3.89	3.85	3.85	3.28
	Syn.	0.87	0.88	0.94	0.83	0.88	0.89	0.84	0.88
2	Asyn.	1.68	2.59	3.32	3.78	3.91	3.99	4.04	3.33
	Syn.	0.66	1.01	0.69	0.86	0.86	0.95	0.83	0.84
3	Asyn.	0.92	1.72	2.04	2.40	2.50	2.53	2.52	2.09
	Syn.	0.59	0.73	0.34	0.38	0.45	0.41	0.37	0.47
4	Asyn.	3.04	3.09	2.84	3.04	18.50	3.65	2.92	5.30
	Syn.	2.51	2.70	2.32	2.16	2.38	2.58	2.50	2.45
5	Asyn.	2.04	2.51	2.30	2.04	3.94	2.58	2.46	2.55
	Syn.	1.32	1.38	1.30	1.59	2.27	3.02	1.81	1.81
6	Asyn.	2.51	2.49	3.28	2.93	2.99	2.52	2.39	2.73
	Syn.	2.41	2.48	2.92	2.78	3.00	3.47	2.79	2.83

It should be noted that the posterior c.o.v. discussed in this section is different from the sample c.o.v. in Section 7.3.2. The sample c.o.v. only reflects the statistical variability of the MPVs among the setups, which is mainly due to environmental variation.

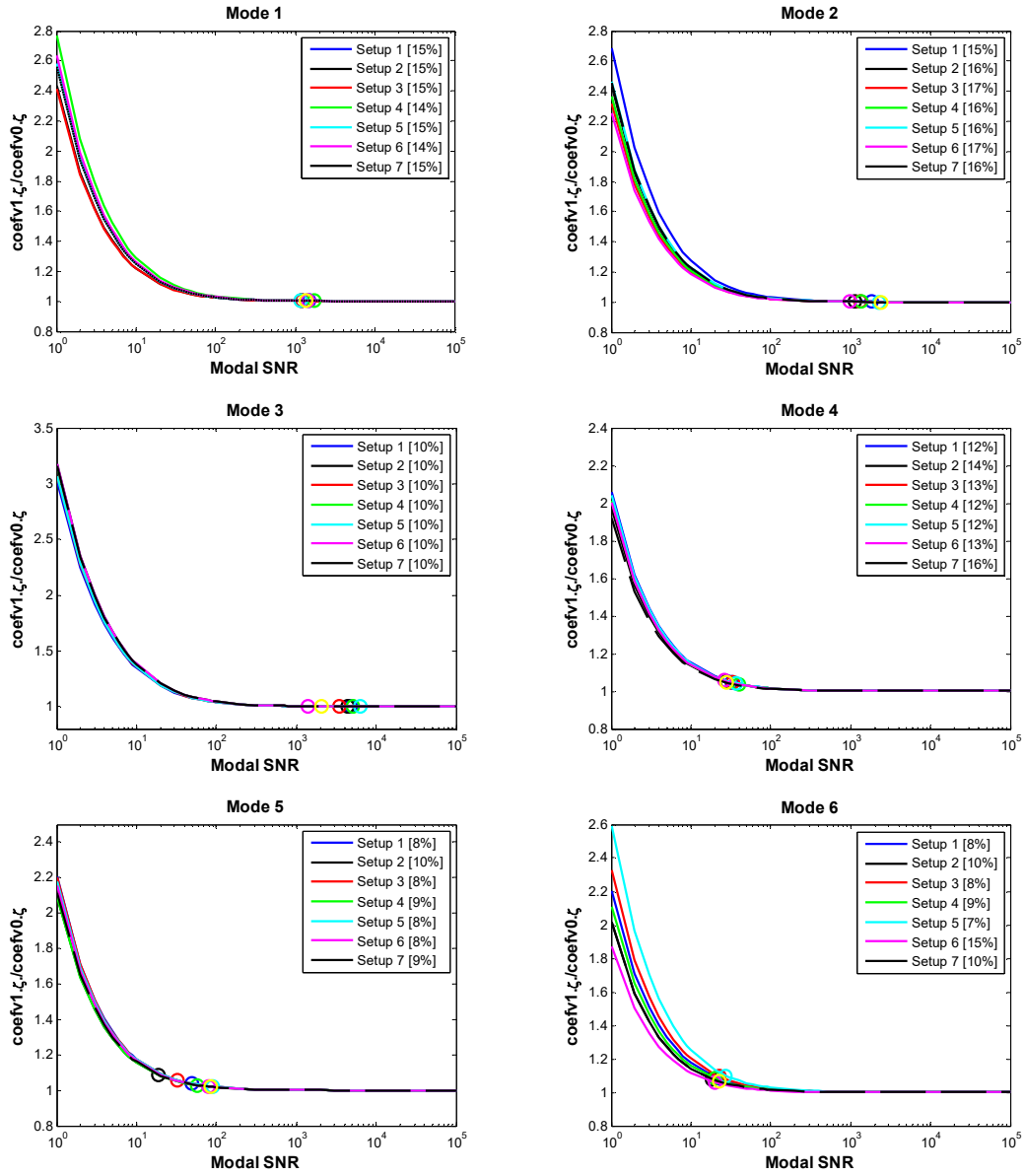

Figure 7.3-19. Uncertainty law of damping ratio based on synchronous data

7.3.5 Computational time

Some comments regarding the computational time for modal analysis are drawn in this section. The foregoing analysis is conducted using MATLAB R2014a on an HP Compaq 800 G1 Elite Desktop (Intel Core i5, 2GHz and 8GB of RAM). To obtain the MPV of modal parameters, the NLLF is optimised using MATLAB function `fminsearch` with a convergence tolerance of 10^{-6} on a fractional basis for all parameters.

Table 7.3-8 lists the computational time (total time among the setups) of MPV and posterior uncertainty of the identified modes for both synchronous and asynchronous data cases. It takes more time to determine the MPV based on asynchronous data compared to those based on synchronous data. This is especially so for the last three modes where the SNR is low. On the other hand, the computational time for determining the posterior uncertainties based on asynchronous data is slightly less than the one based on synchronous data. The whole modal analysis procedure can be done in a few minutes based on asynchronous data.

Table 7.3-8 Computational time

Mode		Time required (s)	
		MPV	Posterior c.o.v.
1	Asyn.	27	3
	Syn.	8	7
2	Asyn.	32	2
	Syn.	10	7
3	Asyn.	31	5
	Syn.	11	10
4	Asyn.	300	9
	Syn.	59	14
5	Asyn.	394	13
	Syn.	36	17
6	Asyn.	479	15
	Syn.	54	19

7.4 Discussion

In this chapter, a full-scale ambient test of an eight-storey office building has been presented to investigate the modal identification quality using asynchronous data incorporating multiple setups. The identification results based on asynchronous data

have been compared with the ones identified based on synchronous data with the same test configurations (i.e., sensor used, measurement location and duration). The identification uncertainty for both synchronous and asynchronous data has also been investigated.

The foregoing analysis shows that the identified natural frequencies and damping ratios based on asynchronous data generally agree well with the ones based on synchronous data. The assembled global mode shapes based on asynchronous data are practically consistent with those based on synchronous data when the modal SNR is high. Challenging issues exist when the modes are suspected of low SNR and high modelling error. The erroneously determined mode shape values in individual setups will lead to further discrepancies when assembling the overall mode shapes. In this context, neither one can provide a plausible estimation of the global mode shapes. The posterior uncertainties of the modal parameters identified based on asynchronous data are of similar order compared with those based on synchronous data (although they cannot be directly compared as they are obtained based on different model assumptions). The posterior uncertainties of the identified mode shapes based on asynchronous data are larger than the synchronous counterpart as less information is involved for inference. The uncertainty law based on synchronous data has also been investigated. It can be seen that for the first three modes, the posterior uncertainties of the damping ratios are already in the convergence region. However, for the last three modes, further reducing the identification uncertainty is still possible by increasing the SNRs. Modal analysis based on asynchronous data takes more time than that of synchronous data. However, the whole computational process can be done in a few minutes, which is still feasible even for on-site implementation.

The global mode shapes are assembled using the global least square method. The identified mode shapes in individual setups are equally weighted regardless of identification quality. Bayesian methods for asynchronous data that can determine the MPV of global mode shape is demanded, where the data quality in different setups can be taken into consideration for inference and better estimation results are expected. In this test, only the zero coherence method is applied for modal analysis. The general coherence method also needs to be applied in order to investigate its applicability and identification quality for full-scale ambient tests and this is one of the future works. Compared to the zero coherence method, more computational time is expected for the general coherence method.

Chapter 8: Conclusions

8.1 Concluding remarks

This thesis has presented two Bayesian approaches for modal identification using ambient vibration data measured in an asynchronous manner. The asynchronisation issue in OMA has been first investigated and a probabilistic model with imperfect coherence for asynchronous data has been proposed. Based on this model, two Bayesian modal identification methods have been proposed, which allows the most probable values as well as the posterior uncertainty of modal parameters to be determined based on asynchronous ambient data. The proposed asynchronous data model and Bayesian OMA approaches have been validated using synthetic, laboratory and full-scale ambient data with different levels of complexity. In addition, the proposed Bayesian OMA method with zero coherence has been applied to modal identification of an eight-storey office building based on asynchronous ambient data incorporating multiple setups, where detailed sensor deployment, synchronisation scheme and challenges encountered in field tests have been discussed.

Laboratory experiments have been conducted to investigate the asynchronous data in OMA. The sampling interval of a DAQ system has been investigated in the first experiment, which illustrated the asynchronisation issue in the sampling procedure due to clock jitter. It is shown that the actual sampling interval of a DAQ unit varies randomly and does not follow any specific distribution. The second experiment illustrated the effect of asynchronisation on the identification results in OMA. A Bayesian method that assumes synchronous data was applied to modal identification of a set of asynchronous ambient data measured on a four-storey laboratory shear building model. The identified natural frequencies and damping ratios are not

severely affected by the time synchronisation issue in the measured data. However, the relative scaling and directions of the mode shapes are erroneously determined. In the third example, the relationship between the asynchronisation and the measurement duration has been explored. It is found that the coherence between two asynchronous data channels decreases with the increase of the measurement time, illustrating a decrease of synchronisation degree between the channels.

Inspired by the experimental findings, a probabilistic model for asynchronous data in OMA has been proposed. Asynchronous data are fundamentally a non-stationary process, which is difficult to model or analyse. Balancing model simplicity and utility, a stationary stochastic model was proposed with imperfect coherence parameter that captures key asynchronous characteristics within suitable time scales. The characteristics of the PSD matrix based on the proposed asynchronous data model have also been investigated.

Based on the asynchronous data model, two Bayesian modal identification methods for asynchronous ambient data have been proposed. The first method was developed based on a simplified model that assumes zero coherence among the synchronous data groups, which provides a fast algorithm to determine the MPV of modal parameters. The analytical expression of the posterior covariance matrix has also been derived, which provides the associated identification uncertainty of the modal parameters. The second method assumes general coherence among synchronous groups, which strictly obeys the asynchronous data model. Efficient computational strategies have been proposed, which significantly suppresses the dimension of matrix computation involved and preserve the constraints during the optimisation procedure. The resulting iterative procedure allows the MPV of modal parameters as

well as the coherence to be determined efficiently. Although more computational effort is expected compared to the first method, this method is more robust with less modelling error involved.

Synthetic, laboratory and field test data have been used to verify the proposed asynchronous data model and the proposed Bayesian modal identification methods. It is found that the properties of the PSD matrix based on proposed asynchronous data model fit well with the ones estimated based on the synthetic and measured laboratory data. The effect of modelling error due to zero coherence assumption has been investigated through a parametric study. It is found that such modelling error does not cause bias in the MPV of modal parameters, but leads to under-estimation in the posterior uncertainty. Nevertheless, such effect is not significant unless the actual coherence among the synchronous data groups in the measured data is high. Besides the synthetic data, the proposed Bayesian methods have also been validated using real asynchronous data measured from a four-storey laboratory shear building model and a full-scale office building. The identified modal parameters based on asynchronous data from these two methods agree well with the ones based on synchronous data, verifying their consistency. The posterior uncertainties of the identified mode shapes based on asynchronous data are larger than the synchronous counterpart as less information is involved for inference.

To further investigate the applicability of the proposed methods in field tests, a full-scale ambient vibration test on an eight-storey building incorporating multiple setups was presented. Detailed sensor specification, instrumentation techniques and synchronisation procedure involved in the test have been discussed, which illustrates the practical issues encountered in full-scale ambient test based on asynchronous data

and provides a guidance for further field tests. Both synchronous and asynchronous ambient vibration data sets have been measured. Modal identification based on these two data sets has been conducted and the global mode shapes of the building have been assembled. The identification results based on asynchronous data agree well with the ones based on synchronous data when the modal SNR is high. Identification difficulties occur when the modal SNR of the mode is low. In this context, neither one can provide a reasonable estimation of the global mode shapes. The identification uncertainties based on asynchronous data are of the same order compared to those based on synchronous data. They are also compared with the uncertainty law for the synchronous data set. Modal identification based on asynchronous data generally takes more time compared to synchronous data. Nevertheless, the whole procedure can be done in a few minutes, which is still quite efficient.

8.2 Future work

According to the current development of the Bayesian modal identification methods for asynchronous ambient data proposed in this work, several research directions can be pursued:

1) The Bayesian modal identification methods proposed in this thesis only considered the case when single mode is dominant in the selected frequency band. However, close-spaced modes are often encountered in real applications, especially for long-span bridges and tall buildings. Modelling close-spaced mode with asynchronisation issue in the measured data can be challenging but the resulting modal identification methods will be useful in practice.

2) In this work, the proposed modal identification methods can only handle the measured asynchronous ambient in a single setup. For multiple setups, the global mode shapes need to be assembled using conventional techniques where the identification quality of individual setups is not taken into consideration for assembling. Further development of Bayesian methods for asynchronous ambient data incorporating multiple setups are demanded, where the global mode shapes can be inferred with probability logic without heuristics.
3) Currently, only the identification uncertainty based on the proposed Bayesian method with zero coherence assumption is investigated. The analytical expression for the posterior covariance matrix based on the proposed Bayesian method with general coherence assumption needs to be derived, which is expected to provide a better estimation of identification uncertainty for asynchronous ambient data.
4) More field tests based on asynchronous ambient vibration data shall be conducted to further explore the challenges encountered in full-scale tests using asynchronous data and investigate the applicability of the proposed methods in this work. Without the time synchronisation requirements, more efficient and flexible ways of conducting ambient vibration tests can be explored. For example, smartphones nowadays have built-in accelerometers. Based on the proposed methods, multiple smartphones can be used to conduct ambient vibration tests without synchronisation. Smartphone software needs to be developed that can conduct modal identification directly on the phone using the proposed methods.

References

[1] Infrastructure Cost Review: Main Report, 2010. http://www.hm-treasury.gov.uk/d/cost_review_main211210.pdf.

[2] J.M.W. Brownjohn, Structural health monitoring of civil infrastructure., Philos. Trans. A. Math. Phys. Eng. Sci. 365 (2007) 589–622. doi:10.1098/rsta.2006.1925.

[3] C.R. Farrar, K. Worden, An introduction to structural health monitoring., Philos. Trans. A. Math. Phys. Eng. Sci. 365 (2007) 303–315. doi:10.1098/rsta.2006.1928.

[4] D.E. Hudson, Dynamic Tests of Full-Scale Structures, J. Eng. Mech. Div. 103 (1977) 1141–1157.

[5] D.J. Ewins, Modal testing : theory, practice, and application, Baldock : Research Studies Press, 2000., 2000.

[6] R. Brincker, C.E. Ventura, Introduction to Operational Modal Analysis, Wiley, London, 2015. doi:10.1002/9781118535141.

[7] S.-K. Au, Operational Modal Analysis: Modeling, Bayesian Inference, Uncertainty Laws, Springer, 2017.

[8] M. Di Paolo Emilio, Data Acquisition Systems, Springer New York, New York, NY, 2013. doi:10.1007/978-1-4614-4214-1.

[9] R.W. Clough, J. Penzien, Dynamics of structures, Computers & Structures, Inc, 2003.

[10] P. Dallard, A. Flint, S. Le Bourva, A. Low, R.M.R. Smith, M. Willford, The

London Millenium Footbridge, Struct. Eng. 79 (2001) 17–35. doi:10.2749/101686699780481709.

[11] H. Marukawa, N. Kato, K. Fujii, Y. Tamura, Experimental evaluation of aerodynamic damping of tall buildings, J. Wind Eng. Ind. Aerodyn. 59 (1996) 177–190. doi:10.1016/0167-6105(96)00006-2.

[12] Y. Tamura, S. Suganuma, Evaluation of amplitude-dependent damping and natural frequency of buildings during strong winds, J. Wind Eng. Ind. Aerodyn. 59 (1996) 115–130. doi:10.1016/0167-6105(96)00003-7.

[13] Y. Fujino, Vibration, control and monitoring of long-span bridges - Recent research, developments and practice in Japan, J. Constr. Steel Res. 58 (2002) 71–97. doi:10.1016/S0143-974X(01)00049-9.

[14] N. Hoang, Y. Fujino, P. Warnitchai, Optimal tuned mass damper for seismic applications and practical design formulas, Eng. Struct. 30 (2008) 707–715. doi:10.1016/j.engstruct.2007.05.007.

[15] R. Rana, T.T. Soong, Parametric study and simplified design of tuned mass dampers, Eng. Struct. 20 (1998) 193–204. doi:http://dx.doi.org/10.1016/S0141-0296(97)00078-3.

[16] N.M.M. Maia, J.M.M. Silva, E.A.M. Almas, R.P.C. Sampaio, E.N. ! A Autica, I.D. Henrique, Damage Detection in Structures: From Mode Shape To Frequency Response Function Methods, Mech. Syst. Signal Process. 17 (2003) 489–498. doi:10.1006/mssp.2002.1506.

[17] Y. Xia, H. Hao, J.M.W. Brownjohn, P.Q. Xia, Damage identification of structures with uncertain frequency and mode shape data, Earthq. Eng. Struct.

Dyn. 31 (2002) 1053–1066. doi:10.1002/eqe.137.

[18] E.J. Cross, K.Y. Koo, J.M.W. Brownjohn, K. Worden, Long-term monitoring and data analysis of the Tamar Bridge, Mech. Syst. Signal Process. 35 (2012) 16–34. doi:10.1016/j.ymssp.2012.08.026.

[19] S. Au, P. To, Full-scale validation of dynamic wind load on a super-tall building under strong wind, J. Struct. Eng. (2012) 1161–1172. doi:10.1061/(ASCE)ST.1943-541X.0000539.

[20] Q.S. Li, Y.Q. Xiao, C.K. Wong, A.P. Jeary, Field measurements of typhoon effects on a super tall building, Eng. Struct. 26 (2004) 233–244. doi:10.1016/j.engstruct.2003.09.013.

[21] S. Lagomarsino, Forecast models for damping and vibration periods of buildings, J. Wind Eng. Ind. Aerodyn. 48 (1993) 221–239. doi:10.1016/0167-6105(93)90138-E.

[22] a. Kareem, K. Gurley, Damping in structures: its evaluation and treatment of uncertainty, J. Wind Eng. Ind. Aerodyn. 59 (1996) 131–157. doi:10.1016/0167-6105(96)00004-9.

[23] P.C. Chang, A. Flatau, S.C. Liu, Review Paper: Health Monitoring of Civil Infrastructure, Struct. Heal. Monit. 2 (2003) 257–267. doi:10.1177/1475921703036169.

[24] J.L. Beck, L.S. Katafygiotis, Updating Models and Their Uncertainties. I: Bayesian Statistical Framework, J. Eng. Mech. 124 (1998) 455–461. doi:10.1061/(ASCE)0733-9399(1998)124:4(455).

[25] C. Papadimitriou, J.L. Beck, L.S. Katafygiotis, Updating robust reliability using structural test data, Probabilistic Eng. Mech. 16 (2001) 103–113. doi:10.1016/S0266-8920(00)00012-6.

[26] G. Hearn, R. Testa, Modal analysis for damage detection in structures, J. Struct. Eng. 117 (1991) 3042–3063.

[27] A. Rahai, F. Bakhtiari-Nejad, A. Esfandiari, Damage Assessment of Structure using Incomplete Measured Mode Shapes, Struct. Control Heal. Monit. 14 (2006) 808–829. doi:10.1002/stc.183.

[28] S.K. Au, C.T. Ng, H.W. Sien, H.Y. Chua, Modal identification of a suspension footbridge using free vibration signatures, Int. J. Appl. Math. Mech. 1 (2006) 55–73.

[29] M. Ülker-Kaustell, R. Karoumi, Application of the continuous wavelet transform on the free vibrations of a steel-concrete composite railway bridge, Eng. Struct. 33 (2011) 911–919. doi:10.1016/j.engstruct.2010.12.012.

[30] T.-P. Le, P. Argoul, Continuous wavelet transform for modal identification using free decay response, J. Sound Vib. 277 (2004) 73–100. doi:10.1016/j.jsv.2003.08.049.

[31] S.R. Ibrahim, E.C. Mikulcik, A method for the direct identification of vibration parameters from the free response, Shock Vib. Bull. 4 (1977) 183–198.

[32] D.L. Brown, R.J. Allemang, R. Zimmerman, M. Mergeay, Parameter Estimation Techniques for Modal Analysis, in: SAE Tech. Pap., 1979. doi:10.4271/790221.

[33] M. Ruzzene, A. Fasana, L. Garibaldi, B. Piombo, Natural frequencies and dampings identification using wavelet transform: Application to real data, Mech. Syst. Signal Process. 11 (1997) 207–218. doi:10.1006/mssp.1996.0078.

[34] F.-L. Zhang, Y.-C. Ni, S.-K. Au, H.-F. Lam, Fast Bayesian approach for modal identification using free vibration data, Part I – Most probable value, Mech. Syst. Signal Process. 70–71 (2015). doi:http://dx.doi.org/10.1016/j.ymssp.2015.05.031.

[35] Y.-C. Ni, F.-L. Zhang, H.-F. Lam, S.-K. Au, Fast Bayesian approach for modal identification using free vibration data, Part II—Posterior uncertainty and application, Mech. Syst. Signal Process. 70–71 (2016) 221–244. doi:10.1016/j.ymssp.2015.06.009.

[36] A. De Sortis, E. Antonacci, F. Vestroni, Dynamic identification of a masonry building using forced vibration tests, Eng. Struct. 27 (2005) 155–165. doi:10.1016/j.engstruct.2004.08.012.

[37] J.M.W. Brownjohn, A. Pavic, Experimental methods for estimating modal mass in footbridges using human-induced dynamic excitation, Eng. Struct. 29 (2007) 2833–2843. doi:10.1016/j.engstruct.2007.01.025.

[38] J.M.W. Brownjohn, M. Bocian, D. Hester, A. Quattrone, W. Hudson, D. Moore, S. Goh, M.S. Lim, Footbridge system identification using wireless inertial measurement units for force and response measurements, J. Sound Vib. 384 (2016) 339–355. doi:10.1016/j.jsv.2016.08.008.

[39] Z. Zembaty, M. Kowalski, Dynamic identification of a model of brick masonry building, Arch. Civ. Eng. 46 (2000) 106–136.

https://www.scopus.com/inward/record.uri?eid=2-s2.0-0038831392&partnerID=40&md5=7aac7e3d384ed40b9f949b69158a2b27.

[40] C.-Y. Liou, C.-C. Shen, Damping ratio estimation using hybrid methods, Mech. Syst. Signal Process. 4 (1990). doi:10.1016/0888-3270(90)90008-9.

[41] N.M.M. Maia, J.M.M. e Silva, Theoretical and experimental modal analysis, Research Studies Press, 1997.

[42] J. Kirshenboim, D.J. Ewins, Method for the Derivation of Optimal Modal Parameters From Several Single-Point Excitation Tests., Proc. Int. Modal Anal. Conf. Exhib. 2 (1984) 991–997. http://www.scopus.com/inward/record.url?eid=2-s2.0-0021586631&partnerID=40&md5=3060fca8abbab33e64e869919ccb98d2.

[43] D.J. Ewins, P.T. Gleeson, A method for modal identification of lightly damped structures, J. Sound Vib. 84 (1982) 57–79. doi:10.1016/0022-460X(82)90432-1.

[44] H. Van der Auweraer, J. Leuridan, Multiple input orthogonal polynomial parameter estimation, Mech. Syst. Signal Process. 1 (1987) 259–272. doi:10.1016/0888-3270(87)90103-8.

[45] S.K. Au, Y.C. Ni, Fast Bayesian modal identification of structures using known single-input forced vibration data, Struct. Control Heal. Monit. 21 (2014) 381–402. doi:10.1002/stc.1571.

[46] Y.C. Ni, F.L. Zhang, Fast Bayesian approach for modal identification using forced vibration data considering the ambient effect, Mech. Syst. Signal Process. 105 (2018) 113–128. doi:10.1016/j.ymssp.2017.11.007.

[47] S.S. Ivanović, M.D. Trifunac, E.I. Novikova, a. a. Gladkov, M.I. Todorovska, Ambient vibration tests of a seven-story reinforced concrete building in Van Nuys, California, damaged by the 1994 northridge earthquake, Soil Dyn. Earthq. Eng. 19 (2000) 391–411. doi:10.1016/S0267-7261(00)00025-7.

[48] H. Wenzel, D. Pichler, Ambient vibration monitoring, Wiley, UK, 2005.

[49] J.M.W. Brownjohn, F. Magalhaes, E. Caetano, A. Cunha, Ambient vibration re-testing and operational modal analysis of the Humber Bridge, Eng. Struct. 32 (2010) 2003–2018. doi:10.1016/j.engstruct.2010.02.034.

[50] J. Bendat, A. Piersol, Engineering applications of correlation and spectral analysis, 1993. doi:10.1016/0022-460X(81)90424-7.

[51] J.S. Bendat, A.G. Piersol, Engineering applications of correlation and spectral analysis., New York: Wiley, 1980., 1980.

[52] R. Brincker, L. Zhang, P. Andersen, Modal identification of output-only systems using frequency domain decomposition, Smart Mater. Struct. 10 (2001) 441–445. doi:10.1088/0964-1726/10/3/303.

[53] J. Rodrigues, R. Brincker, P. Andersen, Improvement of frequency domain output-only modal identification from the application of the random decrement technique, Proc. 23rd Int. Modal Anal. …. (2004).

[54] L. Zhang, T. Wang, A Frequency-Spatial Domain Decomposition (FSDD) Technique for Operational Modal Analysis, Mech. Syst. Signal Process. 24 (2010) 1227–1239.

[55] P. Verboven, Frequency-domain system identification for modal analysis,

2002.

[56] B. Peeters, H. Van Der Auweraer, P. Guillaume, J. Leuridan, The PolyMAX frequency-domain method : a new standard for modal parameter estimation?, Shock Vib. 11 (2004) 395–409. doi:10.1155/2004/523692.

[57] P. Andersen, Identification of Civil Engineering Structures using Vector ARMA Models, 1997.

[58] I. James, George H., T.G. Carne, J.P. Lauffer, The natural excitation technique (NExT) for modal parameter extraction from operating structures, Int. J. Anal. Exp. Modal Anal. 10 (1995) 260–277.

[59] A. Benveniste, J.J. Fuchs, Single Sample Modal Identification of a Nonstationary Stochastic Process, IEEE Trans. Automat. Contr. 30 (1985) 66–74. doi:10.1109/TAC.1985.1103787.

[60] M. Aoki, State space modeling of time series, Springer, Berlin, German, 2013.

[61] P. Van Overschee, B. De Moor, Subspace algorithms for the stochastic identification problem, Automatica. 29 (1993) 649–660. doi:10.1016/0005-1098(93)90061-W.

[62] P. Van Overschee, B.L. De Moor, Subspace identification for linear systems: Theory—Implementation—Applications, Springer Science & Business Media, 2012.

[63] L.F. Ramos, L. Marques, P.B. Lourenço, G. De Roeck, A. Campos-Costa, J. Roque, Monitoring historical masonry structures with operational modal analysis: Two case studies, Mech. Syst. Signal Process. 24 (2010) 1291–1305.

doi:10.1016/j.ymssp.2010.01.011.

[64] J.-H. Weng, C.-H. Loh, J.P. Lynch, K.-C. Lu, P.-Y. Lin, Y. Wang, Output-only modal identification of a cable-stayed bridge using wireless monitoring systems, Eng. Struct. 30 (2008) 1820–1830. doi:10.1016/j.engstruct.2007.12.002.

[65] J. Antoni, Blind separation of vibration components: Principles and demonstrations, Mech. Syst. Signal Process. 19 (2005) 1166–1180. doi:10.1016/j.ymssp.2005.08.008.

[66] F. Poncelet, G. Kerschen, J.C. Golinval, D. Verhelst, Output-only modal analysis using blind source separation techniques, Mech. Syst. Signal Process. 21 (2007) 2335–2358. doi:10.1016/j.ymssp.2006.12.005.

[67] A. Sadhu, S. Narasimhan, A decentralized blind source separation algorithm for ambient modal identification in the presence of narrowband disturbances, Struct. Control Heal. Monit. 21 (2014) 282–302.

[68] P. Guillaume, P. Verboven, S. Vanlanduit, Frequency-domain maximum likelihood identification of modal parameters with confidence intervals, in: Proc. Int. Semin. Modal Anal., 1998: pp. 359–366.

[69] E. Parloo, P. Guillaume, B. Cauberghe, Maximum likelihood identification of non-stationary operational data, J. Sound Vib. 268 (2003) 971–991. doi:10.1016/S0022-460X(03)00377-8.

[70] C. Devriendt, P. Guillaume, The use of transmissibility measurements in output-only modal analysis, Mech. Syst. Signal Process. 21 (2007) 2689–2696. doi:10.1016/j.ymssp.2007.02.008.

[71] W.-J. Yan, W.-X. Ren, An Enhanced Power Spectral Density Transmissibility (EPSDT) approach for operational modal analysis: Theoretical and experimental investigation, Eng. Struct. 102 (2015) 108–119. doi:10.1016/j.engstruct.2015.08.009.

[72] K.V. Yuen, L.S. Katafygiotis, Bayesian time-domain approach for modal updating using ambient data, Probabilistic Eng. Mech. 16 (2001).

[73] L.S. Katafygiotis, K.V. Yuen, Bayesian spectral density approach for modal updating using ambient data, Earthq. Eng. Struct. Dyn. 30 (2001) 1103–1123. doi:10.1002/eqe.53.

[74] W.-J. Yan, L.S. Katafygiotis, A two-stage fast Bayesian spectral density approach for ambient modal analysis. Part I: Posterior most probable value and uncertainty, Mech. Syst. Signal Process. 54 (2015) 139–155. doi:10.1016/j.ymssp.2014.07.027.

[75] W.-J. Yan, L.S. Katafygiotis, A two-stage fast Bayesian spectral density approach for ambient modal analysis. Part II: Mode shape assembly and case studies, Mech. Syst. Signal Process. 54 (2015) 156–171. doi:10.1016/j.ymssp.2014.08.016.

[76] K.V. Yuen, L.S. Katafygiotis, Bayesian fast Fourier transform approach for modal updating using ambient data, Adv. Struct. Eng. 6 (2003) 81–95.

[77] S.-K. Au, F.-L. Zhang, Y.-C. Ni, Bayesian operational modal analysis: Theory, computation, practice, Comput. Struct. 126 (2013) 3–14. doi:10.1016/j.compstruc.2012.12.015.

[78] S.-K. Au, Fast Bayesian FFT method for ambient modal identification with

separated modes, J. Eng. Mech. (2011). doi:10.1061/(ASCE)EM.1943-7889.0000213.

[79] S.-K. Au, Fast Bayesian ambient modal identification in the frequency domain, Part I : Posterior most probable value, Mech. Syst. Signal Process. 26 (2012) 60–75. doi:10.1016/j.ymssp.2011.06.017.

[80] S.-K. Au, Fast Bayesian ambient modal identification in the frequency domain, Part II: Posterior uncertainty, Mech. Syst. Signal Process. 26 (2012) 76–90. doi:10.1016/j.ymssp.2011.06.019.

[81] S.-K. Au, F.-L. Zhang, Fast Bayesian ambient modal identification incorporating multiple setups, J. Eng. Mech. (2012) 800–815. doi:10.1061/(ASCE)EM.1943-7889.0000385.

[82] E.P. Carden, A. Mita, Challenges in developing confidence intervals on modal parameters estimated for large civil infrastructure with stochastic subspace identification, Struct. Control Heal. Monit. 18 (2009) 53–79. doi:10.1002/stc.358.

[83] R. Pintelon, P. Guillaume, J. Schoukens, Uncertainty calculation in (operational) modal analysis, Mech. Syst. Signal Process. 21 (2007) 2359–2373. doi:10.1016/j.ymssp.2006.11.007.

[84] E. Reynders, R. Pintelon, G. De Roeck, Uncertainty bounds on modal parameters obtained from stochastic subspace identification, Mech. Syst. Signal Process. 22 (2008) 948–969. doi:10.1016/j.ymssp.2007.10.009.

[85] M. Döhler, X.B. Lam, L. Mevel, Uncertainty quantification for modal parameters from stochastic subspace identification on multi-setup

measurements, Mech. Syst. Signal Process. 36 (2013) 562–581. doi:10.1016/j.ymssp.2012.11.011.

[86] T.J. Matarazzo, S.N. Pakzad, Sensitivity Metrics for Maximum Likelihood System Identification, ASCE-ASME J. Risk Uncertain. Eng. Syst. Part A Civ. Eng. (2015). doi:10.1061/AJRUA6.0000832.

[87] W.J. Yan, W.X. Ren, Circularly-symmetric complex normal ratio distribution for scalar transmissibility functions. Part II: Probabilistic model and validation, Mech. Syst. Signal Process. 80 (2016) 78–98. doi:10.1016/j.ymssp.2016.02.068.

[88] W.-J. Yan, W.-X. Ren, Circularly-symmetric complex normal ratio distribution for scalar transmissibility functions. Part I: Fundamentals, Mech. Syst. Signal Process. 80 (2016) 58–77.

[89] J.L. Beck, Bayesian system identification based on probability logic, Struct. Control Heal. Monit. 17 (2010) 825–847. doi:10.1002/stc.424.

[90] F.-L. Zhang, S.-K. Au, H.-F. Lam, Assessing uncertainty in operational modal analysis incorporating multiple setups using a Bayesian approach, Struct. Control Heal. Monit. (2014). doi:10.1002/stc.1679.

[91] S.-K. Au, Connecting Bayesian and frequentist quantification of parameter uncertainty in system identification, Mech. Syst. Signal Process. 29 (2012) 328–342. doi:10.1016/j.ymssp.2012.01.010.

[92] S.-K. Au, Uncertainty law in ambient modal identification---Part I: Theory, Mech. Syst. Signal Process. 48 (2014) 15–33. doi:10.1016/j.ymssp.2013.07.016.

[93] S.-K. Au, Uncertainty law in ambient modal identification---Part II: Implication and field verification, Mech. Syst. Signal Process. 48 (2014) 34–48. doi:10.1016/j.ymssp.2013.07.017.

[94] S.K. Au, J.M.W. Brownjohn, J.E. Mottershead, Quantifying and managing uncertainty in operational modal analysis, Mech. Syst. Signal Process. 102 (2018) 139–157. doi:10.1016/j.ymssp.2017.09.017.

[95] D.R. Brillinger, Time series: data analysis and theory, Siam, 1981.

[96] E.A. Gerber, A. Ballato, Precision frequency control, 1985.

[97] J.R. Vig, Introduction to Quartz Frequency Standards, (1992).

[98] E. Kaplan, C. Hegarty, Understanding GPS: principles and applications, Artech house, 2005.

[99] D.L. Mills, Internet time synchronization: the network time protocol, IEEE Trans. Commun. 39 (1991) 1482–1493. doi:10.1109/26.103043.

[100] J.P. Lynch, A Summary Review of Wireless Sensors and Sensor Networks for Structural Health Monitoring, Shock Vib. Dig. 38 (2006) 91–128. doi:10.1177/0583102406061499.

[101] J. Elson, L. Girod, D. Estrin, Fine-grained network time synchronization using reference broadcasts, ACM SIGOPS Oper. Syst. Rev. 36 (2002) 147–163. doi:10.1145/844128.844143.

[102] S. Ganeriwal, R. Kumar, M.B. Srivastava, Timing-Sync Protocol for Sensor Networks, in: Proc. 1st ACM Int. Conf. Embed. Networked Sens. Syst., 2003: pp. 138–149. doi:10.1145/958507.958508.

[103] Y. Lei, A.S. Kiremidjian, K.K. Nair, J.P. Lynch, K.H. Law, Algorithms for time synchronization of wireless structural monitoring sensors, Earthq. Eng. Struct. Dyn. 34 (2005) 555–573. doi:10.1002/eqe.432.

[104] V. Krishnamurthy, K. Fowler, E. Sazonov, The effect of time synchronization of wireless sensors on the modal analysis of structures, Smart Mater. Struct. 17 (2008) 055018. doi:10.1088/0964-1726/17/5/055018.

[105] J.P. Lynch, Y. Wang, K.H. Law, J.H. Yi, C.G. Lee, C.B. Yun, Validation of a large-scale wireless structural monitoring system on the Geumdang Bridge, in: Proc. 9th Int. Conf. Struct. Saf. Reliab., 2005: p. http://vibration.shef.ac.uk/doc/10176624.pdf.

[106] G. Yan, S.J. Dyke, Structural damage detection robust against time synchronization errors, Smart Mater. Struct. 19 (2010) 065001. doi:10.1088/0964-1726/19/6/065001.

[107] J.-H. Park, J.-T. Kim, W.-B. Na, J. Woo, Output-only Modal Analysis Approach for Time-Unsynchronization Signals in Wireless Sensor Network, in: Proc. SPIE - Int. Soc. Opt. Eng., 2009: p. 72952B–72952B–12. doi:10.1117/12.816264.

[108] R. Brincker, A. Brandt, Time synchronization by modal correlation, in: Int. Oper. Modal Anal. Conf. IOMAC'11, 2011. http://www.iomac.dk/.

[109] K. Dragos, K. Smarsly, An embedded algorithm for detecting and accommodating synchronization problems in wireless structural health monitoring systems, in: 24rd Int. Work. Intell. Comput. Eng., 2017.

[110] D.B. Sullivan, J. Levine, Time Generation and Distribution, Proc. IEEE. 79

(1991) 906–914. doi:10.1109/5.84966.

[111] A. Hajimiri, T.H. Lee, A general theory of phase noise in electrical oscillators, IEEE J. Solid-State Circuits. 33 (1998) 179–194. doi:10.1109/4.658619.

[112] A. Demir, Computing timing jitter from phase noise spectra for oscillators and phase-locked loops with white and 1/f noise, IEEE Trans. Circuits Syst. I Regul. Pap. 53 (2006) 1869–1884. doi:10.1109/TCSI.2006.881184.

[113] S. Bjorklund, L. Ljung, A review of time-delay estimation techniques, in: 42nd IEEE Int. Conf. Decis. Control (IEEE Cat. No.03CH37475), 2003: pp. 2502–2507. doi:10.1109/CDC.2003.1272997.

[114] G. Jacovitti, G. Scarano, Discrete time techniques for time delay estimation, IEEE Trans. Signal Process. 41 (1993) 525–533. doi:10.1109/78.193195.

[115] A. Demir, A. Mehrotra, J. Roychowdhury, Phase noise in oscillators: A unifying theory and numerical methods for characterization, Circuits Syst. I Fundam. Theory Appl. IEEE Trans. 47 (2000) 655–674. doi:10.1109/81.847872.

[116] M. Löhning, G. Fettweis, The effects of aperture jitter and clock jitter in wideband ADCs, Comput. Stand. Interfaces. 29 (2007) 11–18. doi:10.1016/j.csi.2005.12.005.

[117] S.-K. Au, F.-L. Zhang, On assessing the posterior mode shape uncertainty in ambient modal identification, Probabilistic Eng. Mech. 26 (2011) 427–434. doi:10.1016/j.probengmech.2010.11.009.

[118] W. Gander, G.H. Golub, U. von Matt, A constrained eigenvalue problem,

Linear Algebra Appl. 114–115 (1989) 815–839. doi:10.1016/0024-3795(89)90494-1.

[119] R. Sleeman, A. van Wettum, J. Trampert, Three-channel correlation analysis: A new technique to measure instrumental noise of digitizers and seismic sensors, Bull. Seismol. Soc. Am. 96 (2006) 258–271. doi:10.1785/0120050032.

[120] S.-K. Au, Assembling mode shapes by least squares, Mech. Syst. Signal Process. 25 (2011) 163–179. doi:10.1016/j.ymssp.2010.08.002.

Publications

Journal Articles:

[1] **Zhu YC**, Au SK. Spectral characteristics of asynchronous data in operational modal analysis. *Structural Control and Health Monitoring* 2017; **24**(11).

[2] **Zhu YC**, Au SK. Bayesian Operational Modal Analysis with Asynchronous Data, Part I: Most Probable Value. *Mechanical Systems and Signal Processing* 2018; **98C**: 652–666.

[3] **Zhu YC**, Au SK. Bayesian Operational Modal Analysis with Asynchronous Data, Part II: Posterior Uncertainty. *Mechanical Systems and Signal Processing* 2018; **98C**: 920–935.

[4] **Zhu YC**, Xie YL, Au SK. Operational modal analysis of an eight-storey building with asynchronous data incorporating multiple setups. *Engineering Structures* 2018; **165**: 50–62.

[5] Brownjohn JMW, Au SK, **Zhu YC**, Sun Z, Li BB, Bassitt J, *et al.* Bayesian operational modal analysis of Jiangyin Yangtze River Bridge. *Mechanical Systems and Signal Processing* 2018; **110**: 210-230.

Conference Papers:

[6] **Zhu YC**, Au SK, Jones S. Identification uncertainty of close modes in operational modal analysis. *12th International Conference on Applications of Statistics and Probability in Civil Engineering*, 2015.

[7] **Zhu YC**, Au SK, Jones S. Uncertainty of closely-spaced modes in Bayesian modal identification. *Engineering Mechanics Institute Conference*, 2015.

[8] **Zhu YC**, Au SK. Bayesian modal identification using asynchronous 'output-only' ambient data. *Engineering Mechanics Institute Conference*, 2017.

[9] Xie YL, **Zhu YC**, Au SK. Operational modal analysis of brodie tower using a

Bayesian approach. *2nd International Conference on Uncertainty Quantification in Computational Sciences and Engineering*, 2017.

Manuscript under Review:

[10] **Zhu YC**, Au SK, Brownjohn JMW. Bayesian operational modal analysis with buried modes. *Mechanical Systems and Signal Processing*

Manuscript under Preparation:

[11] **Zhu YC**, Au SK. Bayesian modal identification method based on general coherence model for asynchronous ambient data.